



**UNIVERSITY OF
PLYMOUTH**

**GRAPHENE/SILICON SCHOTTKY JUNCTION
SOLAR CELLS WITH HIGH EFFICIENCY**

by

AHMED MUNEEER SUHAIL

A thesis submitted to the University of Plymouth in partial
fulfillment for the degree of

DOCTOR OF PHILOSOPHY

School of Engineering, Computing and Mathematics

October 2018

COPYRIGHT STATEMENT

This copy of the thesis has been supplied on condition that anyone who consults it is understood to recognise that its copyright rests with its author and that no quotation from the thesis and no information derived from it may be published without the author`s prior consent.

Abstract

GRAPHENE/SILICON SCHOTTKY JUNCTION SOLAR CELLS WITH HIGH EFFICIENCY

AHMED MUNEER SUHAIL

Silicon p-n junction solar cells have a power conversion efficiency (*PCE*) up to 12%. Graphene, which has unique properties is an excellent material for solar cells with the potential to achieve higher *PCEs*. Since 2009, researchers have started to integrate CVD-graphene with Si substrates to develop Schottky junction solar cells with potentially higher *PCE*. However, there are several challenges remaining in designing and fabricating these cells.

In this project, a novel graphene/Si Schottky junction solar cell with a back-contact structure was fabricated to increase the active area and also enable a texturing process to be implemented on the front of Si substrates. With this structure, a graphene layer and contacts are placed on the back-side of Si substrates, which reduces the optical loss from the front contact. Thus, the active area of graphene/Si Schottky junction solar cells is increased, thereby leading to an improvement in the *PCE*. By applying the texturing process, the light reflected from the front of Si substrates is reduced, resulting in an additional increase in the *PCE*.

Two novel techniques were also developed to overcome the serious issue of the s-shape *J-V* behaviour in previous graphene/Si Schottky junction solar cells. It was shown that the removal of the PMMA residue left on graphene layers is critical to eliminate the s-shape in the *J-V* curves as this residue traps charge carriers, leading to the s-shape. In this case, formamide and deep UV (DUV) treatments were employed to transfer residue free CVD-graphene onto Si

substrates. By reducing the PMMA residue, devices displayed a noteworthy enhancement in the *PCE* compared with that of untreated devices.

As a result of reducing the PMMA residue and applying the texturing process, solar cells with *PCE* of 10% have successfully been fabricated. This value is a new record for graphene/Si solar cells prepared without chemical doping, and it is about 45% more than those for devices reported so far. To further enhance the device performance, the graphene layer was chemically p-doped, leading to a higher *PCE* of 14.1%. Hence, the achieved values of *PCE* in this work are comparable with those of conventional p-n junction solar cells. Additionally, there is a possibility to further improve the performance of graphene/Si Schottky junction solar cells by using multi-graphene layers instead of a monolayer. This further reduces the sheet resistance of transferred graphene layers, leading to a higher *PCE*. This work presents a feasible way to prepare simpler and higher performance graphene/Si Schottky junction solar cells that are able to sustain the positive influence of graphene in solar cell technology.

List of Abbreviations

a - Lattice unit vector

AFM - Atomic force microscope

AM - Air mass

α - Absorption coefficient

B - Coefficient of radiative recombination

BSR - Back Surface Reflector

BSRV - Back Surface Recombination Velocity

C_n - Auger coefficient for electrons

C_p - Auger coefficient for holes

CVD - Chemical vapour deposition

Cz - Czochralski

D - Carrier diffusivity

DI - Deionised

DLAR - Double layer anti-reflection coating

DR - Double resonant

DUV - Deep UV

E_g - Energy gap

EQE - External Quantum efficiency

FBZ - First Brillouin zone

FET - Field effect transistor

FF - Fill Factor

Φ_B - Schottky barrier height

GO - Graphene oxide

HIT - Heterojunction intrinsic thin-layer

I - Current

I_{Dark} - Dark current

I_L - Light current

J_{SC} - Short circuit current density

k - Boltzmann's constant

L - Carrier diffusion length

L - Channel length

LOR - Lift-off resist

λ - Wavelength

MGL - multi-graphene layers

μ - Carrier mobility

n - Ideality factor

n - Concentration of electrons

N_A - Acceptor concentration

N_D - Donor concentration

N_T - Trap Density

p - Concentration of holes

PCE - Power conversion efficiency

PECVD - Plasma Enhanced Chemical Vapour Deposition

P_{in} - Input power

P_{max} - Maximum power

PMMA - poly (methyl methacrylate)

PV - Photovoltaics

PVD - Physical vapour deposition

q - Electron charge

θ - Angle of the incident light

R_B - Back Surface Reflectance

R_c - Contact resistance

RF - Radio frequency

RIE - Reactive ion etching

σ_N - Electron capture cross-section

σ_p - Hole capture cross-section

S - Surface recombination velocities

SEM - Scanning electron microscope

SiO₂ - Silicon dioxide

SLAR - Single layer anti-reflection coating

SRV - Surface Recombination Velocity

T - Temperature

T - Lifetime of minority carriers

τ - Minority carrier Lifetime

U - Recombination rate

UV - Ultraviolet light

V - Voltage

V_{bi} - Built-in potential

V_{oc} - Open-circuit current density

XPS - X-ray photoelectron spectroscopy

W - Channel width

Contents

Abstract	i
List of Abbreviations	iii
List of Figures	xi
List of Tables	xvii
Acknowledgment	xviii
1 Introduction	1
1.1 Requirement of renewable energy/solar cells	1
1.2 Aim and Outline of Thesis	2
2 Overview of solar cell technologies	5
2.1 Photovoltaic effect	5
2.1.1 Absorption of photons in the materials	5
2.1.2 Separation of the generated carriers in the junction	7
2.1.3 Collection of charge carriers at the terminals of the junction	7
2.2 Current density-voltage (<i>J-V</i>) characteristics of solar cell	7
2.3 Loss Mechanisms	10
2.3.1 Electronic Loss:	10
2.3.2 Optical Loss:	17
2.4 Overview of state-of-the-art solar cell development	22
2.4.1 Single p-n junction solar cells.....	22
2.4.2 Schottky junction solar cells	30
3 Graphene, its properties and application in Schottky junction solar cells	32
3.1 Characteristics of graphene	32
3.1.1 Physical characteristics of graphene.....	32
3.1.2 Electronic properties of graphene	35
3.2 Growth of large area sheets of graphene by Chemical Vapour Deposition....	38
3.3 Wet transfer process.....	40
3.4 Application of CVD-graphene in Schottky junction solar cells.....	42
3.4.1 Graphene/Si Schottky junction solar cells with a top-window structure ..	42
3.4.2 Graphene/Si Schottky junction solar cells with a top-grid structure	47
4 Characterisation and experimental techniques	51
4.1 Characterisation techniques.....	51
4.1.1 Optical Microscope	51
4.1.2 Atomic Force Microscopy (AFM).....	52
4.1.3 Raman spectroscopy	53
4.1.4 X-Ray Photoelectron Spectroscopy (XPS).....	55

4.1.5	Nkd-7000 spectrophotometer	55
4.1.6	Scanning electron microscope.....	56
4.1.7	Key-sight B1500A semiconductor Analyzer	57
4.1.8	PVE300 photovoltaic external quantum efficiency system	59
4.2	Experimental techniques	59
4.2.1	Wet transfer process of CVD-graphene	59
4.2.2	Modified Photolithography and Lift-off.....	61
4.2.3	Modified RF magnetron sputtering Technique	63
4.2.4	Forming Cr adhesive layer using thermal evaporation technique.....	64
4.2.5	Modified Argon plasma etching process of CVD-graphene.....	65
4.3	Fabrication Process.....	66
4.3.1	Substrate cleaning process	66
4.3.2	Device Fabrication.....	67
5	Novel graphene/n-Si Schottky junction solar cells with a back-contact structure.....	69
5.1	Introduction.....	69
5.2	Graphene/n-Si Schottky junction solar cells based on a back-contact structure and an improved wet transfer process.....	70
5.2.1	Physical characteristics of transferred graphene using an improved wet transfer process.....	70
5.2.2	Electrical characteristics of transferred graphene using improved wet transfer process.....	73
5.2.3	Current density-voltage ($J-V$) characteristics of graphene/n-Si Schottky junction solar cells based on back-contact structure and improved wet transfer process	77
5.3	Graphene/n-Si Schottky junction solar cells based on back-contact structure and formamide treatment	85
5.3.1	Physical characteristics of transferred graphene using formamide treatment	86
5.3.2	Current density-voltage ($J-V$) characteristics of graphene/n-Si Schottky junction solar cells based on back-contact structure and formamide treatment....	89
5.4	Conclusion.....	98
6	Novel graphene/n-Si Schottky junction solar cells with a back-contact structure based on DUV treatment.....	100
6.1	Introduction.....	100
6.2	Novel wet transfer process based on DUV treatment.....	101
6.2.1	Physical characteristics of transferred graphene using DUV treatment	102
6.2.2	Electrical characteristic of transferred graphene using DUV treatment	104
6.3	Hysteresis of graphene-based field effect transistors (gFETs)	105

6.4	Current density-voltage (J - V) characteristics of graphene/n-Si Schottky junction solar cells based on back-contact structure and DUV treatment.....	110
6.5	Current density-voltage (J - V) characteristics of graphene/n-textured Si Schottky junction solar cells based on back-contact structure and DUV treatment	120
6.6	Conclusions	126
7	Conclusions and Further Work.....	128
7.1	Summary of Key results.....	128
7.2	Future work.....	131
	References:	133
	Appendix	142
1.	Publication and Presentations.....	142
1.1	Journal Publication lists	142
1.2	CONFERENCES	143
1.3	Awards	144
1.4	Teaching qualification	144
2.	Lithography Designs	144
2.1.	Designs for gFET devices.....	144
2.2.	Designs for graphene/Si Schottky junction solar cells.....	145
3.	Materials	147

List of Figures

Figure 2-1: Illustrating the absorption of a photon in a semiconductor with band-gap E_g .	6
Figure 2-2: Schematic band diagrams of (a) indirect band gap and (b) direct band gap.	7
Figure 2-3: Typical J - V characteristics of a solar cell in dark and under illumination.	9
Figure 2-4: Five common recombination sites at different regions of the solar cell. (1) Front interface. (2) n-doped region or the emitter. (3) Depletion region of the p-n junction. (4) p-doped region or the base. (5) Rear interface.	10
Figure 2-5: Radiative recombination process of an electron and a hole in a semiconductor.	12
Figure 2-6: Energy band of Auger recombination with the excess energy transferred to the conduction band electron (eeh) or valence band hole (ehh).	14
Figure 2-7: Energy band of recombination through a defect state.	15
Figure 2-8: Dangling bonds at a silicon surface.	17
Figure 2-9: Reflectance of planar Si wafers with and without antireflection coatings.	18
Figure 2-10: Ray diagram of normally incident light on a pyramid textured surface, showing the ray-paths of incident light.	19
Figure 2-11: AM 1.5G (IEC 60904-3) spectrum, showing the cumulative power over selected wavelength ranges [34].	21
Figure 2-12: Ray diagram light-trapping and the loss-cone for diffuse rear reflectors.	22
Figure 2-13: Schematic energy diagram of a p-n junction solar cell, illustrating photo-excited electron transfer.	23
Figure 2-14: Schematic cross-sectional view of a silicon solar cell with screen printed contacts [40].	24
Figure 2-15: Schematic cross-sectional view of an amorphous silicon single junction solar cell [40].	26
Figure 2-16: Schematic cross-sectional view of the HIT solar cell formed by Sanyo. The thickness of the crystalline silicon substrate was 200 μm , whereas the total thickness of intrinsic + p-type amorphous silicon layers on the top of the substrate was 10 nm and the total thickness of the intrinsic + n-type amorphous silicon on the underside of the substrate was 20 nm [43].	27
Figure 2-17: Schematic cross-sectional view of the HIT solar cell based on the back-contact structure [32].	28

Figure 2-18: Schematic of perovskite solar cell.	29
Figure 2-19: Schematic energy diagram of a Schottky junction solar cell, indicating the photo-excited electron transfer.	30
Figure 3-1: Sketch of graphene geometry in real and reciprocal space. Left: Hexagonal honeycomb lattice in real space, the vectors a_1 and a_2 and the atoms A and B define the Bravais lattice; Right: Corresponding Brillouin zone where Γ is the centre of the FBZ and K and K' are its corners; M is located on a side of the FBZ between K and K' point.	33
Figure 3-2: Raman spectrum of transferred CVD-graphene on SiO ₂ /Si substrate.	34
Figure 3-3: Sketch of the main Raman processes in graphene. (a) D band double resonant process involving a scattering from a defect. (b) and (c) G and 2D peaks generated through a second-order process, respectively.	35
Figure 3-4: Electronic dispersion in the honeycomb lattice. Left: energy spectrum (in units of t). Right: zoom in of the energy bands close to one of the Dirac points [74].	36
Figure 3-5: Structural diagram of a conventional graphene-based back-gated FET.	37
Figure 3-6: (a) and (b) Ideal (I_D - V_G) transfer and (I_D - V_G) output curves of the gFET, respectively.	38
Figure 3-7: Schematic illustration of the growth mechanisms of the CVD growth process of graphene films. (a) CVD growth process with a methane precursor. (b) Scheme of the mild oxidation and sequential reductive heat treatment before the CVD process [80].	39
Figure 3-8: Typical Raman spectrum of PMMA layer [111].	41
Figure 3-9: The Fabrication process of a graphene/n-Si Schottky junction based on a top-window structure [46].	43
Figure 3-10: Fabrication process of the external electric field doped graphene/Si Schottky solar cell [112].	45
Figure 3-11: Schematic structure of a graphene/Si Schottky junction solar cell based on the top-grid structure [105].	48
Figure 4-1: Optical Microscope (BH2 Olympus).	51
Figure 4-2: (a) Schematic of reflected and transmitted light from graphene/SiO ₂ /Si substrate. (b) Optical image of CVD-graphene transferred onto a SiO ₂ /Si substrate.	52
Figure 4-3: (a) Optical image of AFM system (PACIFIC NANOTECHNOLOGY). (b) Block diagram of AFM [148].	53

Figure 4-4: (a) Optical image of XPLORA Raman system with an Olympus BX41 microscope in Cleanroom. (b) Schematic of Raman scattering process, showing Stokes and Anti -Stokes Scatters.	54
Figure 4-5: Optical image of Nkd-7000 spectrophotometer.	56
Figure 4-6: Optical image of JEOL JSM-7001F field enhanced SEM.	57
Figure 4-7: (a) Optical image of Keysight B1500A semiconductor Analyzer. (b) Sketch of I_D - V_G and I_D - V_D measurements. (c) Sketch of a J - V measurement of the solar cell.....	58
Figure 4-8: Wet transfer process steps. (a) Commercial monolayer graphene is on both sides of 25 μ m Cu foil. (b) Coating of one graphene layer with PMMA. (c) Etching the graphene layer at the bottom side is by 10% HNO ₃ . (d) Etching of Cu foil is by 0.1 M Ammonium per-sulphate. (e) Floating of PMMA/graphene layers on DI-water. (f) Transferring of PMMA/graphene layers on the substrate (Si or SiO ₂ /Si substrate). (g) Removing the PMMA layer with acetone treatment.	60
Figure 4-9: Sketch of modified photolithography and lift-off process. (a) and (b) Coating of photoresist/LOR layers onto a graphene/desired substrate. (c) Exposing photoresist/LOR layers to UV. (d) Developing photoresist/LOR layers.	62
Figure 4-10: Optical Associates INC (OAI) instrument.....	63
Figure 4-11: (a) Optical image of three targets 8" sputtering machine (Nordiko Limited). (b) Schematic of conventional sputtering coating technique.	64
Figure 4-12: Optical image of Edwards 306 thermal evaporator.....	65
Figure 4-13: Schematic of improved argon plasma etching technique using the heat sink and improved photolithography process.	66
Figure 5-1: (a) and (b) Optical and AFM images of the transferred monolayer graphene onto SiO ₂ /Si substrate using improved wet transfer process, respectively.	71
Figure 5-2: (a) Raman spectrum of transferred graphene onto SiO ₂ /Si substrate. (b) C1s XPS data of transferred graphene on SiO ₂ /Si substrate, the blue peak corresponds to graphene, and others indicate PMMA residue.	72
Figure 5-3: (a) and (b) Optical pictures of graphene channels processed with standard lithography without and with LOR, respectively. (c) Optical picture of graphene channels processed with modified lithography processes. (d) Raman spectra of graphene channels patterned with and without modified lithography process.	74
Figure 5-4: (a) Schematic structure of a gFET. (b) and (c) Current-voltage (I_D - V_D) output curves of the gFETs with sputtered and evaporated adhesive layers. (d) Current-voltage (I_D - V_G) transfer curves of the gFETs with evaporated and sputtered adhesive layers.	76

Figure 5-5: Fabrication process of graphene/Si Schottky junction solar cells. (a) Si substrate after the cleaning process. (b) and (c) Transferring PMMA/graphene (Gr) onto the Si substrate using the improved wet transfer process. (d) Applying shaping process to obtain a 3.3×3.3 mm ² graphene area. (e) Creating Ag/Cr cathode. (f) Forming Au/Cr grid.	78
Figure 5-6: Schematic energy diagram of a device and photo-excited electron transfer, indication the photo-generation process which done at a Si substrate then electrons move in the opposite direction to that in the case of holes.	79
Figure 5-7: (a) <i>J-V</i> characteristics of graphene/Si Schottky solar cells treated with forming gas for different periods. (b) and (c) Improvements of V_{OC} , J_{SC} , FF and PCE of treated devices for different periods.	80
Figure 5-8: Raman spectrum of transferred graphene layers before and after annealing in forming gas for 2 h, showing 2D/G ratio around 1 after annealing.	82
Figure 5-9: (a) and (b) XPS and AFM data of transferred graphene, which was annealed in forming gas for 2 h, onto SiO ₂ /Si substrates, respectively.	83
Figure 5-10: <i>J-V</i> characteristics of chemical doped graphene/Si Schottky junction solar cells before and after the doping process.	84
Figure 5-11: (a) and (b) Optical and AFM images of transferred graphene surfaces, which was treated with formamide method, onto SiO ₂ /Si substrates, respectively.	86
Figure 5-12: Raman spectra of transferred graphene onto SiO ₂ /Si substrates before and after formamide treatment, showing a red shift in spectrum after this treatment.	87
Figure 5-13: XPS data of transferred graphene treated with formamide method onto SiO ₂ /Si substrates.	88
Figure 5-14: Fabrication process of graphene/Si Schottky junction solar cells based on formamide. (a) Si substrate after cleaning process. (b) Transferring PMMA/graphene (Gr) onto the Si substrate. (c) Immersing sample in formamide and followed by annealing in a hydrogen/argon environment for 2 h. (d) Applying shaping process to obtain a 3.3×3.3 mm ² graphene area. (e) Creating the Ag/Cr cathode. (f) Forming the Au/Cr grid.	89
Figure 5-15: <i>J-V</i> characteristics of graphene/Si Schottky solar cells before and after treating with formamide.	90
Figure 5-16: Current-voltage (I_D - V_D) output curves of the gFETs treated with formamide.	92
Figure 5-17: Current-voltage (I_D - V_G) transfer curves of the gFETs treated without and with formamide before the annealing process.	93
Figure 5-18: (a) <i>J-V</i> characteristics of graphene/Si Schottky solar cells treated with formamide for different periods before applying forming gas process for 2	

h. (b) and (c) Enhancements of V_{OC} , J_{SC} , FF and PCE of treated devices for different periods.	94
Figure 5-19: (a) and (b) Schematic energy band diagrams of graphene/silicon Schottky junctions treated without and with formamide before annealing process, respectively, indicating to the recombination process of generated carriers due to the trap states of PMMA residue.	96
Figure 5-20: Schematic structures of Si substrates with (a) SLAR and (b) DLAR coatings.	97
Figure 5-21: (a) Reflectance spectra of Si substrates with and without anti-reflective coatings. (b) J - V characteristics for the fabricated devices using Si substrates with antireflective coatings after formamide treatment for 30 min, annealing in forming gas for 2h and doping treatment of HNO_3 for 30 sec.	97
Figure 6-1: Schematic representation of the novel wet-transfer process, indicating the DUV irradiation treatment.	101
Figure 6-2: (a) and (b) Optical and AFM images of transferred graphene surfaces, which was treated with DUV irradiation, onto SiO_2/Si substrates, respectively.	102
Figure 6-3: (a) and (b) Raman spectrum and XPS data of graphene transferred with DUV method onto SiO_2/Si substrates, respectively.	103
Figure 6-4: Current-voltage (I_D - V_D) output curves of the gFETs treated with DUV.	105
Figure 6-5: Current-voltage (I_D - V_G) transfer curves measured in air at room temperature and $V_D = 10$ mV under forward and backward sweeps. (a) and (b) Untreated long and short channel devices. (c) and (d) DUV treated long and short channel devices.	106
Figure 6-6: (a) and (b) Shifting of neural point voltage of treated gFETs under repeating the electrical test at different recovery times in air at room temperature and $V_D = 10$ mV. (c) Current-voltage (I_D - V_D) output curves of treated gFETs in air at room temperature and $V_G = 5$ V. (d) Current-voltage (I_D - V_G) transfer curves of treated gFETs measured in air at room temperature and $V_D = 10$ mV after aging process.	108
Figure 6-7: Fabrication process of graphene/Si Schottky junction solar cells. (a) Si substrate after cleaning process and leaving in air for passivation process for 2h. (b) Transferring PMMA/graphene (Gr) onto the center of Si substrate. (c) Exposing PMMA/Gr to the DUV of 254 nm at 180 °C. (d) Removing PMMA layer by acetone treatment. (e) Applying shaping process and creating Ag/Cr cathode. (f) Forming Au/Cr grid.	111
Figure 6-8: (a) J - V characteristics for the graphene/Si Schottky solar cells fabricated with top-window and back-contact structures. (b) External quantum efficiency (EQE) spectra of devices fabricated with both structures.	112

Figure 6-9: Schematic of graphene/Si Schottky junction solar cells fabricated with (a) top-window structure and (b) back-contact structure, showing an enhancement of the active area of the device based on the back-contact structure, showing that the same area of graphene sheet as a junction was used for both fabricated devices.	113
Figure 6-10: (a) and (b) Improvements of V_{OC} , J_{SC} , FF , and PCE of irradiated devices by DUV for different periods.	114
Figure 6-11: XPS data of graphene transferred with DUV method onto SiO_2/Si substrates, respectively.	115
Figure 6-12: Raman spectra of transferred graphene onto SiO_2/Si substrates with DUV treatment between 20 and 65 min.....	116
Figure 6-13: J - V characteristics of graphene/n-Si Schottky junction solar cells treated with forming gas at 300 °C for 120 min and DUV at 180 °C for 65 min.	117
Figure 6-14: (a) and (b) XPS results of treated graphene on SiO_2/Si substrates with DUV at 180 °C for 65 min and forming gas at 300 °C for 120 min, respectively, the red peak corresponds to graphene, and the others indicate PMMA residue.	119
Figure 6-15: Reflectance spectra of textured Si substrates using different KOH/IPA/DI H ₂ O solutions at 75 °C for 45 min. A, B, C and D refer to processes displayed in Table 6-5.....	121
Figure 6-16: SEM images of textured Si substrates processed using different KOH/IPA/DI H ₂ O solutions at 75 °C for 45 min. A, B, C and D refer to processes displayed in Table 6-5.....	122
Figure 6-17: (a) Schematic of graphene/textured Si Schottky junction solar cell, indicating SiO_2 as the passivation layer. (b) J - V characteristics for graphene/textured Si devices before and after doping process of graphene/textured-Si Schottky. (c) and (d) Photovoltaic parameters of chemical doped graphene/Si Schottky junction solar cells during 9 days storage in air.	123

List of Tables

Table 5-1: The short-circuit current density (J_{SC}), open circuit voltage (V_{OC}), fill factor (FF) and power conversion efficiency (PCE) of graphene/Si devices treated with forming gas for different periods (average values reported)	81
Table 5-2: Comparison of photovoltaic parameters of graphene/Si solar cells reported with different structures.....	91
Table 5-3: The short-circuit current density (J_{SC}), open circuit voltage (V_{OC}), fill factor (FF) and power conversion efficiency (PCE) of treated graphene/Si devices with formamide for different periods (average values reported)	95
Table 5-4: Open-circuit voltage (V_{OC}), short-circuit current density (J_{SC}), fill factor (FF), and power conversion efficiency (PCE) of fabricated devices using Si substrates with and without anti-reflective coatings after formamide treatment for 30 min, annealing in forming gas for 2 h and doping process for 30 sec	98
Table 6-1: Sheet and contact resistances of graphene layers transferred with and without DUV treatment.....	104
Table 6-2: Difference in the threshold voltages (ΔV_{th}) for long and short channel devices treated with and without DUV irradiation under both sweeps in air at room temperature and $V_D = 10$ mV	106
Table 6-3: Shifting of neural point voltage of treated devices under both sweeps and repeating the electrical test at different recovery times (1, 10, 20, 50, 100, 200 and 500 s) in air at room temperature and $V_D = 10$ mV	109
Table 6-4: Open-circuit voltage (V_{OC}), short-circuit current density (J_{SC}), fill factor (FF) and power conversion efficiency (PCE) of treated graphene/Si devices with DUV for different periods (average Values reported).....	114
Table 6-5: Parameters of texturing processes for c-Si substrates processed using different KOH/IPA/DI H ₂ O solutions at 75 °C for 45 min.....	120
Table 6-6: Comparison of open-circuit voltage (V_{OC}), short-circuit current density (J_{SC}), fill factor (FF) and power conversion efficiency (PCE) of graphene/n-textured Si solar cells before and after doping process.	124
Table 6-7: The highest power conversion efficiency (PCE) reported to date for SGL/n-Si Schottky junction solar cells prepared without chemical doping and anti-reflection coating.....	125
Table 6-8: Open-circuit voltage (V_{OC}), short-circuit current density (J_{SC}), fill factor (FF) and power conversion efficiency (PCE) of doped graphene/Si devices during 9 days storage in air (average Values reported).....	125

Acknowledgment

Firstly, I would like to express my sincere appreciation to Iraqi government/HCED institution which support me by giving Ph.D. scholarship. The HCED institution were so helpful during my research. Additionally, I would like to thank my supervisor Professor Genhua Pan for his understanding and patience throughout my Ph.D. Genhua provided prompt support and valuable advice to enable me to improve the quality of my research. Further thanks go to my co-supervisor Dr David Jenkins for his continuous assistance and guidance on solar cell-related topics. Our discussions provided valuable knowledge which soon became essential throughout my project. The knowledge and skills gained throughout my PhD have provided me with the knowledge and practical experience I need to benefit me throughout my scientific career and my future research.

Special thanks are extended to Mr. Nick Fry, Dr. Bing Li, Dr. Kamrul Islam and Dr. Nasih Salah for sharing their time and invaluable expertise with me. Further thanks and acknowledgment go to the contributions of Ph.D. Dr. Brett Fisher at Surrey University for his support in the solar cell technology. I am deeply appreciative to all members of the Davey Building groups at Plymouth University for allowing me to use their facilities and for their assistance. I would like to express my thanks to Mr. Nick Fry. Nick consistently found the time to assist me and offer guidance throughout his busy schedule, sharing his practical skills which I have now been able to pass over to others.

My acknowledgment extends to my partners in Malaysia and Australia. I deeply appreciate their efforts for sharing their techniques to measure the J - V curve for solar cells. Furthermore, I would like to express my thanks to my friends and

colleagues. Owing to their friendship and continuous encouragement and support I've been able to overcome many frustrations and sadness.

Finally, I would like to give special thanks to my parents, brothers and sister for their love and understanding. I have had to spend the majority of my time on my work and unfortunately I have been unable to accompany them throughout my project. I am very proud of them and I now hope they can also be proud of me. I love you Mom and Dad.

Author's Declaration

At no time during the registration for the degree of Doctor of Philosophy has the author been registered for any other University award without prior agreement of the Doctoral College Quality Sub-Committee.

Work submitted for this research degree at the University of Plymouth has not formed part of any other degree either at Plymouth University or at another establishment.

This study was financed with the aid of a scholarship from the government of Iraq.

Relevant conferences were attended at which work was often presented and several papers prepared for publication.

Word count of main body of thesis: 37,900 words

Signed.....



Date...**01/08/2019**.....

1 Introduction

1.1 Requirement of renewable energy/solar cells

Human society has developed rapidly over the last hundred years, however at the cost of exhausting a huge amount of natural resources and causing severe environmental pollution. The greenhouse effect, an observed global temperature increase on earth, which is attributed to gas emission, primarily CO₂, into the atmosphere during the last two centuries, has attracted worldwide attention in recent years. One of the major reasons for the continuous increase of CO₂ emissions is the sharp rise of continuous demand for more energy, mainly due to steadily increasing demands from industry, transport and the demands of living. Therefore, it seems necessary to find renewable methods to meet this ever increasing demand for energy. Solar cells are one of the most promising candidates for sustainable and environmentally friendly energy sources because they convert sunlight directly into electricity without impacting on the environment. However, solar cells currently contribute to a very small fraction of the total world energy production because the energy produced by solar cells is about two to four times more expensive than the traditional energy sources. Hence, the research and development of solar cell technologies is a long-term project to develop continuous stable energy resources. Any single-element semiconductor substrate can actually form a Schottky junction solar cell with a metal [1]. Unfortunately, metals cause optical loss and decrease the solar cell efficiency because the reflectivity of metals is high. Therefore, transparent conducting oxides such as indium-tin-oxide (ITO) are used instead of metal in the fabrication process of Schottky junction solar cells [2, 3]. However, the limited resource of indium causes high production cost, and the diffusion of indium ions will cause a degradation of device performance. Furthermore, the brittle nature of ITO will limit

its application for flexible devices [4, 5]. Hence, graphene, which has flexible properties and high transparency, is used here to prepare Schottky junction solar cells [6, 7].

1.2 Aim and Outline of Thesis

The aim of this research is to prepare low-cost, stable and high-performance Schottky junction solar cells utilising the unique properties of graphene. To achieve that, the state-of-the-art of graphene/n-Si Schottky junction solar cells has been reviewed. This supports the development of a novel structure of the graphene/n-Si Schottky junction solar cell to overcome current issues of reported structures. To fabricate a graphene/n-Si Schottky junction solar cell with the new structure, four novel techniques for lithography, forming contacts, and transferring of CVD-graphene are developed. This thesis is divided into two distinctive parts. The first part is the background review section which includes chapters 2 and 3, provides a literature review on the solar cell technologies and the properties and application of graphene in Schottky junction solar cells. The second part is the experimental section, which includes chapters 4 to 7, which describes the experimental details and results in the fabrication process of a high efficiency graphene/n-Si Schottky junction solar cell.

The outline of this thesis is presented as follows:

Chapter 2 provides a comprehensive view of solar cell technologies. It discusses a photovoltaic process and the loss mechanisms in solar cells. It also explores the state-of-the-art of silicon solar cell development and the challenges faced to achieve high efficiency solar cells based on silicon substrates.

Chapter 3 focuses on graphene, its properties and application in Schottky junction solar cells. It also outlines the growth of graphene by chemical vapour deposition

(CVD) and the challenges of the wet transfer process of CVD-graphene. Additionally, it illustrates the current development of graphene/Si Schottky junction solar cells. In particular, it presents the challenges of graphene/Si Schottky junction solar cells fabricated with different structures.

Chapter 4 presents the characterisation and experimental techniques employed in this work. It shows the experimental setup and working mechanisms of equipment involved in the research. It also explains the novel techniques which are developed within the fabrication process of these devices.

Chapter 5 demonstrates a novel graphene/n-Si Schottky junction solar cell with a back contact structure. The results of novel techniques for shaping process and forming contacts, which are required to obtain solar cells with high efficiency, are displayed. It also shows the effect of PMMA residue on the characteristics of transferred graphene sheets and graphene/n-Si Schottky junction solar cell. An additional novel technique using formamide is presented to reduce the PMMA residue and suppress the s-shape in the J - V characteristics of solar cells, resulting in an improvement in the solar cell efficiency. The results of fabricated solar cells after enhancing p doping in graphene using HNO_3 and reducing the reflected light from silicon substrates by anti-reflection coatings (ARCs) are also mentioned.

Chapter 6 illustrates a novel technique using deep UV treatment which is employed in the wet transfer process to efficiently remove the PMMA layer from the transferred graphene surface, improve the properties of graphene and suppress the s-shape J - V behaviour in solar cells. It also shows the physical and electrical results of graphene layers transferred after the DUV treatment. Additionally, it displays the results of hysteresis in graphene-based field effect

transistors (gFETs). The effect of DUV irradiation on the performance of graphene/n-Si Schottky junction solar cells is also presented in this chapter. The results of the J - V characteristics of solar cells after applying the texturing and doping processes are shown.

Chapter 7 concludes and summarizes the major progress and results of this work, and it highlights the contribution of this work to knowledge and proposes potential future work to further develop solar cell technology.

Appendix illustrates the list of journal publications, conferences related to this project. Additionally, awards obtained during this research are presented. The detailed patterns of lithography photomasks and the used materials in this work are also demonstrated.

2 Overview of solar cell technologies

2.1 Photovoltaic effect

A solar cell is an electronic device that converts sunlight into electricity by the photovoltaic effect. In the photovoltaic effect, an electron will be excited from a valence band to a conduction band when this electron absorbs light with energy around the energy gap of a semiconductor. When this occurs a hole is also created within the valence band. This means that electron-hole pairs have been created by the incident light. The photovoltaic effect involves three processes:

- a) Absorption of photons in the material.
- b) Separation of generated carriers in the junction
- c) Collection of the charge carriers at the terminals of the junction [8].

2.1.1 Absorption of photons in the materials

When a solar cell is exposed to light, the material will absorb some of the incident light energy ($h\nu = E_f - E_i$). Electrons are excited from an initial energy level E_i to a higher energy level E_f as shown in Fig. 2.1. Electrons in the semiconductor can reside at energy levels below a valence band edge (E_v) or above a conduction band edge (E_c). There are no allowed energy states between the two bands which electrons can reside in [9]. The energy gap (E_g) is located between the maximum energy of the valence band and the minimum energy of the conduction band. The valence and conduction bands are not flat (see Fig. 2.2), and this depends on the value of a k-vector, which describes the crystal momentum (p) of a semiconductor material. According to the momentum value of the minimum edge of the conduction band and the maximum edge of the valence band, the semiconductor can have either an indirect band gap such as Si and Ge or direct

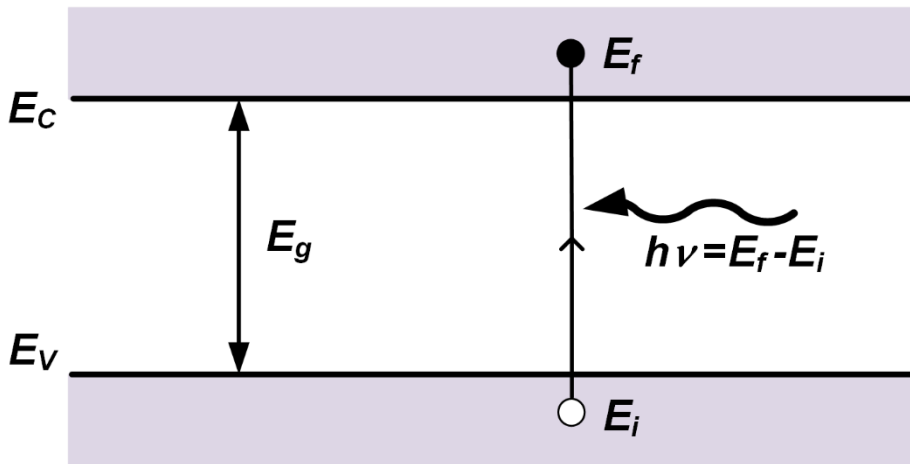


Figure 2-1: Illustrating the absorption of a photon in a semiconductor with band-gap E_g .

band gap such as InAs and GaAs as illustrated in Fig. 2.2. When an electron is excited from the valence band to the conduction band without a change in the crystal momentum, this semiconductor is a direct band-gap material. This means that both edges have the same momentum and the electron does not absorb a phonon to change its momentum. For indirect band-gap semiconductors, an electron can not be excited from the valence band to the conduction band without a change in crystal momentum. This indicates that both edges of the conduction and valence bands have different momentum [10]. In a solar cell application, indirect gap semiconductors are more preferable than the direct gap semiconductors as the indirect-gap semiconductors are lower cost. In addition, a radiative recombination process, which affects solar cell performance, is most likely to be in direct-gap semiconductors, whereas it is extremely low and almost negligible in indirect gap semiconductors [11]. This points out that the generated carriers are more than the recombined carriers, leading to an improvement in solar cell performance.

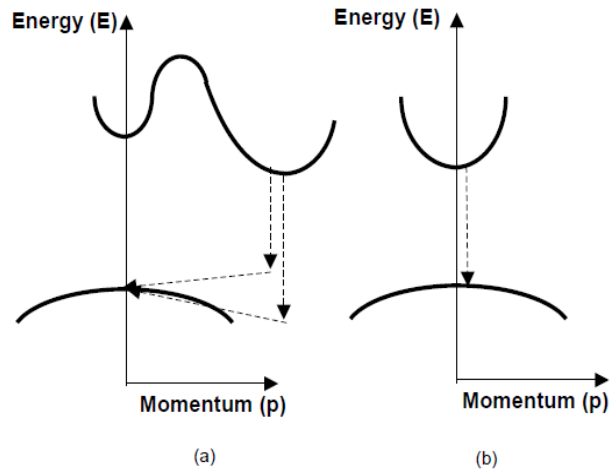


Figure 2-2: Schematic band diagrams of (a) indirect band gap and (b) direct band gap.

2.1.2 Separation of the generated carriers in the junction

After the creation of electron-hole pairs in a semiconductor, carriers should be separated to avoid returning electrons to an initial energy level E_i in the valence band and recombining with holes by a recombination process. In a solar cell, the pairs will be subsequently separated due to the action of the electric field existing at the p-n junction. This means that the period of separation process should be shorter than the carrier lifetime [12].

2.1.3 Collection of charge carriers at the terminals of the junction

When separated electrons and holes move to n-type and p-type layers respectively as a result of the built-in field across the junction, electrons will leave the solar cell through the electrical contacts. These electrons then recombine with the holes, which have been created in the valence band, and the chemical energy of the electron-hole pairs has been converted to electric energy [13].

2.2 Current density-voltage (J - V) characteristics of solar cell

Current density-voltage (J - V) characteristics of a solar cell can be measured after illuminating the solar cell under the standard test conditions (STC) of air mass

(AM) of 1.5 and an incident power density of 100 mW/cm^2 at $25 \text{ }^\circ\text{C}$. The value of the air mass at the Earth's surface can be obtained as:

$$AM = \frac{1}{\cos \theta} \quad (2.1)$$

where θ is the angle of the incident light [14]. The net output current of a solar cell is given by:

$$I = I_{\text{Dark}} - I_L = I_0 (e^{qV/nkT} - 1) - I_L \quad (2.2)$$

where I_{Dark} is a dark current of simple diode that describes the I - V relationship of a forward-biased diode, and it is composed of electrons from the electron-rich n+ emitter (n-type base) diffusing to the electron-poor p-type base. The drift current of photo-generated carriers flows in the opposite direction of that of the dark diffusion current. I_0 is called the saturation current density, q is the electronic charge, n is the ideality factor, k is Boltzmann's constant, T is the temperature in degrees Kelvin and I_L is the photocurrent. Fig. 2.3 shows typical J - V curves of the solar cell for the dark and under illumination conditions. It is clear that the J - V curve of a solar cell under a dark condition is the same as that for a diode J - V curve after accounting for the photocurrent. The photocurrent has a negative value as the direction of current flow is in the opposite direction of that for electrons. Therefore, equation 2.2 is can be rewritten as:

$$J = J_L - J_0 (e^{qV/nkT} - 1) \quad (2.3)$$

The photovoltaic parameters are also illustrated in Fig. 2.3. For example, J_{SC} is the short-circuit current density, which flows through the external circuit when the electrodes of the solar cell are short-circuited. The magnitude of the J_{SC} depends on the area of the solar cell and loss mechanisms described in section 2.2. V_{oc} is the open circuit voltage, and it refers to the maximum voltage that a solar cell can supply when there is no current in the external circuit.

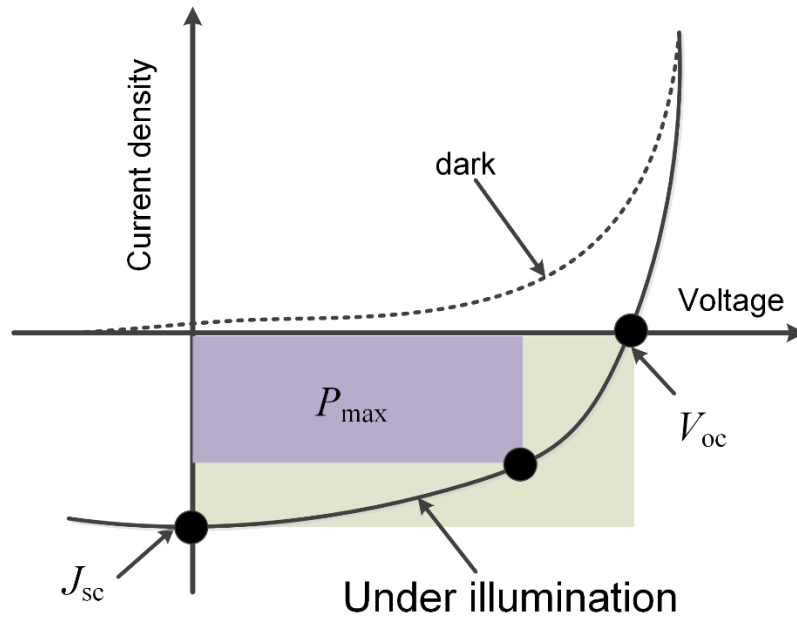


Figure 2-3: Typical J - V characteristics of a solar cell in dark and under illumination.

This value can be determined using the last equation, by assuming that the net current is equal to zero, as:

$$V_{oc} = \frac{kT}{e} \ln\left(\frac{J_L}{J_0} + 1\right) \quad (2.4)$$

It is clear from the above equation that V_{oc} depends on the photo-generated current and saturation current densities. In fact, V_{oc} is mostly affected by the saturation current density, which depends on the recombination losses in the solar cell. This means that an increase in either the dark diffusion current or the recombination current increases J_0 , and thus reduces J_{sc} and V_{oc} . The fill factor (FF) is defined as the ratio of the maximum power (P_{max}) generated by a solar cell to the product of V_{oc} and J_{sc} ,

$$FF = \frac{P_{max}}{V_{oc} J_{sc}} = \frac{V_{mP} J_{mP}}{V_{oc} J_{sc}} \quad (2.5)$$

Where the maximum power density (P_{max}) is shown by the rectangle area in this figure and is calculated from the product of the current density (J_{mP}) and voltage (V_{mP}) at the maximum power point. Finally, the power conversion efficiency (PCE)

of the solar cell is the ratio of the maximum output power (P_{max}) of a solar cell to the incident light power on the solar cell (P_{in}), which is 100 mW/cm² [15, 16].

$$PCE = \frac{P_{max}}{P_{in}} = \frac{V_{oc} J_{sc} FF}{P_{in}} \quad (2.6)$$

2.3 Loss Mechanisms

The loss mechanisms in solar cells can be divided into two types: electronic and optical losses.

2.3.1 Electronic Loss:

The electronic loss in a solar cell refers to the recombination process of electron-hole pairs at different regions of the solar cell according to the wavelength of the incident light as shown in Fig. 2.4. Recombination losses affect a short-circuit current and open circuit Voltage [16-18]. Actually, the recombination process of

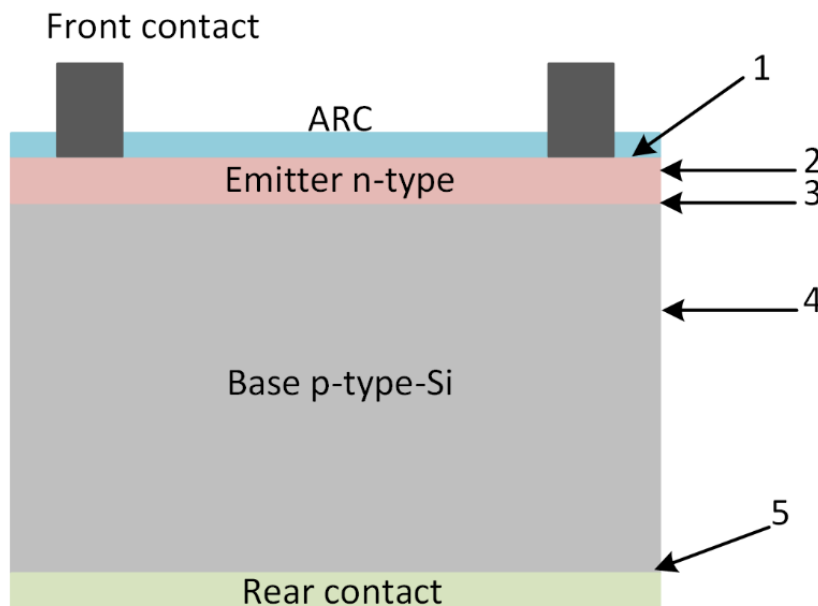


Figure 2-4: Five common recombination sites at different regions of the solar cell. (1) Front interface. (2) n-doped region or the emitter. (3) Depletion region of the p-n junction. (4) p-doped region or the base. (5) Rear interface.

electron-hole pairs in semiconductors will happen through four fundamental recombination mechanisms:

- Radiative recombination
- Auger recombination
- Shockley-Read-Hall recombination (SRH recombination).
- Surface Recombination

2.3.1.1 Radiative recombination

Radiative recombination, which is also known as a band-to-band recombination, is the attenuation of the generation process when a free electron drops directly from the conduction band into the valence band to recombine with a free hole. The difference in energy will be released as a photon (see Fig. 2.5). The rate of radiative recombination (U_{rad}) is given by equation 2.7, and it is proportional to the concentrations of electrons (in an n-type semiconductor) and holes (in a p-type semiconductor) in the conduction and valence bands.

$$U_{rad} = Bnp = B(\Delta n + n_o)(\Delta p + p_o) \quad (2.7)$$

Where B is the coefficient of radiative recombination, n and p are concentrations of electrons and holes in the n-type and p-type semiconductors after exposing to the light, respectively. The lifetime of radiative recombination (τ_{BB}) can be calculated as:

$$\tau_{BB} = \frac{\Delta n}{B \cdot (n_o + \Delta n) \cdot (p_o + \Delta p)} \quad (2.8)$$

Where Δn and Δp are photo-generated electrons and holes (injected carriers), n_o and p_o are the thermal equilibrium concentrations of free electrons and free holes, respectively. Consequently, the values of the radiative recombination lifetime at

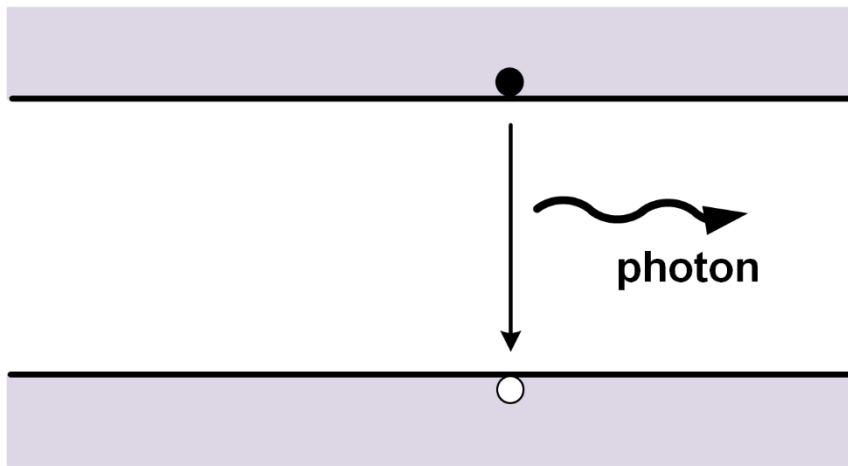


Figure 2-5: Radiative recombination process of an electron and a hole in a semiconductor.

different injection levels (a low injection level (*LLI*) and high injection level (*HLI*)) can be obtained as follows:

$$\tau_{BB,LLI} = \frac{1}{B \cdot N_{doped}} \quad \text{and} \quad \tau_{BB,HLI} = \frac{1}{B \cdot \Delta n} \quad (2.9)$$

Where N_{doped} refers to the concentration of acceptors and donors in p-type and n-type semiconductors, respectively. This means that the radiative recombination lifetime will stay constant for low injection levels while it decreases for medium and high injection levels. In an indirect band gap semiconductor such as crystalline Si, radiative recombination is smaller in comparison with other types of recombination as a result of requiring phonon generation to conserve momentum [19].

2.3.1.2 Auger recombination

The Auger recombination is an interaction $e^- e^- h^+$ or $e^- h^+ h^+$ as illustrated in Fig. 2.6. In this recombination loss, an electron in the conduction band will recombine with a hole in the valence band. Then, the third particle (electron or hole) will absorb the excess energy and become excited to a higher energy state. The Auger recombination rate (U_{Auger}) is the sum of both processes (U_{eeh} and U_{hhe}), and is given by:

$$U_{Auger} = U_{eeh} + U_{ehh} \quad \text{or} \quad U_{Auger} = C_n n^2 p + C_p n p^2 \quad (2.10)$$

Where C_n and C_p are the Auger coefficients for electrons and holes, respectively [20]. The Auger recombination lifetimes under the low injection level and high injection level can be determined as follows:

For p-type silicon

$$\tau_{Auger,LLI} = \frac{1}{C_p N_A^2} \quad \text{and} \quad \tau_{Auger,HLL} = \frac{1}{(C_n + C_p) \Delta p^2} \quad (2.11)$$

For n-type silicon

$$\tau_{Auger,light} = \frac{1}{C_n N_D^2} \quad \text{and} \quad \tau_{Auger,high} = \frac{1}{(C_n + C_p) \Delta n^2} \quad (2.12)$$

According to equations 2.10, 2.11 and 2.12, it can be observed that Auger recombination is great in heavily doped silicon than the radiative recombination. In addition, the Auger lifetime is inversely dependent on the carrier density squared, whereas the radiative lifetime linearly decreases with doping concentration. This means that Auger recombination is the dominant process in solar cell emitters and back surface fields [21, 22]. Furthermore, Auger recombination in heavily doped n-type Si is around three times stronger than in p-type silicon as the values of C_n and C_p are 2.8×10^{-31} and 9.9×10^{-32} cm⁶/s, respectively for silicon which has more than 5×10^{18} cm⁻³ dopant concentration. Therefore, solar cells based on p-type silicon, which have n-type emitters, are more affected by Auger recombination [20].

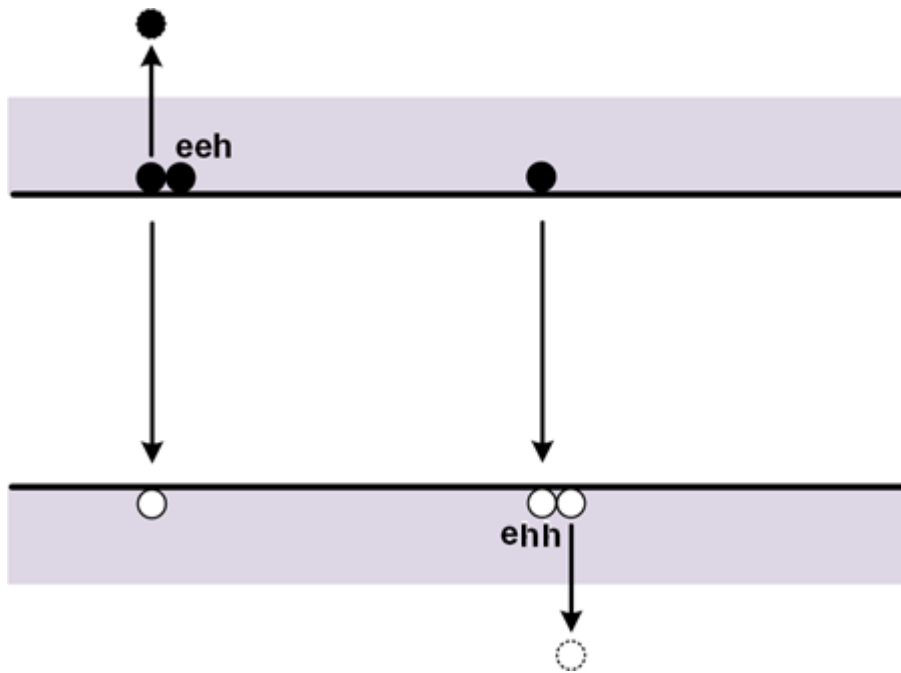


Figure 2-6: Energy band of Auger recombination with the excess energy transferred to the conduction band electron (eeh) or valence band hole (ehh).

2.3.1.3 Shockley-Read-Hall recombination (SRH recombination)

Defect states at the forbidden band of a semiconductor can also increase the probability of recombination losses. These defect states are due to impurities and crystal defects in the semiconductor lattice. In this process, an excited electron will lose its energy when it is trapped as shown in Fig. 2.7, and this electron will recombine with a hole in the valence band. This type of recombination is usually in a material with a high defect density. The dynamics of this process was first discovered by Shockley, Read and Hall, and therefore, it is known as SRH recombination theory. The SRH recombination rate (U_{SRH}) is determined by

$$U_{SRH} = \frac{np - n_i^2}{\tau_{po}(n + n_1) + \tau_{no}(p + p_1)} \quad (2.13)$$

Where τ_{no} and τ_{po} are lifetimes for electron and hole respectively. Lifetimes, which are related to the thermal velocity (v_{th}), the trap density (N_t), and the cross-section for electrons (σ_n) and holes (σ_p) capture, are obtained by:

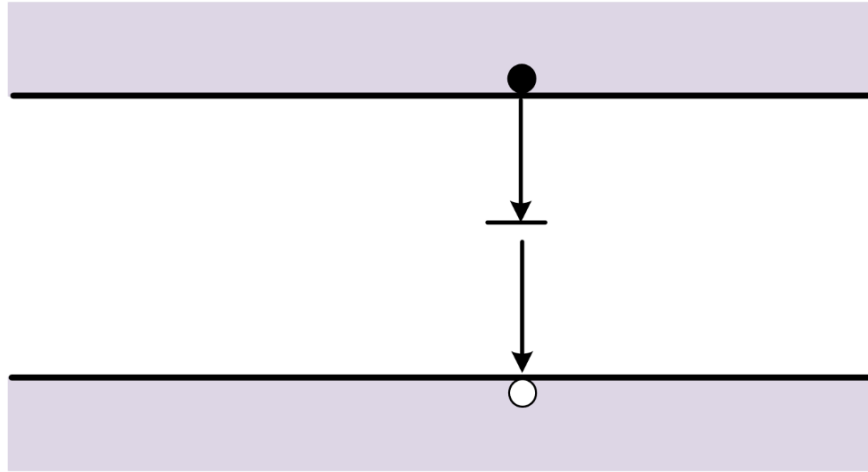


Figure 2-7: Energy band of recombination through a defect state.

$$\tau_{po} = \frac{1}{\sigma_p v_{th} N_t} \quad \text{and} \quad \tau_{no} = \frac{1}{\sigma_n v_{th} N_t} \quad (2.14)$$

The cross-section factors are related to the probability of defect states that will capture the carriers. The concentration of electrons (n_1) and holes (p_1), which will be trapped, are given by:

$$n_1 = n_i \exp\left(\frac{E_t - E_i}{KT}\right) \quad \text{and} \quad p_1 = n_i \exp\left(\frac{E_i - E_t}{KT}\right) \quad (2.15)$$

Where n_i and E_i are the intrinsic carrier concentration and the intrinsic energy level respectively, T is the temperature and k is the Boltzmann constant. Consequently, the lifetime of SRH recombination can be written as follows

$$\tau_{SRH} = \frac{\tau_{po}(n + n_1) + \tau_{no}(p + p_1)}{n_o + p_o + \Delta n} \quad (2.16)$$

Therefore, the expressions of the SRH recombination lifetime under low and high injection levels are as follows:

$$\text{n-type Si} \quad \tau_{SRH,LLI} = \tau_{po} + \frac{\tau_{no}(\Delta n + p_1)}{N_D} \quad \text{and} \quad \tau_{SRH,HLI} = \tau_{no} + \tau_{po} \quad (2.17)$$

$$\text{p-type Si} \quad \tau_{SRH,LLI} = \tau_{no} + \frac{\tau_{po}(\Delta n + n_1)}{N_A} \quad \text{and} \quad \tau_{SRH,HLI} = \tau_{no} + \tau_{po} \quad (2.18)$$

For traps which are located at the middle of the band gap ($E_t \cong E_i$), both n_1 and p_1 are small and equal to n_i . Therefore, the SRH lifetime under low injection level can be expressed as:

$$\text{n-type Si} \quad \tau_{SRH,LLI} = \tau_{po} \quad \text{for mid-gap traps} \quad (2.19)$$

$$\text{p-type Si} \quad \tau_{SRH,LLI} = \tau_{no} \quad \text{for mid-gap traps} \quad (2.20)$$

It is clear that the SRH lifetime has a minimum value when the traps are located at the middle of a band gap [11, 23].

2.3.1.4 Surface Recombination

Surface recombination can play a vital role in the solar cell performance. The main reason for this recombination is dangling bonds at the silicon surface as shown in Fig 2.8. These dangling bonds are a result of the discontinuity in the crystalline structure at the silicon surfaces. The dangling bonds cause a large density of defect states within the band gap of the semiconductor. The Surface recombination rate (U_s) is given by

$$U_s = \frac{n_s p_s - n_i^2}{\frac{n_s + n_1}{S_{po}} + \frac{p_s + p_1}{S_{no}}} \quad (2.21)$$

Where n_s and p_s are the concentrations of electrons and holes at the substrate surface. S_{no} and S_{po} factors refer to the surface recombination velocities for electrons and holes respectively. The relation between the capture cross-sections (σ_p and σ_n) and surface recombination velocities can be calculated by

$$S_{po} \equiv \sigma_p v_{th} N_{st} \quad (2.22)$$

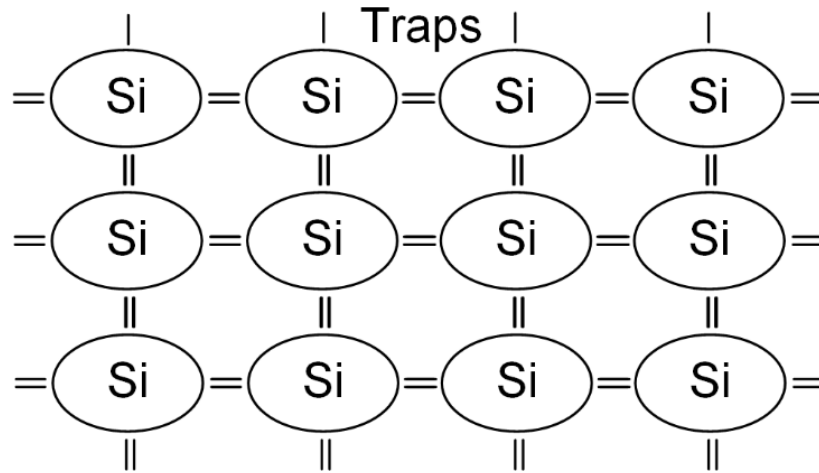


Figure 2-8: Dangling bonds at a silicon surface.

$$S_{no} \equiv \sigma_n v_{th} N_{st} \quad (2.23)$$

Where N_{st} is the density of surface states per unit area [18]. There are two processes that can actually reduce surface recombination loss:

a) Passivation process

Surface recombination can be reduced by forming a dielectric layer, such as silicon oxide; on the silicon surface in order to passivate the dangling bonds. Therefore, the density of the interface states and the magnitude of the capture cross-sections will be reduced. In addition, the passivation process will increase the open circuit voltage V_{OC} and solar cell efficiency [24].

b) Excess concentration of minority carriers

The issue of dangling bonds at a silicon surface can also be reduced by the excess concentration of minority carriers at the silicon surface. This option can be realised by increased doping of the semiconductor surface to repel the minority carriers at the silicon surface [16].

2.3.2 Optical Loss:

In a typical silicon solar cell, the main optical losses can be classified into:

- Reflection at the front surface.
- Absorption in anti-reflection coatings.

- Free carrier absorption in heavily doped regions.
- Absorption at the rear contact.
- Reflection of the rear surface.

2.3.2.1 Reflection at the front surface

The optical loss in this mechanism is due to the reflection from front grid electrodes and silicon substrates. The reflection of grid electrodes reduces the photo-generation process within wavelength range 500-1000 nm. The Fresnel reflection at the silicon surface is about 39% as silicon has a high coefficient index over the wavelength range (300nm -1000 nm) compared to air as shown in Fig. 2.9. This reflection can be reduced by antireflection coatings (ARC)

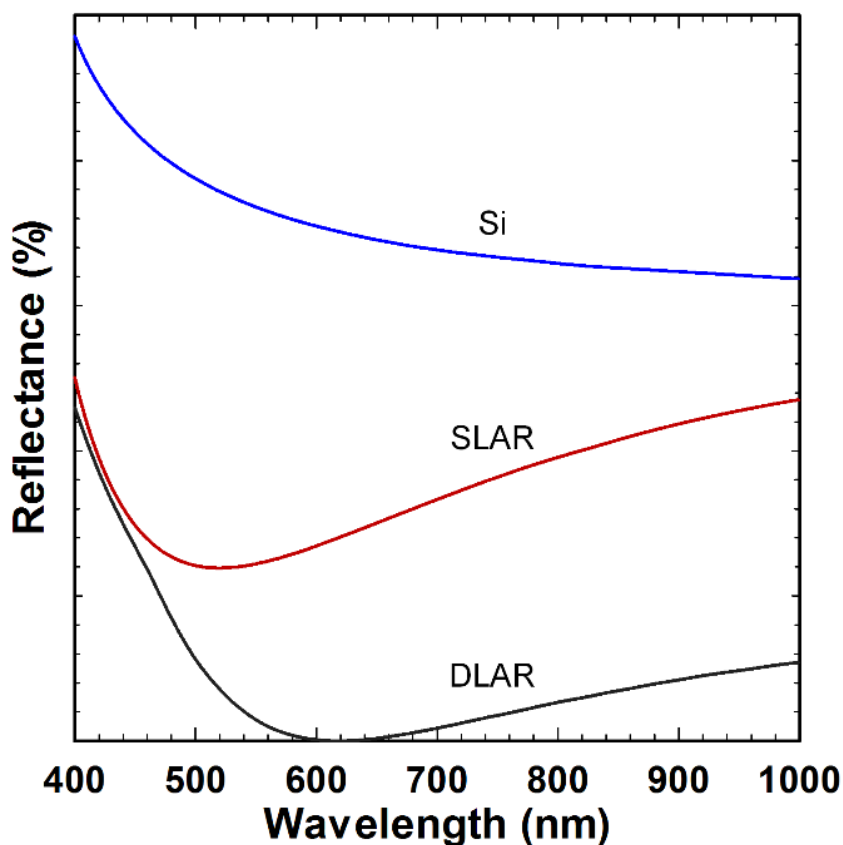


Figure 2-9: Reflectance of planar Si wafers with and without antireflection coatings.

[32]. For example, a single layer anti-reflection coating (SLAR) such as silicon dioxide (SiO₂) and double layer anti-reflection coating (DLAR) such as SiO₂/titanium dioxide (TiO₂) are formed on Si substrates. The thickness of the SiO₂ layer for SLAR coating should be equal to one quarter the wavelength of the incoming wave (i.e. $d_{SiO_2} = \lambda_0/4n_{SiO_2}$, where λ_0 is the mid-range wavelength of 500 nm, n_{SiO_2} and d_{SiO_2} represent the refractive index and thickness of SiO₂ layer, respectively) [25]. To achieve zero reflectance using DLAR coatings, the thickness of SiO₂ and SiO₂/TiO₂ layers should satisfy following equations [26]:

$$\frac{n_1 d_1}{\lambda_0} = \frac{1}{2\pi} \tan^{-1} \left\{ \pm \left[\frac{(n_s - n_0)(n_0 n_s - n_2^2) n_1^2}{(n_1^2 n_s - n_0 n_2^2)(n_1^2 - n_0 n_s)} \right]^{1/2} \right\} \quad (2.24)$$

$$\frac{n_2 d_2}{\lambda_0} = \frac{1}{2\pi} \tan^{-1} \left\{ \pm \left[\frac{(n_s - n_0)(n_0 n_s - n_1^2) n_2^2}{(n_1^2 n_s - n_0 n_2^2)(n_2^2 - n_0 n_s)} \right]^{1/2} \right\} \quad (2.25)$$

Where d_1 and d_2 represent the thickness of the TiO₂ and SiO₂ layers, respectively. Parameters of n_0 , n_1 , n_2 and n_s refer to the refractive index of air, TiO₂, SiO₂ and substrate, respectively. Texturing is also employed to effectively reduce the light reflected from silicon substrates to below 15% [27-29]. Moreover, more light is absorbed due to multiple interactions as shown in Fig. 2.10 [30].

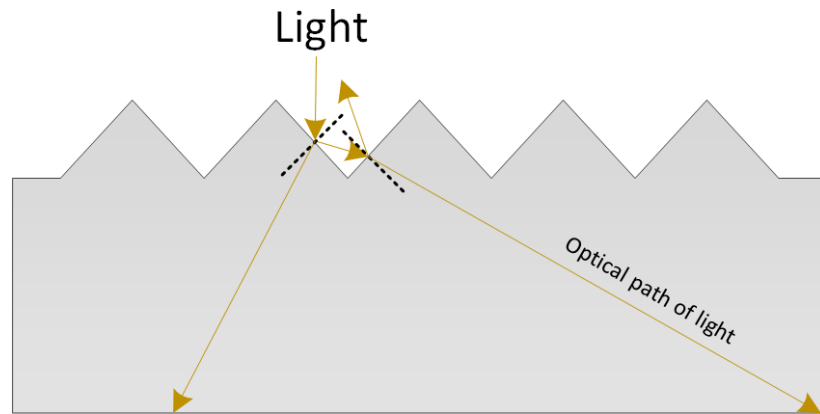


Figure 2-10: Ray diagram of normally incident light on a pyramid textured surface, showing the ray-paths of incident light.

2.3.2.2 Parasitic absorption in anti-reflection coatings

The Beer-Lambert law describes the light absorption through a material as follows

$$I(x) = I_0 e^{-\alpha x} \quad (2.26)$$

Where I_0 is the intensity of the incident light, $I(x)$ is the intensity of light in the absorbing material at depth (x), and α is the absorption coefficient which is a function of the extinction coefficient (k) of the material and wavelength (λ). The absorption coefficient is obtained as [31] :

$$\alpha = \frac{4\pi k}{\lambda} \quad (2.27)$$

ARC materials absorb some of the incident light with a wavelength range (300-500 nm) [32], and this results in an optical loss. Therefore, antireflection layers should have negligible absorption over that wavelength range. For example, SiO₂ and SiN_x are the best common ARC materials used in the fabrication process of Si solar cells to reduce that effect [31].

2.3.2.3 Parasitic free carrier absorption

Free carrier absorption (FCA) processes arise when an electron (hole) in the conduction (valence) band of semiconductor transits to a higher (lower) energy state within the same conduction (valence) band. Therefore, this process will not contribute to the photocurrent, as the absorbed energy is lost because of thermalisation processes. FCA process can be neglected in silicon for wavelengths less than 1000 nm, while it can become significant for longer wavelengths, particularly in regions with high carrier concentrations as it will increase the absorption of long wavelength light [33].

2.3.2.4 Reflection of back silicon substrate

Silicon has weak absorption at wavelengths beyond 1 μm . In fact, the wavelength range (850-1200 nm) for incident light holds around 25% of the optical energy in the AM 1.5 spectrum as shown in Fig. 2.11. This means that silicon substrate should be thick enough to completely absorb light up to 1100 nm, as silicon has a band gap of 1.12 eV. This can also be achieved by using the half wafer thickness when the rear side of the solar cell device is coated with highly reflective metals such as silver or aluminum. This technique will enhance the absorption of light as shown in Fig. 2.12 [30]. To further reduce the effect of this reflection, the special back surface reflector (BSR) called a Lambertian back reflector is employed. In this case, BSR will randomize the direction of the reflected light as shown. This allows incident light at the back surface to be reflected within the silicon substrate. Furthermore, the light will be totally reflected at the top surface of the silicon substrate when the angle of incident light at the top surface is greater

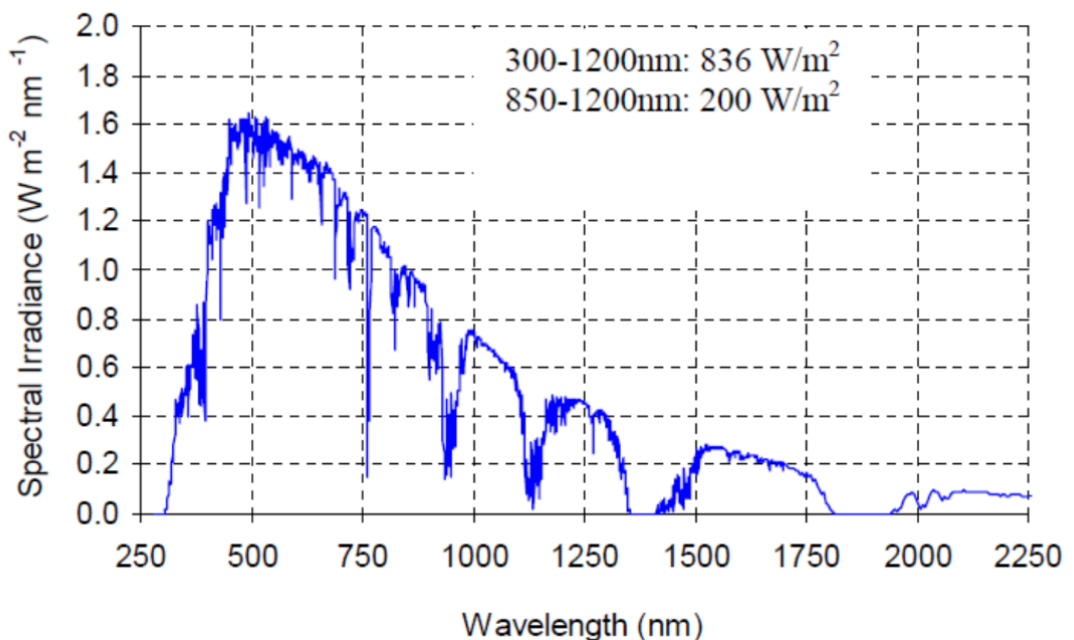


Figure 2-11: AM 1.5G (IEC 60904-3) spectrum, showing the cumulative power over selected wavelength ranges [34].

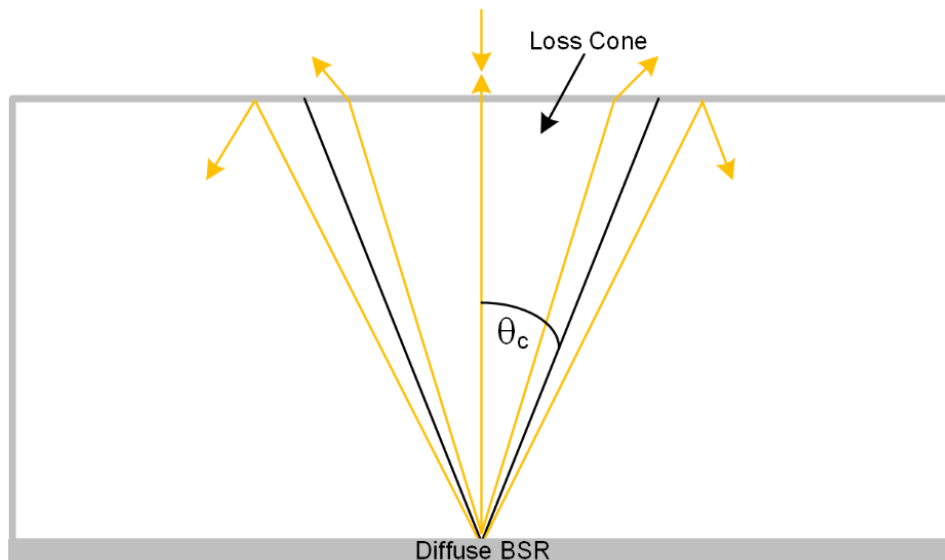


Figure 2-12: Ray diagram light-trapping and the loss-cone for diffuse rear reflectors.

than the critical angle (θ_c) [34, 35]. This means that the light path length is enhanced by a factor up to $4n^2$, where n is the refraction index of the silicon substrate [36]. Therefore, this technique will also reduce the cost of the fabrication process because a thinner silicon substrate is used to absorb the same amount of that light which is absorbed by the thick silicon substrate as a result of the increase in the optical path length.

2.4 Overview of state-of-the-art solar cell development

2.4.1 Single p-n junction solar cells

In this case, incident light is converted into electricity by a p-n semiconductor junction solar cell as shown in Fig. 2.13. Electron-hole pairs, which are generated, are then separated by the electric field, and the electrons and holes will move in opposite directions towards the electrodes, resulting in the generation of the photocurrent [37, 38]. Many types of high efficiency solar cells devices based on a p-n junction have been reported. In the next sections, the focused will be on silicon, III-V compounds and perovskite solar cells.

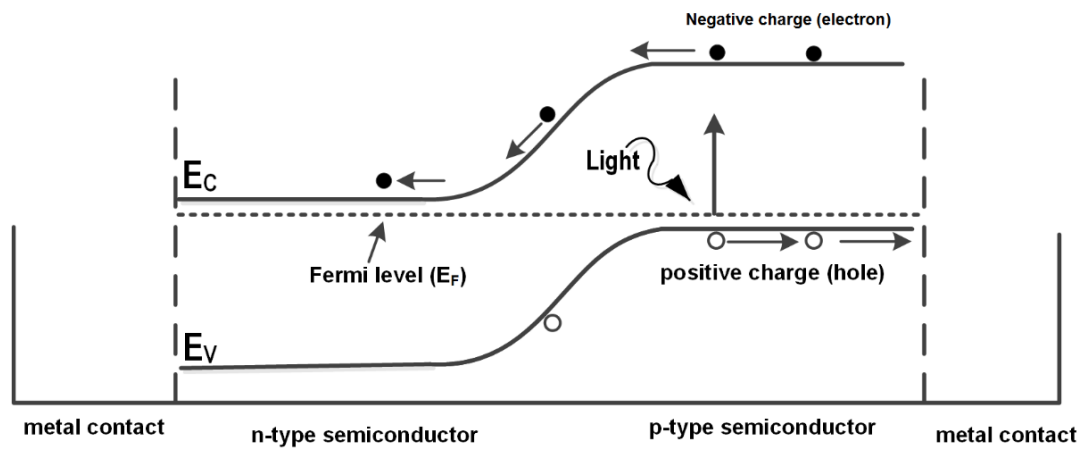


Figure 2-13: Schematic energy diagram of a p-n junction solar cell, illustrating photo-excited electron transfer.

2.4.1.1 Silicon solar cells

2.4.1.1.1 Single crystalline silicon solar cells

Single crystalline silicon has been used as a substrate to fabricate monocrystalline silicon solar cells. Crystalline silicon has an indirect energy band gap that is around 1.1 eV at room temperature. The indirect energy band gap results in a low optical absorption coefficient, $\alpha \approx 100 \text{ cm}^{-1}$. In other words, the silicon thickness in this kind of solar cell is required to be several hundred microns thick ($\gg 1/\alpha$) to absorb most incident light. Electron-hole pairs, which are generated by the light, should be able to reach the electric field in the depletion region of the junction in order to contribute to the photocurrent. This is achieved by diffusion of the carriers to the junction region and is measured by the diffusion length (L) of a minority carrier which moves between generation and recombination stages. Since carriers are generated through whole Si substrates dependent on a wavelength of the incident light, the number of carriers reaching the junction is large when these carriers have long diffusion length. This results in high solar cell performance. The diffusion length is shown by elementary semiconductor theory as follows:

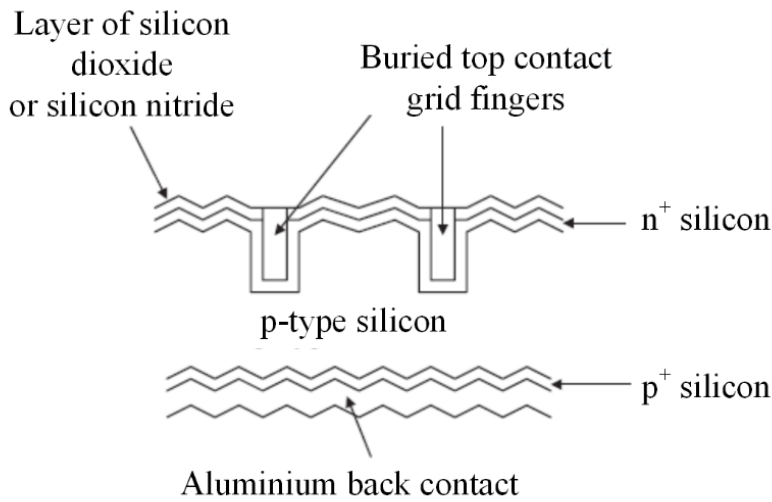


Figure 2-14: Schematic cross-sectional view of a silicon solar cell with screen printed contacts [40].

$$L \propto \sqrt{T\mu} \quad (2.28)$$

Where μ is the mobility and T is the lifetime of minority carriers in the light absorbing region [39]. Because μ and T are sensitive to material quality, so solar cells should be prepared using materials such as crystalline silicon, which has less defects, to obtain high solar cell efficiency. Fig. 2.14 shows a cross-sectional view of the conventional silicon solar cell structure [40]. The boron doped p-type monocrystalline silicon wafer has been used as a substrate. In order to fabricate the p-n junction solar cell, the doped phosphorus impurities are diffused into the silicon wafer. A screen-printed silver technique for contact fingers has been used on the n-type surface instead of metals to allow light to transmit into the junction region and reduce optical losses. The second issue of this cell is the high reflectivity of silicon substrates (as mentioned in the 2.2.2.1 section). The silicon surface has been textured to minimize the reflection and to enhance the path length of the light within the silicon substrate. An antireflection coating layer (ARC), which is titanium dioxide, is deposited over the top contact fingers to

reduce the effect of the reflection from the silicon substrate. The efficiency of this cell is about 12.8% [41].

2.4.1.1.2 Polycrystalline silicon solar cells

To reduce the cost of previous solar cells, polycrystalline Si is used within the fabrication process of solar cells to form a junction with a Si substrate. Plasma Enhanced Chemical Vapour Deposition (PECVD) is used to form a high-quality polycrystalline layer over crystalline silicon substrates. In this technique, hydrogen gas plays an important role in the passivating process for the dangling bonds and reduces grain boundaries. There are many advantages of using polycrystalline such as lower capital costs, higher throughput, less sensitivity to the quality of the silicon feedstock used and higher packing density of cells to make a module because of the square or rectangular shape of the cells. Silicon nitride as antireflection coating layer is also fabricated by PECVD. The average efficiency of the cell is about 12.6%, which is actually not very different from that efficiency of single crystalline silicon cells [40].

2.4.1.1.3 Amorphous silicon solar cells

A hydrogenated amorphous silicon (a-Si: H) layer is deposited on crystalline silicon to form a junction solar cell. Hydrogen gas also plays the important role in the passivating process for dangling bonds on the surface of a silicon substrate. In addition, the hydrogenated amorphous silicon is found to have a direct optical energy band gap of 1.7 eV and an optical absorption coefficient $\alpha > 10^5 \text{ cm}^{-1}$ for photons with energies greater than the energy band gap. This means that only a few microns of material are required to absorb most of the incident light. Furthermore, this technique will reduce the fabrication cost. The efficiency of this cell was about 12%. The main issue of this cell is the doping level of this layer which will reduce the mobility and lifetime of minority carriers in an amorphous

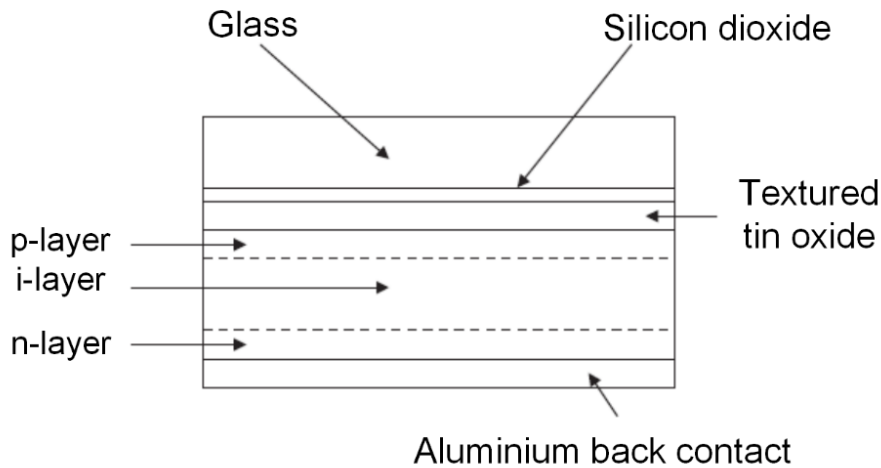


Figure 2-15: Schematic cross-sectional view of an amorphous silicon single junction solar cell [40].

silicon layer. This issue has been avoided by using a p-i-n device structure with a different energy bandgap i-layer. In this case, an intrinsic Si layer (i-layer) is introduced between the p and n-types Si. Fig. 2.15 shows the cross-sectional view of a typical p-i-n solar cell structure. Although the initial efficiency of this cell made in the laboratory is >12%, this value degrades to around 5% when a device is exposed to sunlight over a period of months. This phenomenon is known as Staebler-Wronski effect [42].

2.4.1.1.4 Heterojunction intrinsic thin-layer solar cell

Heterojunction intrinsic thin-layer (HIT) solar cells are prepared by using multiple p-i-n structures. In this structure, intrinsic thin amorphous silicon layers are deposited on both sides of crystalline silicon substrates as shown in Fig. 2.16. Then, p and n-type Si layers are coated on i-layers. Many advantages have been demonstrated with the structure of the HIT solar cells. For instance, the absorption of the solar spectrum is more efficient since the Si substrate, p and n-type Si layers have different energy gaps, resulting in an improvement in solar cell efficiency to 21%. Additionally, this cell is more stable compared with that of the previous solar cell as the multiple p-i-n junctions have been used. It also offers

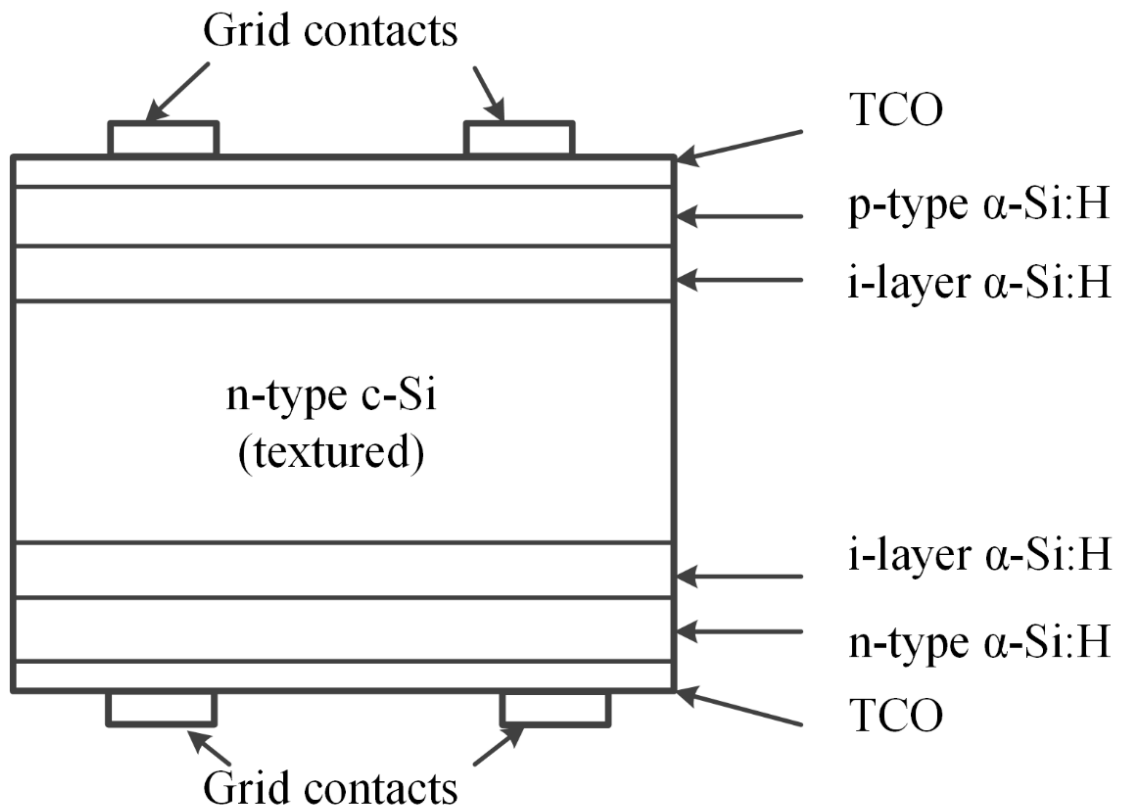


Figure 2-16: Schematic cross-sectional view of the HIT solar cell formed by Sanyo. The thickness of the crystalline silicon substrate was 200 μm , whereas the total thickness of intrinsic + p-type amorphous silicon layers on the top of the substrate was 10 nm and the total thickness of the intrinsic + n-type amorphous silicon on the underside of the substrate was 20 nm [43].

a better temperature coefficient in comparison with crystalline silicon solar cells [44]. In addition, the dangling bonds at the crystalline silicon surface have been successfully reduced by the intrinsic amorphous silicon layers. Therefore, the use of the a-Si (i) has provided a higher open circuit voltage. Although HIT solar cells have many advantages, there are some disadvantages. The first challenge is the absorption loss due to the ITO and metal layers, where the optical loss by the electrode is in the wavelength range (500 nm-1000 nm). At the same time, the ITO film absorbs the incident light in the wavelength range (300 nm-500 nm). The second issue is that the temperature for fabrication of this cell should be lower

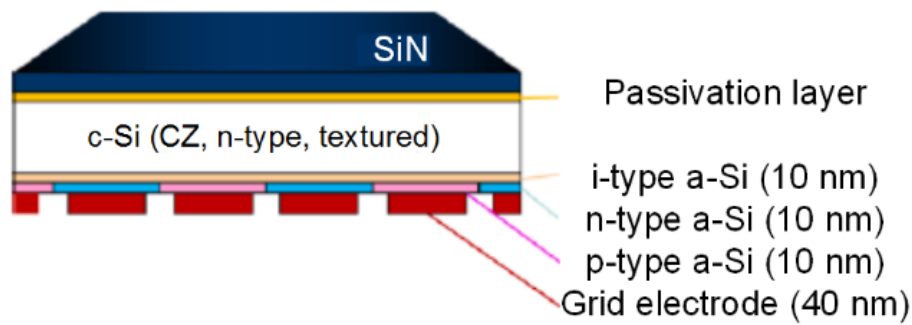


Figure 2-17: Schematic cross-sectional view of the HIT solar cell based on the back-contact structure [32].

than 200 °C for all films to reduce defects. Furthermore, the fabrication cost of this type of solar cell is high [45]. To reduce the optical loss for electrodes, HIT solar cells based on back contact structure has been fabricated as shown in Fig. 2.17. In this case, coated layers and electrodes are formed on the backside of Si substrates. The efficiency improved to around 25% for a fabricated device [32].

2.4.1.1.5 III-V compound Solar cells

III-V compounds such as indium phosphide (InP), gallium arsenide (GaAs) and gallium antimonide (GaSb) have several advantages such as a direct energy bandgap and a high optical absorption coefficient, which are crucial factors for achieving high solar cell efficiency [46]. In particular, GaAs and InP have widely been used in the fabrication process of solar cells since these materials have near optimum bandgap values for single-junction conversion of the solar spectrum [47, 48]. The highest obtained efficiency is about 21% for GaAs/InP solar cells [49]. Although III-V material solar cells have higher efficiency than those of Si solar cells based on a p-n junction, the cost of these cells is very high. Thus, these cells are not ideal for the industrial application.

2.4.1.1.6 Perovskite solar cells

As an alternative to the all solid state solar cells in the previous sections, organic-inorganic halide perovskite materials are used to prepare low cost and high efficiency perovskite solar cells (PSCs). The most commonly studied perovskite absorber is methylammonium lead trihalide ($\text{CH}_3\text{NH}_3\text{PbX}_3$), where X is a halogen atom such as iodine, bromine or chlorine. The optical bandgap of this material can be changed between 1.5 and 2.3 eV depending on the halide content [50, 51]. The fabrication process of this type of solar cell is simple, which can be achieved in any traditional lab environment. Fig. 2.19 shows the block diagram structure of this cell. The charge carriers are generated in a perovskite layer. Then, holes and electrons will move to the hole and electron interface layers, respectively. In this case, PEDOT:PSS or the PTAA-class of polymers are employed as hole interface layers, while PCBM, C_{60} , ZnO and TiO_2 are used as electron interface layers. The PSC efficiency has significantly been improved from 3.8% to about 22 % since 2009 [52, 53]. Unfortunately, these solar cells have many drawbacks such as instability, J - V hysteresis and lead toxicity.

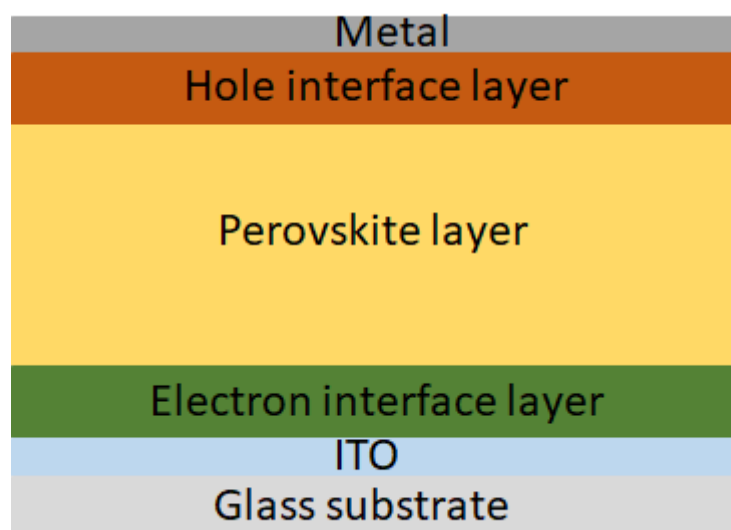


Figure 2-18: Schematic of perovskite solar cell.

In fact poor stability is a serious issue in solar cells, which will also make PSCs undesirable in the industrial application. Currently, researchers are working to fix those challenges, which could lead to a great progress in the future of solar cell technology [50].

2.4.2 Schottky junction solar cells

In previous sections, the p-n junction has been used to form solar cells. Although the efficiency of fabricated cells is high, it still costs a lot from in terms of materials and processing. Thus, the focus is on a way to manufacture solar cells that can scale up and lower costs. It was stated that the fabrication process of Schottky junction solar cells is simpler than that of p-n junction solar cells. In this case, a single-type semiconductor such as silicon can form a Schottky junction solar cell with a metal if there is enough difference between their work functions as shown in Fig. 2.18 [1]. It can be observed that the generation process of charge carriers is achieved throughout the Si substrate. The issue of this structure is that there is high absorption by the metal layer, resulting in an optical loss.

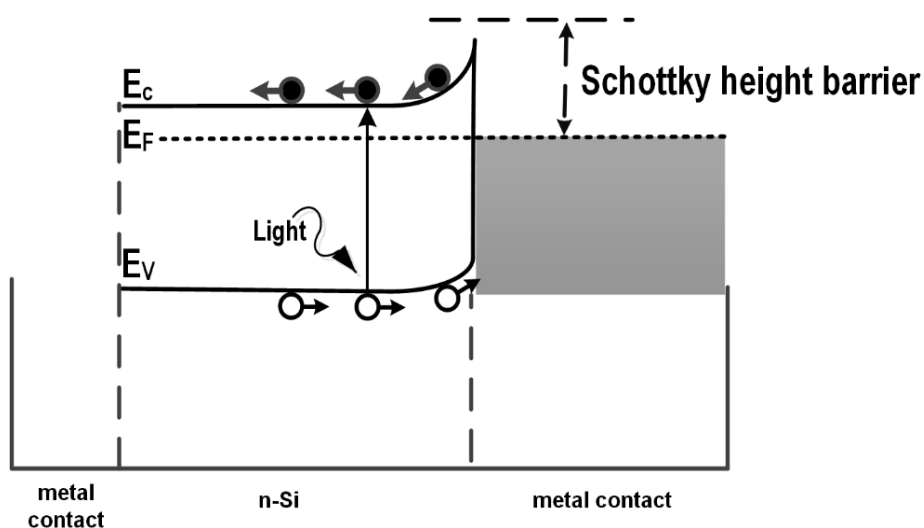


Figure 2-19: Schematic energy diagram of a Schottky junction solar cell, indicating the photo-excited electron transfer.

To reduce the optical loss, indium-tin-oxide (ITO) film is used instead of the metal layer in the Schottky junction solar cell [2, 3]. Nevertheless, the limited resource of indium causes a high production cost of solar cells. The diffusion of indium ions also results in a degradation in the device performance. Additionally, the brittle nature of ITO limits its application in flexible solar cells [4, 5]. Recently, CVD-graphene, which has outstanding physical properties which are described later, is used to prepare flexible Schottky junction solar cells. Since graphene has a near-zero band-gap, the optical loss is also eliminated in graphene/Si Schottky junction solar cells [5]. Hence, usage of graphene is a feasible way to prepare low-cost, flexible and high-performance solar cells.

3 Graphene, its properties and application in Schottky junction solar cells

3.1 Characteristics of graphene

3.1.1 Physical characteristics of graphene

Graphene consists of a monolayer of carbon atoms forming a two-dimensional honeycomb lattice as shown in Fig. 3.1. Since this material is a sheet of carbon atoms one atom thick, it is the thinnest film ever formed [6, 54]. The structure of graphene can be represented as a triangular lattice with two atoms (A and B) per unit cell. Where a_1 and a_2 are the lattice unit vectors, and δ_i ($i=1, 2, 3$) is the nearest-neighbor vector. The reciprocal-lattice vectors are b_1 and b_2 . Each atom will form 4 bonds; 3 σ bonds and one π bond in the third dimension [55]. Fig. 3.2 shows a typical Raman spectrum of a monolayer graphene, consisting of three major peaks: D, G, and 2D. As shown, the D peak is the first peak, and it refers to defects participating in double resonance Raman scattering near the K point of the Brillouin zone [56, 57]. The position and shape of this peak depend upon the frequency of the laser and the defects in graphene. This peak is usually weak in the graphene spectrum and is at about 1350 cm^{-1} [58]. The D peak actually arises from the double resonant (DR) Raman process in the Brillouin zone as shown in Fig. 3.3a. This process happens when an electron-hole pair is created by a photon at K point in the first Brillouin zone (FBZ). After that, an electron will scatter by absorbing a phonon into the second conduction band at K' point in the second Brillouin zone. This electron must scatter back to K before recombining with a hole to conserve energy and momentum. Thus, the electron will elastically scatter back to the first conduction band by a defect [59-61]. Defects in graphene are owing to PMMA residue or any breaking of the symmetry of the graphene lattice, such as a vacancy site [62, 63], sp^3 -defects [64], grain

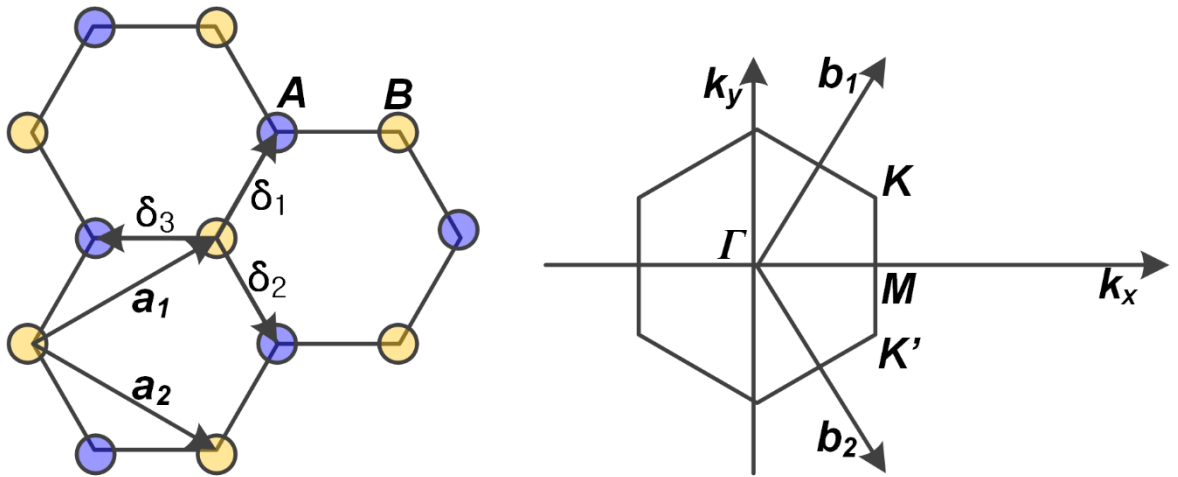


Figure 3-1: Sketch of graphene geometry in real and reciprocal space. Left: Hexagonal honeycomb lattice in real space, the vectors a_1 and a_2 and the atoms A and B define the Bravais lattice; Right: Corresponding Brillouin zone where Γ is the centre of the FBZ and K and K' are its corners; M is located on a side of the FBZ between K and K' point.

boundaries [65], or even an edge [66-68]. Finally, the electron will recombine with a hole, resulting in an emission of a photon. It is clear that the Raman process in the case of D peak requires a phonon, so the energy shift for the D band is half than that of the 2D band [64]. The second peak is the G peak, and it is a doubly-degenerate in-plane sp^2 (C-C) stretching mode [69]. For all sp^2 carbon systems, including amorphous carbon, carbon nanotubes and graphite, this peak exists [70]. The position of this peak is quite sensitive to the doping level in graphene, and it has been stated that G peak appears in the frequency range from 1518 cm^{-1} to 1630 cm^{-1} [71, 72]. It also shifts to lower energies with increasing number of graphene layers [72, 73]. This indicates that detail about the number of graphene layers is obtained from the G peak. This peak arises from a single resonant process that starts with an incident photon that resonantly excites a virtual electron-hole pair in graphene as shown in Fig. 3.3b. Then, the electron and hole recombine, leading to an emission of a photon which is red shifted by the amount of energy given to the phonon [74]. The 2D peak, which is the last peak, is the strongest peak of the graphene spectrum. The 2D peak shifts to lower energy by

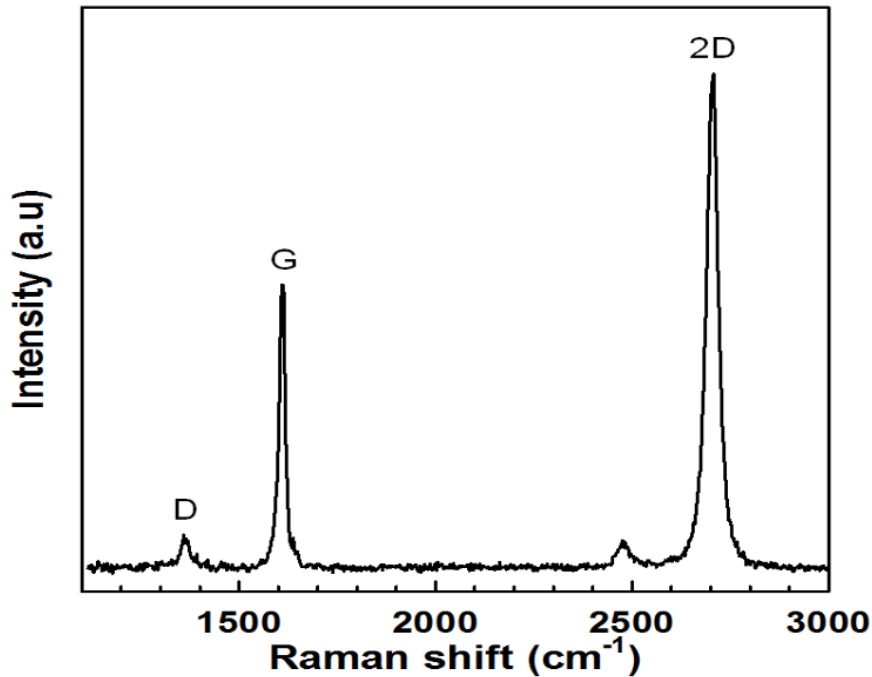


Figure 3-2: Raman spectrum of transferred CVD-graphene on SiO₂/Si substrate.

decreasing the number of graphene layers. Additionally, the position of it depends on the graphene doping level. The position of this peak is around 2700 cm⁻¹. Fig. 3.3c shows the origin of this peak. It can be seen that an electron-hole pair is created by a photon at the K point in the first Brillouin zone. After that, the electron at K will scatter by absorbing a phonon into the second conduction band at K'. Due to the conservation of energy, this electron must scatter back to K before recombining with a hole. Thus, the electron will elastically scatter back to the first conduction band by absorbing the second phonon. This means that the mechanism of this process requires two phonons. Then, the electron will recombine with a hole in the valence band, resulting in an emission of a photon. The 2D process is also known as double resonant, as the incident or scattered photon and the first or second phonon scattering are resonant with electronic levels in the graphene [58]. Conversely, the 2D band process can also be triple resonant as shown in Fig. 3.3c. In this case, the electron at valence band in the

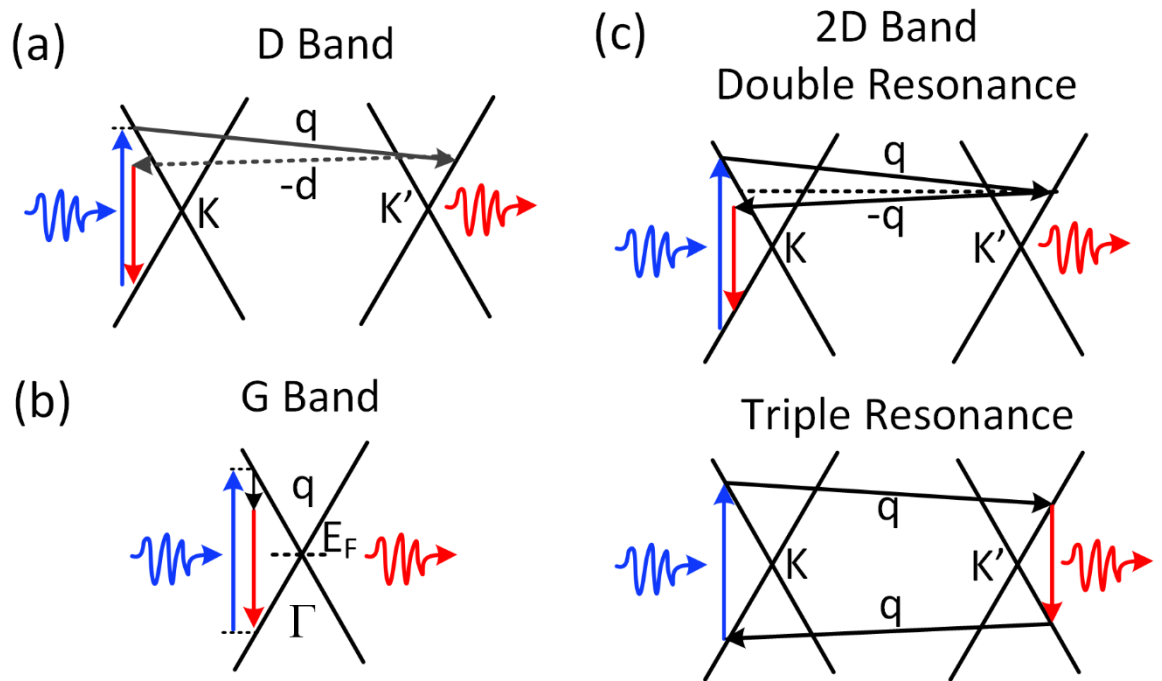


Figure 3-3: Sketch of the main Raman processes in graphene. (a) D band double resonant process involving a scattering from a defect. (b) and (c) G and 2D peaks generated through a second-order process, respectively.

second Brillouin zone will scatter elastically by absorbing an additional phonon and then recombining with a hole at the valence band in the first Brillouin [58, 75]. The quality and monolayer nature of graphene is provided by the intensity ratio of the 2D to G (I_{2D}/I_G) peaks. For example, when this ratio is around 2 for monolayer graphene, graphene is high-quality monolayer [76]. Graphene also has unique and interesting optical properties, and each graphene layer can transmit around 97.7% of the incident light as graphene has a zero band gap energy [77]. This means that a graphene sheet will not cause optical losses. Therefore, the usage of graphene in solar cells will increase the short current circuit, resulting in an improvement in solar cell performance.

3.1.2 Electronic properties of graphene

A zero band gap is a unique property of graphene as the conduction and valence bands are located at the same position as demonstrated in Fig. 3.4. Carbon atoms have 6 electrons. 2 electrons in the inner shell and 4 electrons in the outer

shell. The 4 outer shell electrons in an individual carbon atom are available for chemical bonding. In a graphene sheet, each atom is connected to 3 other carbon atoms as 3 σ bonds in the two-dimensional plane. The fourth electron of carbon atom is free in the third dimension. The fourth electrons are known as π electrons or Dirac fermions and are located above and below the graphene sheet [78, 79]. This means that the fourth electrons of the carbon atoms will behave as massless at the Dirac points. In other words, the dispersion relation between energy and momentum is linear which is in contrast to a band-gap semiconductor where the dispersion is quadratic [80]. Therefore, π electrons are responsible for the remarkable electronic properties of graphene. The electrical properties of graphene such as a contact resistance (R_C), sheet resistance, mobility (μ) and Dirac point are studied using a graphene-based back-gated field effect transistor (gFET) as shown in Fig. 3.5. The mobility and Dirac point are obtained from the current-voltage (I_D - V_G) transfer curve of the gFET as shown in Fig. 3.6a.

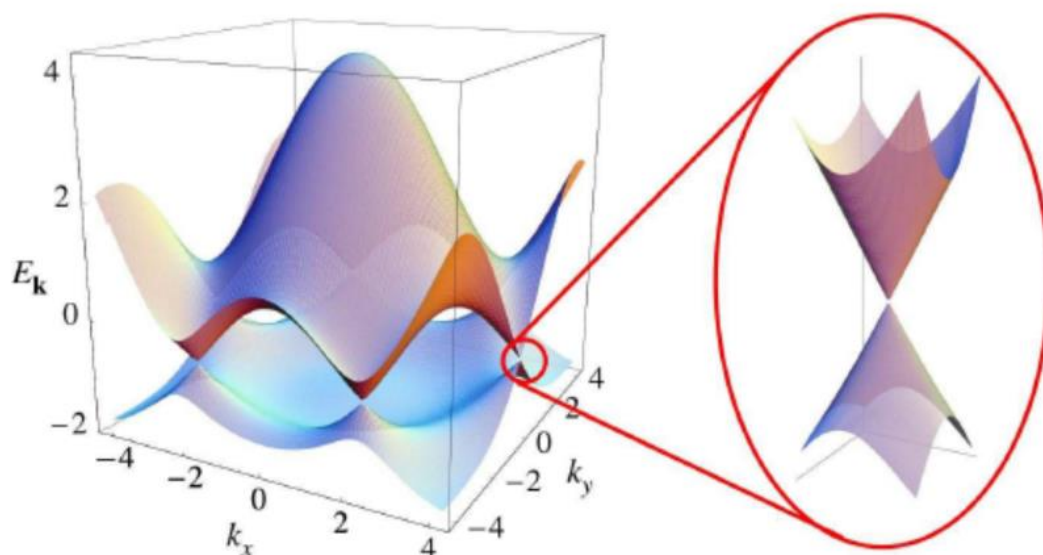


Figure 3-4: Electronic dispersion in the honeycomb lattice. Left: energy spectrum (in units of t). Right: zoom in of the energy bands close to one of the Dirac points [74].

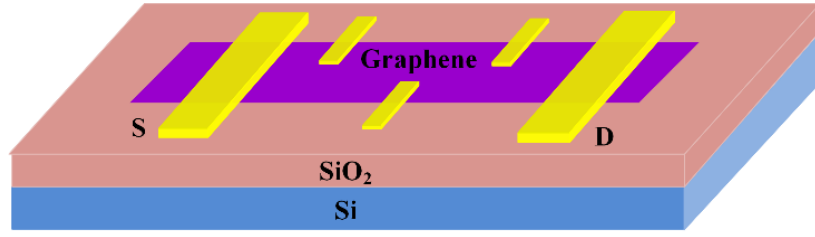


Figure 3-5: Structural diagram of a conventional graphene-based back-gated FET.

This curve is obtained from plotting the current measured between the source and drain electrodes versus the voltage applied across the source and gate electrodes. A typical graphene FET exhibits ambipolar behaviour in the I_D - V_G curve owing to the zero bandgap nature of monolayer graphene. In this case, the mechanism of carrier transport changes from electrons to holes (or from holes to electrons) when carriers reach a minimum level at the Dirac Point as shown in Fig. 3.6a. Both holes and electrons have their contribution to charge carriers at the region of the Dirac Point, whereas carriers consist of only holes or electrons in the regions relatively far from the Dirac Point. The field-effect mobility (μ) of holes and electrons can be extracted in this figure from the slope of source-drain current variation from gate voltage to the linear regime using the following equation [81]:

$$\mu = \frac{L}{WC_{ox}V_D} \frac{\Delta I_D}{\Delta V_G} \quad (2.27)$$

Where, L and W are the channel length and width, C_{ox} is the gate capacitance (11.5 nf cm^{-2}), V_D is the source-drain voltage and $\Delta I_D/\Delta V_G$ is the transconductance. The contact and sheet resistances are extracted from a current-voltage (I_D - V_D) output curve (see Fig. 3.6b) of the gFET using a four-probe/two-probe method. In this case, contact resistance for each contact is obtained as follows [82-85]:

$$R_C = \frac{1}{2} (R_{total} - R_g) \quad (2.28)$$

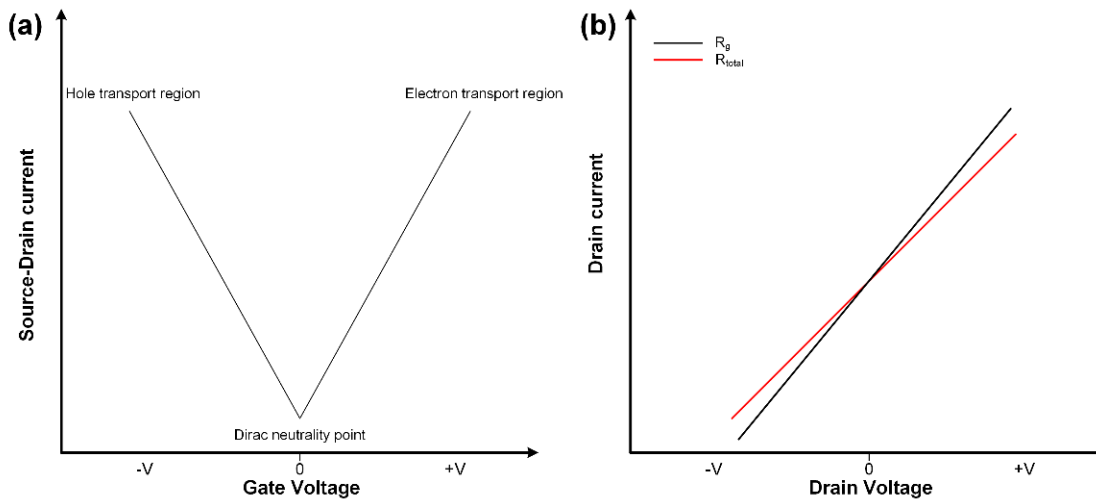


Figure 3-6: (a) and (b) Ideal (I_D - V_G) transfer and (I_D - V_G) output curves of the gFET, respectively.

Where R_c is the contact resistance between graphene and metal, R_{total} is the total resistance measured between the source and drain and R_g is the graphene channel resistance. In fact, the contact resistance arises at the metal/graphene interface represents the major limitation to the complete exploitation of graphene properties in electronic devices. In order to obtain efficient graphene-based devices, the contact resistance should be minimized [82-85].

3.2 Growth of large area sheets of graphene by Chemical Vapour Deposition

In 2004, researchers at the University of Manchester produced monolayer graphene on SiO_2/Si substrates by the scotch-tape method [6]. Although they prepared high-quality graphene sheets, the area of these sheets is very small. After that, teams tried to fabricate large sheets of graphene using different techniques such as reduction of graphene oxide, liquid phase exfoliation, epitaxial growth on SiC substrate and graphene growth from solid carbon sources. However, the quality of the graphene sheet thus produced is not good enough to use in electronic applications [86-88]. Li and his co-workers formed a large area

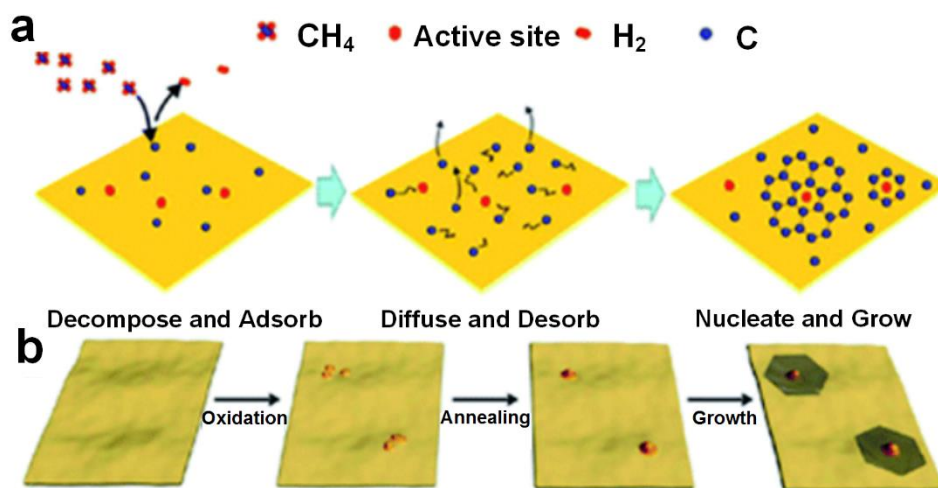


Figure 3-7: Schematic illustration of the growth mechanisms of the CVD growth process of graphene films. (a) CVD growth process with a methane precursor. (b) Scheme of the mild oxidation and sequential reductive heat treatment before the CVD process [80].

of graphene sheets with high quality by Chemical Vapour Deposition (CVD) [87].

The growth mechanism of graphene sheets by this technique is a result of the catalytic effect of metals [89, 90]. For metals with a relatively higher carbon solubility at high temperatures (such as nickel), the carbon atoms are dissolved in the metal to form solid solutions within the metal. Then, carbon atoms are segregated from the solid solution upon cooling due to the reduction of carbon solubility as temperature reduces, and precipitated on the metal surface to form graphene crystals. For copper which has a lower carbon solubility than nickel, carbon atoms are directly deposited on the catalytic surface (Cu) without segregation resulting in a graphene layer [86-88]. During this process, the metal surface is generally pre-annealed (800-1000 °C) in vacuum to obtain larger crystalline grains as shown in Fig 3.7. Then, short chain hydrocarbon molecules are introduced into the furnace chamber, where they are adsorbed on the metal surface, decompose into carbon atoms and form graphene on the metal surface [91, 92]. There are many factors effecting the CVD process such as concentration

and gas flow rate [93], annealing process [94], metal grain size [95, 96] and cooling rate [97].

3.3 Wet transfer process

A wet transfer process is used to transfer CVD-graphene sheets from metals to substrates. In this process, the graphene sheet/ metal is spin-coated by a Poly (methyl methacrylate) (PMMA) $(C_5O_2H_8)_n$ film as shown in Fig. 3.8 and then floated in an etchant solvent to etch the Cu substrate. In the fabrication process of graphene/silicon Schottky junction solar cells, etching solvents such as ferric chloride and ferric nitrate are usually used [45, 98-101]. These solvents leave chemical residue on graphene layers. This effects the electrical properties of transferred graphene, resulting in a recombination process of charge carriers and a decrease in the graphene/Si Schottky junction performance [102, 103]. In contrast, ammonium persulfate is rarely used for that purpose although this solvent leaves a chemical free residue [102]. Once the removal of the metal layer is completed, the floating PMMA/graphene layers are transferred to the desired substrates. Then, the PMMA layer is removed with acetone treatment [57]. However, after removing the PMMA layer by the standard acetone treatment process, there is a residue of PMMA because acetone can not remove this layer completely. The PMMA residue is actually the main issue of the wet transfer process because it has a negative effect on the graphene properties such as the shifting of the Dirac point, increased sheet and contact resistance, and reduction of the mean free path [104]. Moreover, it alters the electronic band structure of graphene when it is adsorbed at the edge or at defect sites [105-107]. It has also been stated that the hysteresis in (I_D-V_G) characteristics of gFETs is originated as a result of trapping charges at a graphene/SiO₂ interface [108-110]. The density

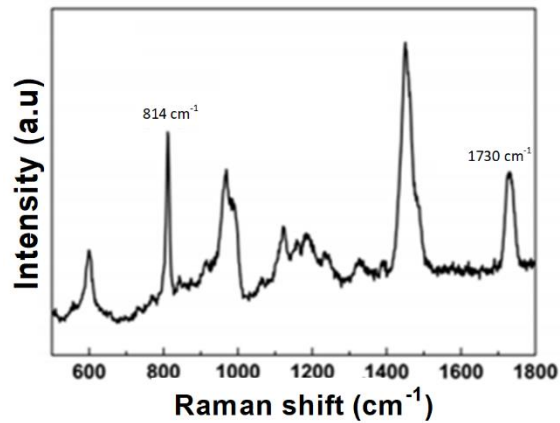


Figure 3-8: Typical Raman spectrum of PMMA layer [111].

and occupancy properties of these charges generally depend on the composition and fabrication process of the dielectric materials [112]. In fact, PMMA residue is also one of the major issues that affects CVD-graphene surface [113-117]. This indicates that the density of trapped charges at the graphene/SiO₂ interface will be increased, leading to a further increase in the hysteresis in I_D - V_G characteristics of this kind of devices. Hence, minimizing the PMMA residue on a graphene surface may reduce the hysteresis in I_D - V_G curves. Removing the residue of PMMA is a challenging issue for obtaining a graphene sheet with its intrinsic electronic properties [118]. Several techniques have been utilized to remove this residue such as a modified Radio Corporation of America Cleaning (RCA) process and an atomic force microscope (AFM) to mechanically sweeping away the contamination [119]. However, these techniques require complicated wet chemistry and are limited to cleaning only a local area [119-121]. Her and his co-workers have used acetic acid to remove the residue of PMMA [121]. However, this technique is useful to remove the PMMA residue from a small area of graphene sheets. Sack and his co-workers also minimize the PMMA issue by the formamide liquid (CH₃NO). Graphene samples, in this case, are immersed in the formamide liquid overnight [122]. However, this method required long time to reduce PMMA residue. To date, annealing transferred graphene in Ar/H₂ forming

gas for few hours is an usable method to reduce the PMMA residue on the large area of graphene sheet although this method cannot entirely remove the PMMA residue, where the mechanism of this process is burning some PMMA residue on graphene surface. It was also shown that there is a blue shift in the spectrum of annealed graphene because of the p-doping effect [103, 107, 123, 124]. This means that the annealing process enhances p doping in graphene.

3.4 Application of CVD-graphene in Schottky junction solar cells

The attractive properties of graphene, such as near-zero band-gap, high electrical conductivity, high mobility, flexibility, and high transparency have stimulated a lot of research interest [7]. One promising application for graphene is in graphene/silicon Schottky junction solar cells. To fabricate this device, there are two structures reported so far, which are top-window and top-grid [125].

3.4.1 Graphene/Si Schottky junction solar cells with a top-window structure

Graphene/Si Schottky junction solar cells with a top-window structure are widely reported. In this structure, an n-Si substrate coated with a 300nm SiO₂ layer is used in the fabrication process as shown in Fig. 3.9. A layer of Au is formed on a SiO₂ layer. Usage of an Au layer is to provide a low contact resistance to graphene layers [45, 100, 126]. Consequently, a patterned square window on the SiO₂/Si substrate is etched using photolithography and subsequent wet-etching. Then, the ohmic contact will be formed. Afterwards, PMMA/CVD-graphene layers are transferred onto the substrate by the wet transfer process to form a Schottky junction with Si.

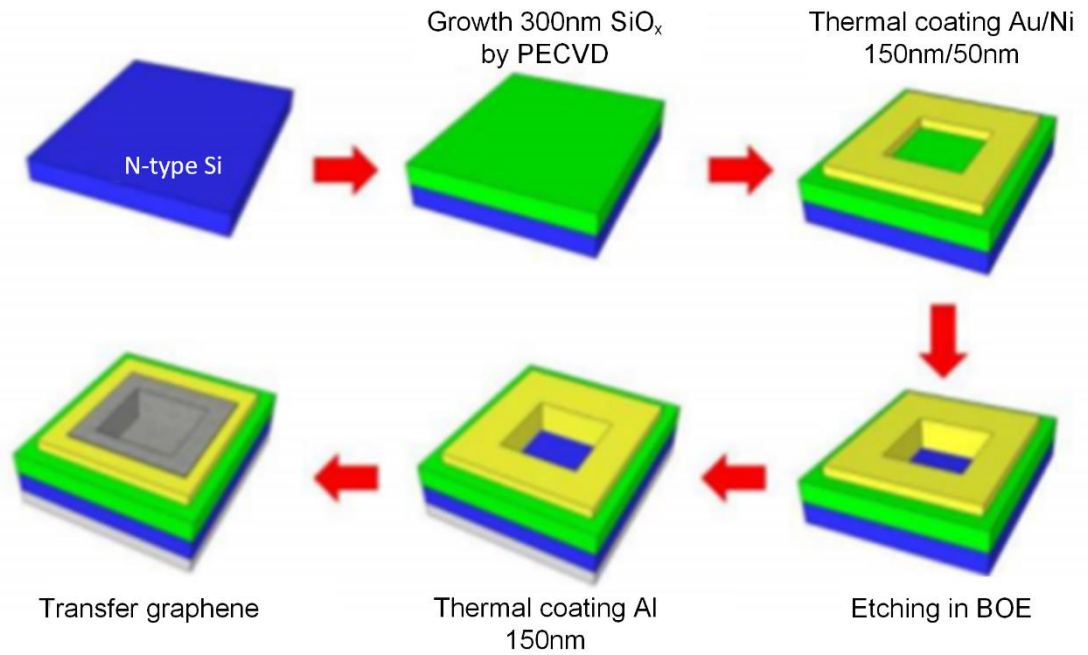


Figure 3-9: The Fabrication process of a graphene/n-Si Schottky junction based on a top-window structure [46].

It has been shown that the optimum area of graphene sheet, which forms a Schottky junction with a Si substrate, is 0.11 cm^2 . The reason for using such a small graphene area is the quality of Schottky junction degrades when a graphene area larger than 0.11 cm^2 is used [125, 127]. Additionally, the optical loss of the front contact, which is formed on the graphene surface, is increased when a large graphene area is employed within the fabrication process [125].

These reasons result in a poor solar cell efficiency. In reported graphene/Si Schottky junction solar cells [45, 98-101], acetone is only used to remove the PMMA layer from the graphene surface [45, 98-101]. This means that there is PMMA residue on graphene sheets as mentioned in section 3.3. This residue causes the recombination process of charge carriers, leading to a decrease in the solar cell efficiency, and this will be shown in chapters 5 and 6. In 2010, Li and his co-workers have fabricated the first graphene/Si Schottky junction solar cell with an active area of about 0.1 cm^2 and efficiency of about 1.34%. It was reported

that the low efficiency and open circuit voltage of the fabricated device is due to the low Schottky barrier between the graphene layer and metal [38]. This indicates that the difference between the work functions of graphene and Si is not suitable to form a proper Schottky junction [1]. To improve the solar cell performance, multi-graphene layers (MGL) have been used to fabricate MGL/Si Schottky solar cell. This improved the efficiency of this cell to 2.1%. This improvement was attributed to an enhancement in the transport of carriers and a decrease in the series resistance of the device. Furthermore, the sheet resistance of graphene reduced from $3000 \Omega \square^{-1}$ for monolayer to $750 \Omega \square^{-1}$ for three layers. [45]. To enhance the work function of the graphene sheet, Miao and his co-workers have employed chemical doping. This leads to an increase in the Schottky barrier height ($\Phi_B = W_{Gr} - \chi_{Si}$) and the built-in potential ($qV_{bi} = W_{Gr} - W_{Si}$). Therefore, the V_{OC} of the solar cell increased and sheet resistance reduced. This improved the efficiency of doped-graphene/Si solar cells to 8.6% [100]. Although chemical doping improved the solar cell performance, the efficiency of solar cells suffers from a decline with time. This indicates that chemical doping is not a suitable method to achieve stable graphene/n-Si Schottky junction solar cells. Instead of chemical doping process in graphene, an external power supply and polarizing a ferroelectric polymer layer were integrated to achieve stable doped-graphene/Si solar cells. In this case, a 2 nm GO layer was deposited on the silicon substrate to optimize the graphene/Si interface as shown in Fig. 3.10. Then, a monolayer graphene layer was transferred onto the Si substrate. Subsequently, thermal evaporation was used for the front contact. After that, an insulating layer of 10 nm HfO_2 was coated on the graphene layer. Afterwards, the second graphene sheet was transferred to the last insulating layer, followed by forming a poly (vinylidene fluoride-co-trifluoroethylene) P (VDF-TrFE) layer. Finally, Ag and

InGa layers were formed for a cathode and gate, respectively as shown in Fig. 3.10. This improved the solar cell efficiency to 4.14% [128]. However, it can be noticed that the fabrication process of this device is more complicated and higher cost than that of pervious devices. Other teams stated that the dangling bonds at

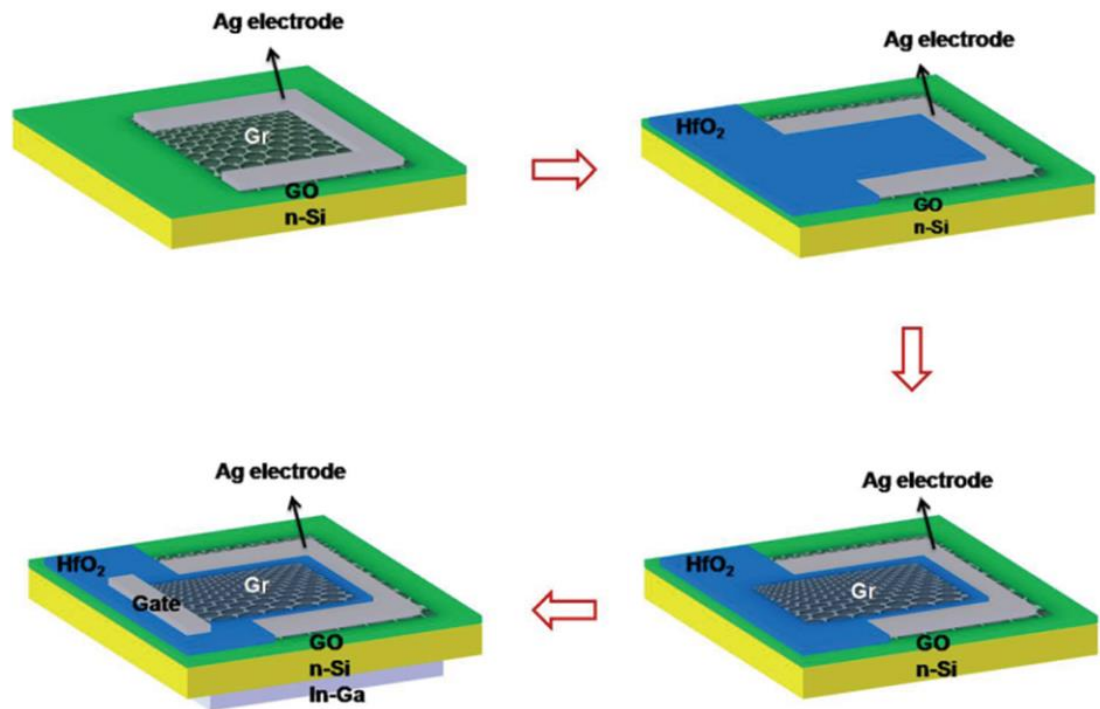


Figure 3-10: Fabrication process of the external electric field doped graphene/Si Schottky solar cell [112].

a Si surface also results in a low value in an open circuit voltage of graphene/Si Schottky junction solar cells since dangling bonds causes the recombination process of charge carriers at the graphene/Si interface [38]. To minimize the recombination process, a layer of graphene oxide (GO) has been formed as an intermediate layer between the graphene and Si substrate [129]. The inserted GO layer functions as a hole transport layer to improve the separation of electron-hole pairs. This also suppresses recombination at the graphene/silicon interface. Thus, the passivation process led to a significant increase in the solar cell efficiency to about 6%. However, creating the GO layer results in additional

complexity in the fabrication process of graphene/Si Schottky junction solar cells. To obtain an easier and lower cost passivation process, it has been stated that exposing Si substrates to ambient air for 2 hours forms an effective layer of native SiO₂ [45, 127, 130]. In contrast, it has been shown that the native oxide grown on Si substrates in this case causes a serious recombination process of charge carriers [127]. The additional issue of this cell is the reflectivity of the silicon substrates which is around 40%, and this causes optical loss. In order to reduce the reflectivity, the texturing process of Si substrates was applied in the fabrication process of graphene/n-Si Schottky junction solar cells. Unfortunately, this process causes a severe recombination process of charge carriers at the graphene/textured Si interface, resulting in a decrease in the solar cell efficiency [131, 132]. A TiO₂ layer as an antireflection layer was used instead of the texturing process to reduce the reflectivity of the silicon substrates. Usage of a 65 nm TiO₂ layer reduces the reflection from 38% to 30% at 550nm, leading to an increase in the short circuit current of this cell [133]. However, reducing the reflectivity to 30% is still not good enough to obtain high graphene/Si solar cell efficiency. In several reported devices [38, 127, 132-137], there was also a distinctive s-shaped kink in the measured *J-V* curves. In fact, the s-shaped kink affects the performance of graphene/Si Schottky solar cells by reducing the fill factor [38, 133-140]. It has been reported that there are many reasons for the s-shaped kink effect. For example, it was suggested that the s-shape is due to the limitation of accessible states for the holes in graphene [136, 140]. It was also stated that this effect is attributed to carrier recombination losses at the graphene/Si interface due to dangling bonds at Si surfaces, and this reduced by using a thin layer of SiO₂ [127] or GO [129] as a passivation layer for the silicon surface. In several cases, the s-shape could also be eliminated when the graphene doping level is enhanced

using doping process such as chemical, electrostatic gating or forming gas [103, 133, 135, 136, 140], but after sometime the s-shape would be observed again in the J - V curves [141]. This indicates that the reason for the existence and subsequent removal of the s-shape kink in the J - V curve is still unclear.

Other teams tried to prepare this cell using a p-type silicon rather than an n-type silicon as substrates. Fabricated devices showed the very low efficiency of 0.1%, and it was mentioned that the main reason of the low graphene/p-Si efficiency is the difficulty of forming an effective n-graphene transparent cathode with a suitable doping level and an appropriate interface with a p-Si substrate [142]. Recently, Ho and his co-workers used graphene/TiO_x as a transparent cathode to prepare a graphene/p-Si Schottky junction solar cell. The efficiency of this cell increased from 0.1% to 2.2% after removing the native oxide from Si substrates by post buffer oxide etchant (BOE) [127].

3.4.2 Graphene/Si Schottky junction solar cells with a top-grid structure

Recently, graphene/Si Schottky solar cells based on a top-grid structure as shown in Fig. 3.11 have been reported as having a larger active area, lower cost and an easier fabrication process [125], in comparison with devices fabricated with the top-window structure. With this structure, ultraviolet (UV) photolithography and etching process of SiO₂ layers is avoided by forming the top-grid on graphene sheets directly. The highest efficiency of 4.29% was achieved for the 0.1 cm² device area. However, the performance of prepared

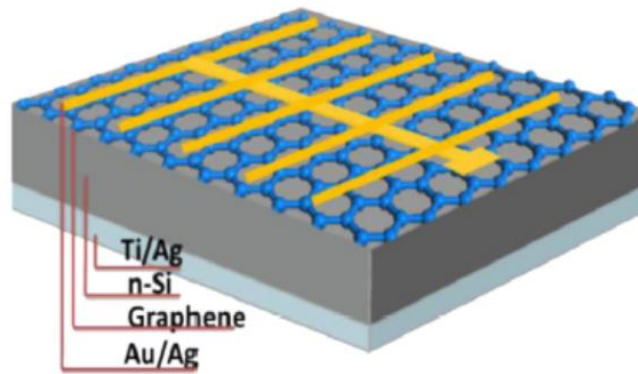


Figure 3-11: Schematic structure of a graphene/Si Schottky junction solar cell based on the top-grid structure [105].

devices with a graphene area larger than 0.11 cm^2 was degraded to 0.6%. This means that the optimum area of the graphene sheet as a Schottky junction with Si is around 0.11 cm^2 in order to obtain efficient solar cells [125, 127]. This also points out that transferred graphene layers on Si substrates should be patterned when graphene/Si Schottky solar cells based on the top-grid structure are fabricated. Thus, to obtain the optimum area of the graphene sheet, reactive-ion etching (RIE) is often used. However, some reports have shown that RIE causes degradation of the mobility of patterned graphene due to the variation in growth direction along the crystal lattice of the catalytic metal substances as well as the inherent crystal grain boundaries present in the CVD grown graphene [143]. Oxygen plasma etching has also been used to pattern graphene nanostructures [144, 145]. However, this technique affects the field effect conductivity, surface morphology and other properties of graphene [146-149]. In addition, the etching rate for this technique is too fast, and it is impossible to control the etching process [150]. Furthermore, oxygen plasma requires special vacuum pumps and safety precautions. In contrast, argon plasma etching has not been reported very much in the shaping process of graphene due to the difficulties in the removal of the thermal cross-linked sacrificial layer after the etching process [151-154].

Additionally, a metal-graphene contact resistance is a crucial factor that affects the performance of graphene/Si Schottky junction solar cells with the top-window structure. To provide a low contact resistance to graphene layers, an Au electrode is formed by a thermal evaporation method, which is a non-destructive technique for graphene layers [155]. However, this method is costly for commercial production. In contrast, a sputtering method, which is the most favourable technique in the current semiconductor industry, is rarely used to create Au electrodes in the fabrication process of graphene-based devices. The sputtering method has many advantages such as high throughput, diverse material choices and low cost. It has been reported that defects and disorders are introduced into graphene sheets due to the energetic sputtering flux [156-159], resulting in a high contact resistance of around 4.2 K Ω extracted by four-probe/two-probe method [85]. This indicates that the sputtering process of Au should be achieved at a low deposition rate to maintain the properties of graphene. The sputtering method also causes very difficult to remove an unwanted sputtered films compared to that of evaporated [160, 161]. This also indicates that a sputtering rate of Au atoms will be less than those in the case of Ag and Cr atoms [161, 162]. Thus, the photolithography and lift-off processes should be modified to engage the sputtering process for Au in the fabrication process of graphene-based devices.

In conclusion, there are two structures to fabricate graphene/Si Schottky junction solar cells. The fabrication process of devices with the top-grid structure is easier and lower cost compared with that of devices with the top-window structure. However, the efficiency of devices based on the top-grid structure is less than that of devices based on the top-window structure. For devices fabricated with both structures, there are some serious disadvantages such as a small active area of about 0.1 cm², high cost and a complex fabrication process. Graphene/Si

Schottky junction solar cells also suffer from the recombination process owing to the chemical residue obtained from ferric chloride and ferric nitrate solvents, PMMA residue, dangling bonds at a Si surface and texturing process, leading to a decrease in the solar cell performance. In several reported devices, there is a distinctive s-shaped kink in the measured J - V curves, and the reason of this shape is still not clear!

4 Characterisation and experimental techniques

4.1 Characterisation techniques

4.1.1 Optical Microscope

An optical microscope is shown in Fig. 4.1, and it is used to analyse the uniformity and continuity of CVD-graphene layers transferred onto SiO₂/Si substrates. This microscope has four objective lenses (5 X, 10 X, 20 X and 50 X) and two-eyepieces (10 X), and it is connected to a high-resolution monitor. The intensity of the white light source can be controlled. Fig. 4.2a shows how the light source interacts with the three interfaces at graphene, SiO₂ and Si layers. Since a part of the incident light is reflected from each interface and the rest of that light is transmitted and refracted. Therefore, a number of optical paths are possible. The amplitude of the reflected light, which makes the visibility of graphene layers on SiO₂/Si substrates, is as a result of interference between all the optical paths.

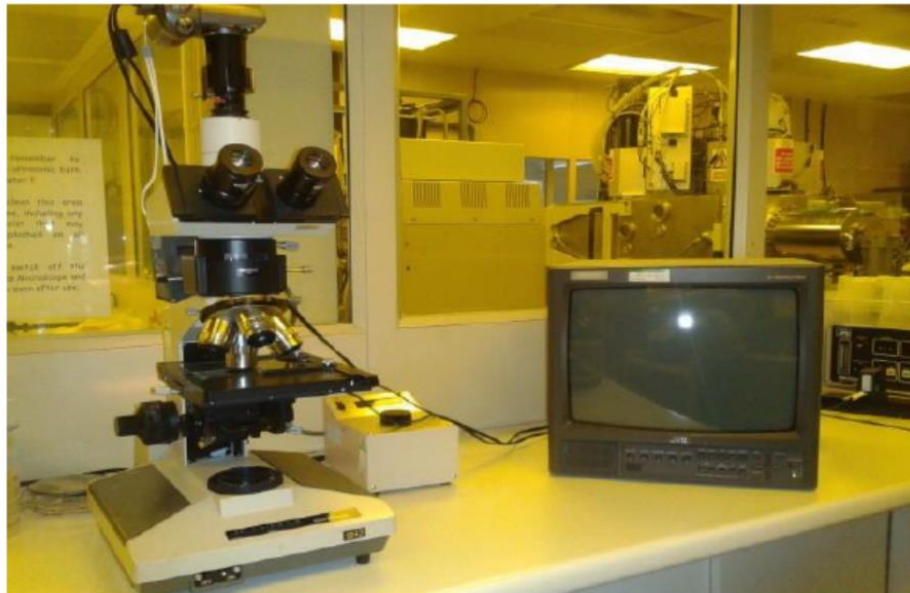


Figure 4-1: Optical Microscope (BH2 Olympus).

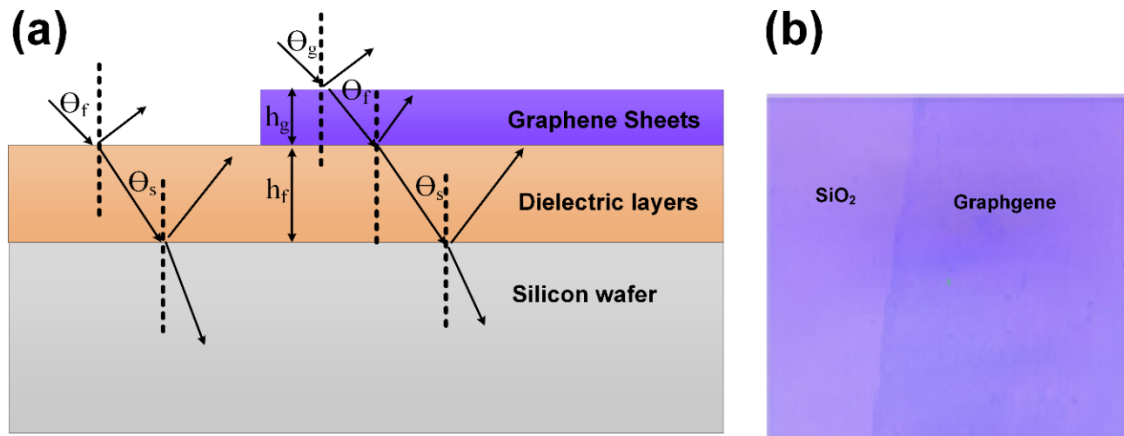


Figure 4-2: (a) Schematic of reflected and transmitted light from graphene/SiO₂/Si substrate. (b) Optical image of CVD-graphene transferred onto a SiO₂/Si substrate.

It has been reported that the optical image of graphene can be different from lab to another lab due to the combination of the reflection spectrum [163]. Fig. 4.2b shows a typical optical image of a monolayer graphene sheet, and it can be noticed that there is a clear difference between the colours of graphene and SiO₂.

4.1.2 Atomic Force Microscopy (AFM)

The morphology of graphene layers is investigated by Atomic Force Microscopy (AFM). Furthermore, this technique is used to measure the thickness of coated films. Fig. 4.3a shows the optical picture of the system, which involves an electronic controller, a mechanical measurement unit and a PC with corresponding software. Fig. 4.3b displays a typical block diagram of AFM which consists of a cantilever with a sharp tip (probe) at its end that is used to scan a specimen surface. The cantilever is typically made of silicon or silicon nitride with a tip radius of curvature on the order of 10 nm. When the tip is brought into proximity of a sample surface, the force between the tip and sample leads to a deflection of the cantilever according to Hooke's law which is expressed as:

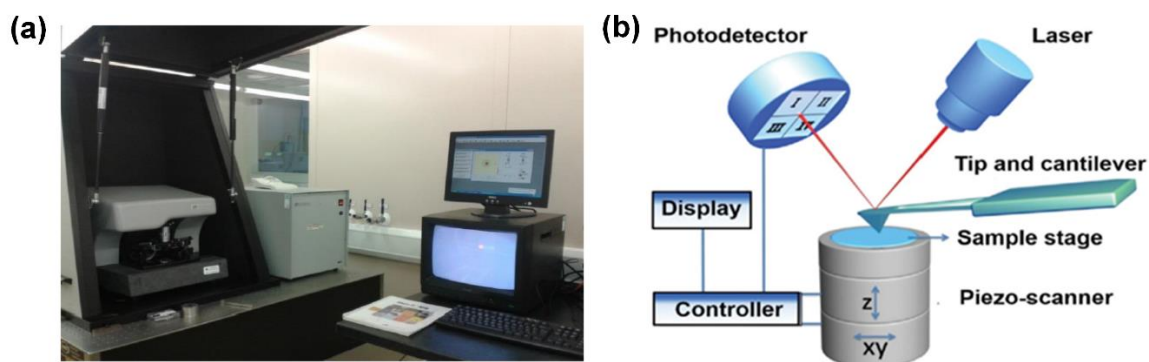


Figure 4-3: (a) Optical image of AFM system (PACIFIC NANOTECHNOLOGY). (b) Block diagram of AFM [148].

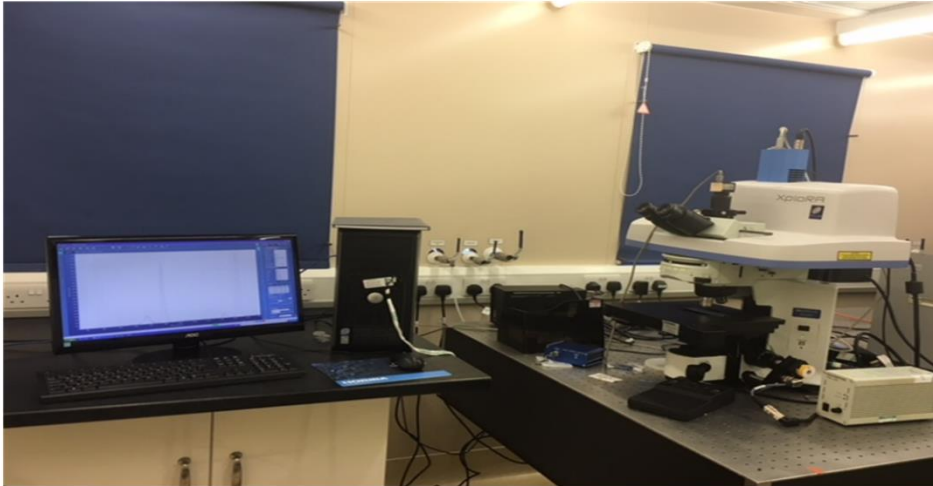
$$F = -kx \quad (4.1)$$

Where k is the spring constant of the cantilever and x is the distance between the tip and the sample surface [164]. In this process, a laser beam deflects from the cantilever to a photodiode. The photodiode measures the deflection of the cantilever and is converted it into an electrical signal. The magnitude of this signal is proportional to the displacement of the cantilever with respect to the equilibrium position of a sample. These electrical signals are then converted into 2D and 3D images of the sample surface.

4.1.3 Raman spectroscopy

Raman spectroscopy is a unique tool to analyse the crystallinity, doping and impurity content of graphene sheets through positions and ratios of graphene peaks (see section 3.1.1). In this case, an XPLORA HORIBA system combines with an Olympus BX41 microscope (equipped with 10 X, 100 X objective lenses and 10 X eyepieces) as shown in Fig. 4.4a. The characterisation of graphene is achieved under typical acquisition parameters, which are 532 nm green laser source with the power of 100 mW, 100 X objective lens, a scan range of 1100 to 3000 cm^{-1} and an exposure time of 5-60 s. Raman spectroscopy is based on the

(a)



(b)

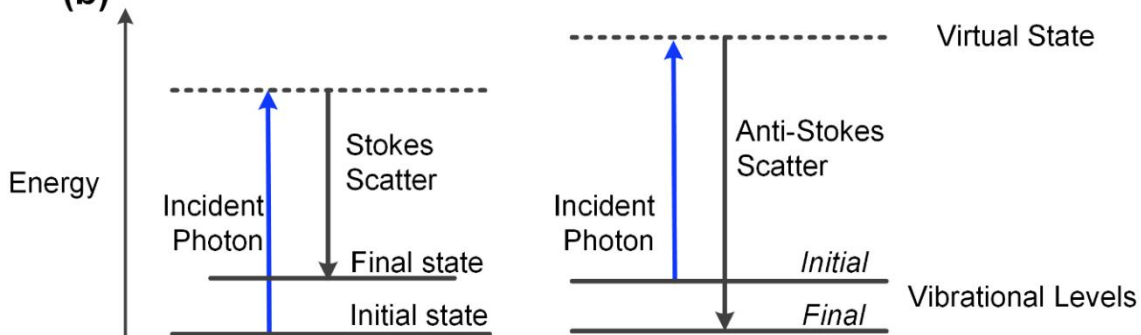


Figure 4-4: (a) Optical image of XPLORA Raman system with an Olympus BX41 microscope in Cleanroom. (b) Schematic of Raman scattering process, showing Stokes and Anti -Stokes Scatters.

inelastic scattering of monochromatic light as shown in Fig. 4.4b. Inelastic scattering means that the frequency of the photon will change when it interacts with the molecules in graphene crystal. When molecules absorb an incident photon with frequency (ν_0) at the ground state, it will excite into a virtual state (ν_m). There are two types of the scattering processes. If the excited molecule decays back to a higher level than the initial, this is called Stokes Scattering. Anti -Stokes Scattering is obtained if the exciting molecule decays back to a lower level than initial. According to the changes of the wavelengths or wave numbers of scattered light, which is caused by the molecular rotation and vibration, information about molecular structure and defect density is obtained [165].

4.1.4 X-Ray Photoelectron Spectroscopy (XPS)

PMMA residue left on a CVD-graphene surface is investigated by XPS since this technique is one of the best techniques to study the elemental composition and chemical state of the graphene surface. XPS analysis is carried out at Newcastle University using a Kratos AXIS Ultra DLD spectrometer, monochromatic Al $K\alpha$ emission at 1486.6 eV with an operating power of 150W. The measurement is carried out in the fixed analyser transmission (FAT) mode with a pass energy of 80 eV and 20 eV for wide survey scans and high-resolution scans respectively. XPS peaks are obtained by irradiating a sample with X-rays, leading to the emission of electrons from the first few nanometres of the material, where each electron emission has a unique binding energy. By analysing the binding energy and their corresponding spectra, elemental data can be obtained.

4.1.5 Nkd-7000 spectrophotometer

An nkd spectrophotometer is used to characterise the reflectance of silicon substrates before and after applying anti-reflective coatings and texturing processes. Fig. 4.5 shows the optical picture of the spectrophotometer. This equipment consists of a light source with a wavelength range from 350 to 1100 nm, a slit, collimating and concave mirrors, a diffraction grating and a photodetector. The incident light in the first step of this process is directed through an optical fiber into an entrance slit, which vignettes the light as it enters the spectrometer. Following this, the divergent light is collimated by a concave mirror and directed onto a grating. The grating disperses the spectral components of the light at different angles. The light is then focused by a second concave mirror and imaged onto the detector. When the light is imaged onto the detector, the output signal is digitized. Subsequently, the software of Nkd system interpolates the signal and plots this as a function of the wavelength range.



Figure 4-5: Optical image of Nkd-7000 spectrophotometer.

4.1.6 Scanning electron microscope

A scanning electron microscope (SEM) is used to study the surface morphology of textured Si substrates. This is achieved by a JEOL JSM-7001F ultra-high resolution FESEM as shown in Fig. 4.6. A sample is loaded into the vacuum chamber, and the surface is cross-scanned by the electron beam. This system has a Schottky Electron Gun, an acceleration voltage range of 0.5 kV-30 kV, a magnification range of 10-500000 X and a resolution down to 1.2 nm at a power of 30 kV. During the analysis, an electron beam is focused onto the surface of the loaded sample, resulting in the generation of secondary electrons. By



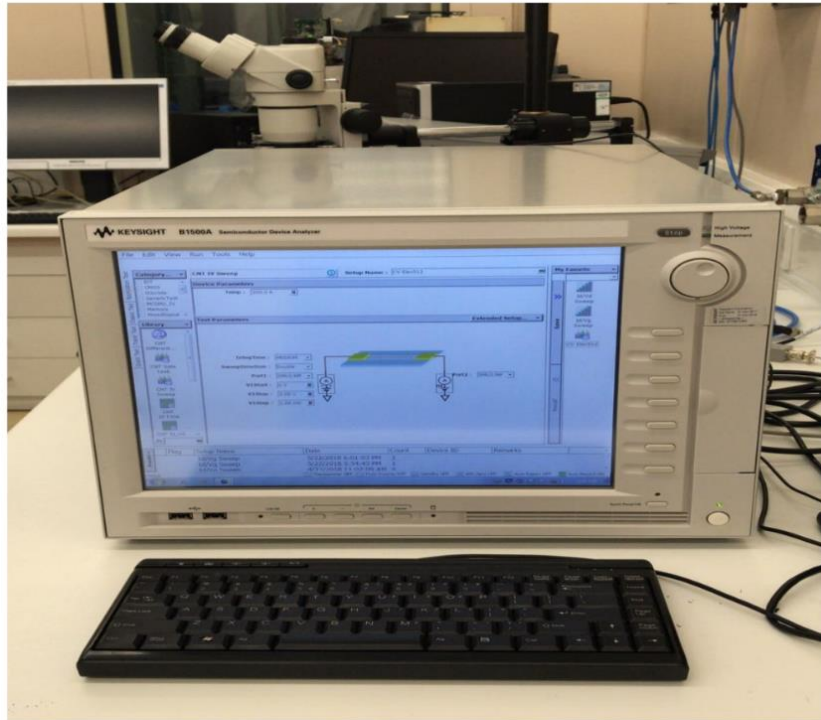
Figure 4-6: Optical image of JEOL JSM-7001F field enhanced SEM.

analysing these electrons using the software of SEM, the topographical image is obtained.

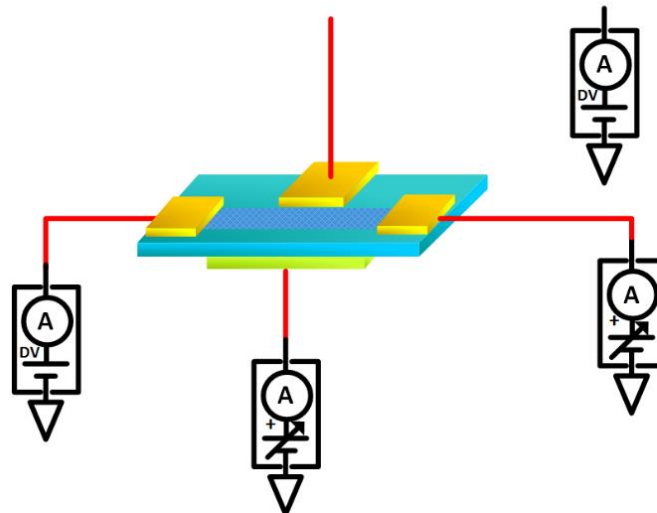
4.1.7 Key-sight B1500A semiconductor Analyzer

The Key-sight B1500A semiconductor Analyser shown in Fig. 4.7a has been used to measure the electrical characteristics of gFETs and graphene/Si Schottky junction solar cells. Fig. 4.7b shows the set-up of a gFET measurement, where the source-drain voltage is varied from 50 mV to 2 V, and the back gate voltage is varied from -100 V into 100 V depending on the specific measurement. The scanning time is fixed at 100 ms. By using the set-up shown in Fig. 4.7c, the performance of solar cells is measured under 1.5 AM and 100mW cm² illumination intensity halogen lamp conditions, and the applied voltage during measurements is between 0.1 and 1 V. A standard commercial Si solar cell has been used for the calibrating measurement.

(a)



(b)



(c)

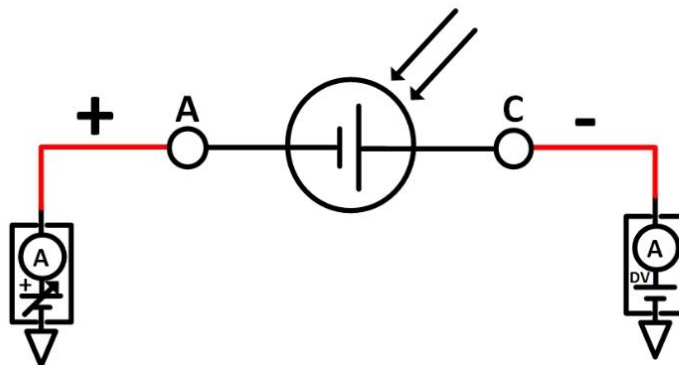


Figure 4-7: (a) Optical image of Keysight B1500A semiconductor Analyzer. (b) Sketch of I_D-V_G and I_D-V_D measurements. (c) Sketch of a J-V measurement of the solar cell.

4.1.8 PVE300 photovoltaic external quantum efficiency system

External Quantum efficiency (EQE) measurement is one of the most significant characterisation tools for solar cells. An *EQE* measurement of the prepared graphene/Si Schottky junction solar cells is carried out using a PVE300 photovoltaic *EQE* system at Bentham Instruments Ltd. This system consists of a Xe lamp source with a wavelength range from 300 to 1800 nm, a collimating lens, Chopper, filters, a monochromator and digital conversion software. The principle of this system is to count the ratio of the number of carriers collected in a solar cell to the number of photons incident upon the solar cell, which is called an *EQE*. To achieve this measurement, it is necessary to shine light on the cell. The monochromator is used to vary the wavelength of incident light, which is modulated at 30 Hz frequency. When the incident light is absorbed, electron-hole pairs are generated through whole Si substrates as a function of wavelength. By using the digital conversion software, the spectrum of the EQE as a function of wavelength is obtained. Based on the EQE-setup method, the value of EQE is equal to the ratio of the short-circuit current density (J_{SC}) to the number of incident photons per second as the following equation [166]:

$$EQE(\lambda) = \frac{\text{number of collected carriers}}{\text{number of incident photons}} = \frac{I_{SC}}{\text{photons/second}} \quad (4.2)$$

4.2 Experimental techniques

4.2.1 Wet transfer process of CVD-graphene

A wet transfer process has been used to transfer CVD-graphene layers, which are grown on both sides of Cu foil and purchased from Graphene Supermarket, onto desired substrates (Si or SiO₂/Si substrate) as shown in Fig. 4.8.

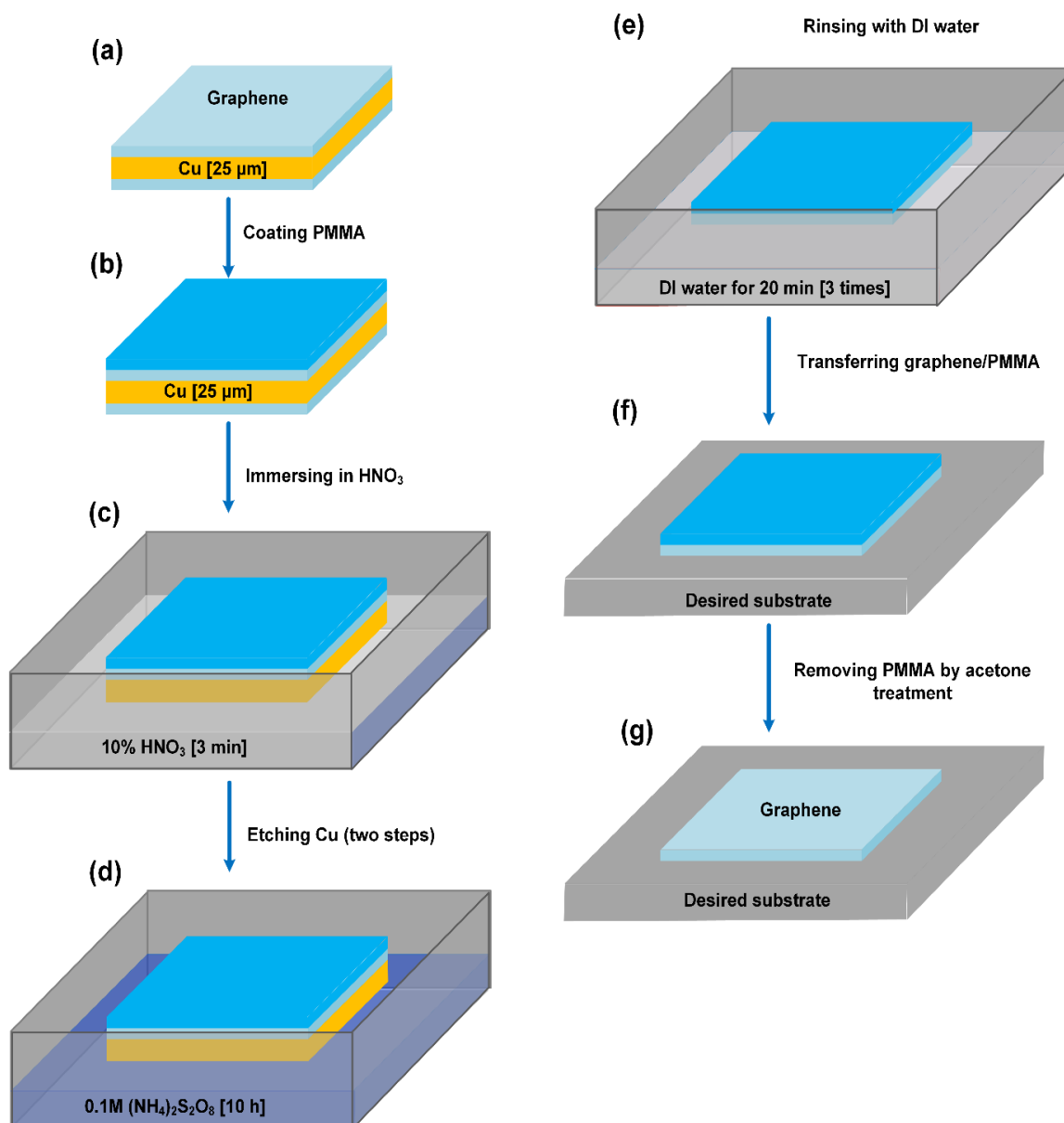


Figure 4-8: Wet transfer process steps. (a) Commercial monolayer graphene is on both sides of 25 μm Cu foil. (b) Coating of one graphene layer with PMMA. (c) Etching the graphene layer at the bottom side is by 10% HNO₃. (d) Etching of Cu foil is by 0.1 M Ammonium per-sulphate. (e) Floating of PMMA/graphene layers on DI-water. (f) Transferring of PMMA/graphene layers on the substrate (Si or SiO₂/Si substrate). (g) Removing the PMMA layer with acetone treatment.

Poly (methyl methacrylate) (PMMA) (C₅O₂H₈)_n is dissolved in chlorobenzene with a 10 mg/mL concentration and spin-coated onto the graphene layer at 3000 rpm for 1 min. The resulting PMMA thickness is approximately 90 nm. The advantage of coated PMMA layers is to ensure graphene layers are visible during the transfer procedure in solution and to also protect it from the potential damage

from HNO₃ and mechanical transfer. The sample is then dried on a hot plate at 180 °C for 1 min in the ambient air. Graphene grown on the other side of Cu foil is etched away by floating this side on 10% HNO₃ aqueous solution for 3 min, and then rinsed with DI-water to remove the HNO₃ residue. After that, the Cu substrate is etched in 0.1M ammonium persulfate for approximately 7h with the endpoint determined when Cu is no longer visible. The sample is then etched for an additional 3 h in a separate fresh ammonium persulfate bath to ensure that the Cu is completely removed. The resulting PMMA/graphene membrane is transferred to a rinse bath of DI-water for 20 min and then transferred onto the desired substrate. The sample is at that time dried in a vacuum (10⁻³ Torr) for 3h and baked in air at 220 °C for 5 min, allowing the PMMA/graphene to re-flat. Afterwards, the PMMA layer is removed by using acetone at 50 °C for 30 min and followed by cleaning the sample by IPA and DI-water. Finally, the sample is dried in a vacuum of 10⁻³ Torr for 3h.

4.2.2 Modified Photolithography and Lift-off

A modified photolithography technique as shown in Fig. 4.9 is introduced before the shaping process and forming contacts were processed to avoid a thermal cross-linked sacrificial layer of photoresist (see details about this issue in section 3.4.2). In this case, the lift-off resist (LOR) 3B is firstly spun at 3000 rpm for 30 s onto graphene/desired substrates after the substrates are cleaned by a standard process described later in section 4.3.1. At that time, a pre-baking is done in a fan oven at 175°C for 15 min. Then, samples are spin-coated with S1805 positive photoresist at 3000 rpm for 30 s. To solidify the photoresist, the substrates are pre-baked on a hot plate at 100 °C for 1 min. To process the required patterns as shown in Fig. 4.9c, samples are exposed to UV radiation of 319 nm for 10 s.

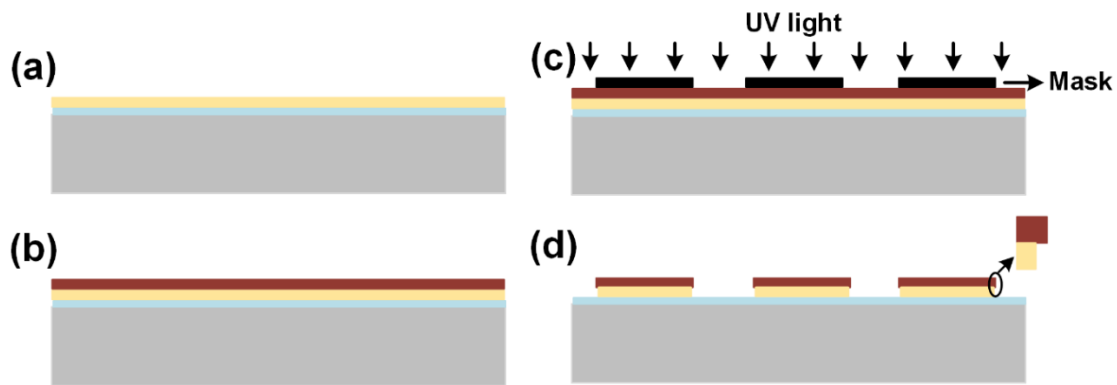


Figure 4-9: Sketch of modified photolithography and lift-off process. (a) and (b) Coating of photoresist/LOR layers onto a graphene/desired substrate. (c) Exposing photoresist/LOR layers to UV. (d) Developing photoresist/LOR layers.

The UV radiation is obtained from an optical Associates INC (OAI) instrument (see Fig. 4.10). Consequently, samples are immersed in the Microposit developer 351 for about 15 s and rinsed with DI-water for 30 s. It can be observed from Fig. 4.9d that the LOR is more developed than the photoresist, and this will enable the photoresist to be easily removed by the Microposit remover 1165 later. After the samples are dried by an N₂ gun, and post-baking is achieved by 254 nm DUV at 180 °C for 2 min. This eliminates the issue of a thermal cross-linked sacrificial layer of photoresist which is later caused by the effect of argon plasma etching or sputtering processes. After samples are processed for shaping or forming contacts, samples are immersed in Microposit remover 1165 at 60 °C for 12 h in order to remove the photoresist/LOR layers. Then, samples are dipped into DI-water to remove only residues, followed by a drying process. At this stage, the lift-off is reached. It can be noticed that the period of remover treatment is long because an ultrasonic bath cannot be used to complete the lift-off process in the case of graphene-based devices. In contrast, for calibrating the thickness of metals which are sputtered or evaporated, a standard photolithography technique is processed since an ultrasonic bath can be employed. In this case, samples are directly spin-coated with photoresist and followed by the same steps



Figure 4-10: Optical Associates INC (OAI) instrument.

as described previously. After the developing process, the post-baking is achieved in a fan oven at 120°C for 15 min. Then, metals are either evaporated or sputtered. To remove the photoresist layer, the samples are immersed in the remover at 60 °C for 8 min and followed by removing the remover residue using DI-water and drying processes.

4.2.3 Modified RF magnetron sputtering Technique

A sputtering technique was used to deposit the required materials with various thicknesses on desired substrates. The sputtering machine (Nordiko Limited) as shown in Fig. 4.11a is firstly warmed up for 30 min in advance. After loading samples into the vacuum chamber, the machine is pumped down until the required vacuum ($<6 \times 10^{-7}$ Torr) was reached and each target is cleaned by an argon plasma at 200 W for 20 min. During the sputtering process, the energetic atoms of argon bombard the target. Then, atoms from the target surface are

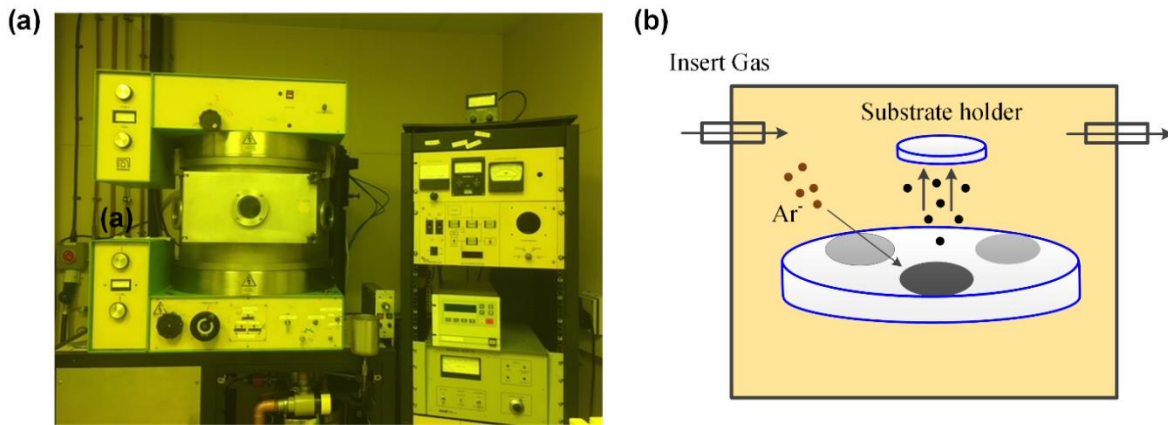


Figure 4-11: (a) Optical image of three targets 8'' sputtering machine (Nordiko Limited). (b) Schematic of conventional sputtering coating technique.

ejected towards the substrate with energy higher than the binding energy as shown in Fig. 4.11b. During the sputtering process, materials (such as Au, Ag and Cr) are deposited in the same way, where atoms deposits toward a substrate via regular trajectories. However, Au atoms deposit with more random trajectories compared with Ag or Cr atoms [156, 161]. This suggests that Au atoms are more likely to coat the edges of the substrate during sputtering, making the unwanted Au film more difficult to be removed during a lift-off process. This also indicates that the number of Au atoms reached to the substrate is lower than that of others. Thus, sputtered Au atoms have less effect on a graphene surface than others. To secure the properties of graphene and avoid issues which are mentioned in section 3.4.2, a sputtering process for all materials is achieved at a low power of 50 Watt and 4 mTorr argon pressure. Additionally, the substrate is water cooled to avoid thermal damage. To ensure a fast cooling process, a heat sink is placed underneath samples during the sputtering process.

4.2.4 Forming Cr adhesive layer using thermal evaporation technique

To evaluate the effect of an adhesive layer on a graphene-metal contact resistance, a layer of Cr is also formed by an Edwards 306 thermal evaporator



Figure 4-12: Optical image of Edwards 306 thermal evaporator.

as shown in Fig. 4.12. In this case, an evaporation process is achieved by tuning the voltage applied between two terminals of a tungsten boat holder containing Cr when the required vacuum of 6×10^{-6} Torr is reached. Once the Cr melts, metal vapour is deposited onto the surface of substrates. Results for the graphene-metal contact resistance for adhesive layers formed by sputtering and evaporating methods are listed in chapter 5.

4.2.5 Modified Argon plasma etching process of CVD-graphene

An etching process supports the study of the electrical characteristics of the transferred graphene sheet. Additionally, it is used to obtain a 0.11 cm^2 graphene area that will be used within the fabrication process. The reason for using such a small graphene area is the quality of Schottkey junction degrades when a graphene area larger than 0.11 cm^2 is used [125, 127]. Additionally, the optical loss of the front contact, which is formed on the graphene surface, is increased

when a large graphene area is employed within the fabrication process [125]. These reasons result in a poor solar cell efficiency. Hence, in my research, the recommended area of graphene sheet in reported works [125, 127] was used to obtain graphene/Si Schottky junction solar cells with high efficiency. After creating requested patterns on graphene sheets using the modified photolithography process, a sample holder as displayed in Fig. 4.13 is placed inside the sputtering machine. Then, this machine is pumped down until the required vacuum of 6×10^{-7} Torr is obtained. It was found practically that applying a plasma etching process for 2 min at a low power of 50 W and 4 mTorr argon pressure is effectively enough to pattern the graphene sheets. Samples are then treated with the lift-off process, followed by drying.

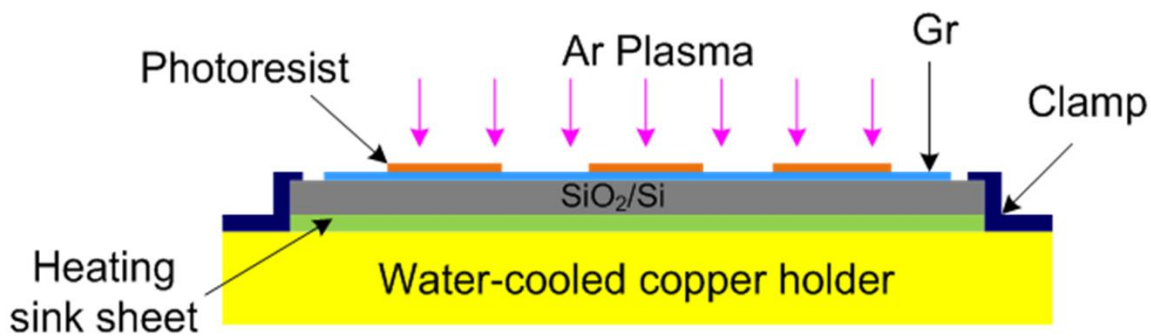


Figure 4-13: Schematic of improved argon plasma etching technique using the heat sink and improved photolithography process.

4.3 Fabrication Process

4.3.1 Substrate cleaning process

Substrates, n-type (100) single c-Si substrates with a resistivity of $2-3 \Omega\text{cm}^{-1}$, 0.19 cm^2 area and thickness of $200 \mu\text{m}$, are cleaned through preliminary and Radio Corporation of America (RCA) processes. For preliminary cleaning process, substrates are immersed in a mixture of H_2SO_4 and H_2O_2 with volume ratios of 2:1 to 4:1 at a temperature of $100-130 \text{ }^\circ\text{C}$ for 10-15 min. Organics are destroyed

and eliminated by wet-chemical oxidation, but inorganic contaminants such as metals are not desorbed. Substrates after this cleaning step are highly contaminated with sulfuric residues from the sulphuric acid. Rinsing substrates with DI-water for 2 min is required to completely remove this viscous liquid. The RCA process is then designed to dissolve and remove alkali residues and any residual trace metals on the silicon surface. The first step of this process is called a Standard Clean-1 (SC-1). Substrates at this time are dipped in 5:1:1 to 7:2:1 parts by volume of H₂O, H₂O₂, and NH₄OH. Treatment of substrates can be varied from 5 to 10 min at 70-75°C and followed by a quench and an overflow rinse in running DI-water for 2 min. Standard Clean-2 (SC-2) is the next step. This step involves immersing substrates in a composition of 6:1:1 parts by volume of H₂O, H₂O₂, and HCl for 5 min at 75 °C. Then, substrates are rinsed in cold running DI water for 2 min. After that, substrates are dipped in 2% HF for 15 s to remove native oxide and followed by a DI-water rinse for 30 s and drying.

4.3.2 Device Fabrication

To overcome difficulties of the fabrication process for reported graphene/Si Schottky junction solar cells (see section 3.4), a novel graphene/Si Schottky junction solar cell with a back-contact structure is prepared. After cleaning a Si substrate, a monolayer CVD-graphene is transferred using the wet transfer process onto substrates. To reduce the PMMA residue, which is discussed in section 3.3, left on graphene layers, annealing in a forming gas with and without formamide treatment is introduced as described in Chapter 5, while DUV treatment is applied in Chapter 6. Then, the shaping process is applied to obtain a 3.3 × 3.3 mm² graphene area after the sample was processed by the modified photolithography technique. At that time, 5nm Cr/150 nm Ag layers are formed as a cathode on the backside (unpolished side) of substrates. In this case, a Cr

layer is evaporated, and the Ag layer is sputtered. For the grid electrode, Cr/Au (5 nm/50 nm) layers are created onto the surface of graphene. A Cr layer, in this case, is evaporated, and the Au layer is sputtered. To reduce the reflected light from the front surface of Si substrates, anti-reflection coatings and a texturing process are employed. In the case of anti-reflection coatings, SiO₂ and SiO₂/TiO₂ layers as SLAR and DLAR coatings are sputtered at room temperature on Si substrates, where this technique is used in chapter 5. In the case of a texturing process, optimum KOH solution is used to create pyramid-like structures on Si surfaces as described in Chapter 6. To obtain p-doped graphene sheets, 65% HNO₃ is applied.

For a graphene-based field effect transistor (gFET), after transferring a graphene layer onto a 300nm SiO₂/Si substrate and applying the shaping process, Cr (5nm) /Au (50nm) layers are formed on a graphene channel as electrodes. In this case, the Cr layer is created using the evaporating and sputtering methods, and Au is again sputtered.

5 Novel graphene/n-Si Schottky junction solar cells with a back-contact structure

5.1 Introduction

In this chapter, a graphene/Si Schottky solar cell with a new back-contact structure is demonstrated to overcome the disadvantages of fabrication processes, which are stated in section 3.4, for reported graphene/Si Schottky junction solar cells. This device has benefits of a larger active area (0.19 cm^2), a simpler fabrication process and lower fabrication cost in comparison with devices fabricated with the previous structures. Instead of ferric chloride and ferric nitrate, ammonium persulfate is used within the wet transfer process to etch the Cu substrate and reduce the chemical residue left on a graphene layer (see section 3.3 for details). Additionally, the etching process using an argon plasma is successfully applied through the fabrication process of solar cells to obtain the optimum area of the graphene layer. In this case, a novel DUV treatment is included in the lithography process as a post-backing to remove the thermal cross-linked sacrificial layer of photoresist caused by the effect of argon plasma etching (see sections 3.4.2, 4.2.2 and 4.2.5 for more details). Furthermore, the Au electrode is formed by a sputtering method after introducing an evaporated Cr layer, resulting in a significant improvement in the contact resistance (see sections 3.4.2, 4.2.3 and 4.2.4). Moreover, the origin of the s-shape J - V behaviour, which is discussed in section 3.4, in graphene/silicon Schottky junction solar cells is systematically investigated, where a forming gas mixture (95% Ar/5% H_2) is engaged to decrease the PMMA residue reported in section 3.3, reduce the effect of s-shape and improve solar cell efficiency. An additional novel technique using formamide treatment in combination with an annealing process in forming gas has been also employed to further decrease the PMMA

residue, successfully suppress the behaviour of distinctive s-shaped kinks and improve the solar cell efficiency. To reduce the reflection from the silicon substrate, anti-reflection coatings (ARCs) are coated on Si substrates. The chemical doping process is also involved to increase the p doping level in graphene, leading to an extra improvement in solar cell performance.

5.2 Graphene/n-Si Schottky junction solar cells based on a back-contact structure and an improved wet transfer process

In this section, the physical and electrical characteristics of graphene sheets transferred using the improved wet transfer process were studied. Graphene/n-Si Schottky junction solar cells based on the back-contact structure and improved wet transfer process were also prepared under the optimized conditions of a shaping process and low metal-graphene contact resistance. Then, current density-voltage (J - V) characteristics of fabricated graphene/n-Si solar cells were investigated.

5.2.1 Physical characteristics of transferred graphene using an improved wet transfer process

Monolayer graphene layers were successfully transferred onto Si and SiO₂/Si substrates using the improved wet transfer process. Ammonium persulfate was employed through the wet transfer process to etch the Cu substrates. An optical microscope and AFM were used to investigate the surface morphology and roughness of transferred graphene layers. An optical image of a 60×60 μm² area of the transferred graphene is shown in Fig. 5.1a. It can be clearly observed that there are spots of residual PMMA on the transferred graphene. These spots affect the electrical properties of graphene and the contact between the graphene and electrodes [122, 125, 167]. Fig. 5.1b shows a non-contact AFM image of a

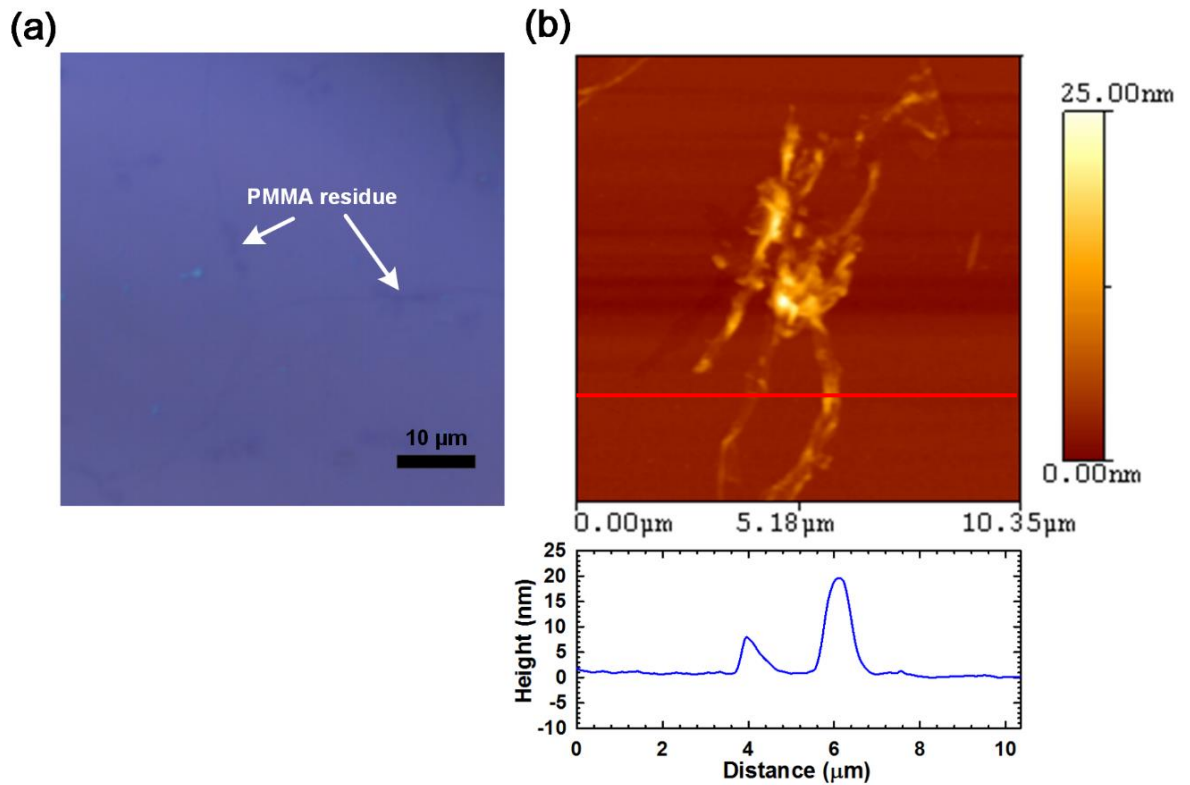


Figure 5-1: (a) and (b) Optical and AFM images of the transferred monolayer graphene onto SiO₂/Si substrate using improved wet transfer process, respectively.

10.35×10.35 μm² area of the transferred graphene. A significant amount of PMMA residue can be seen, which causes a rough surface of the graphene. To verify the quality and monolayer nature of transferred graphene, Raman spectroscopy was employed. As shown in Fig. 5.2a, the G band is at 1590 cm⁻¹ and originates from sp² hybridized carbon, whereas the 2D band at 2704 cm⁻¹ originates from two-phonon inelastic scattering. This data is in an agreement with that of reported works [122, 168]. The intensity ratio of the 2D to G (I_{2D}/I_G) bands for graphene is around 1.6. It can also be observed that there is a peak for the D band in the spectrum of transferred graphene at 1357 cm⁻¹. This is due to defects participating in double resonance Raman scattering near the K point of the Brillouin zone and PMMA residue [56, 57]. X-ray photoelectron spectroscopy (XPS) (Kratos AXIS Ultra DLD spectrometer, monochromatic Al Kα emission at

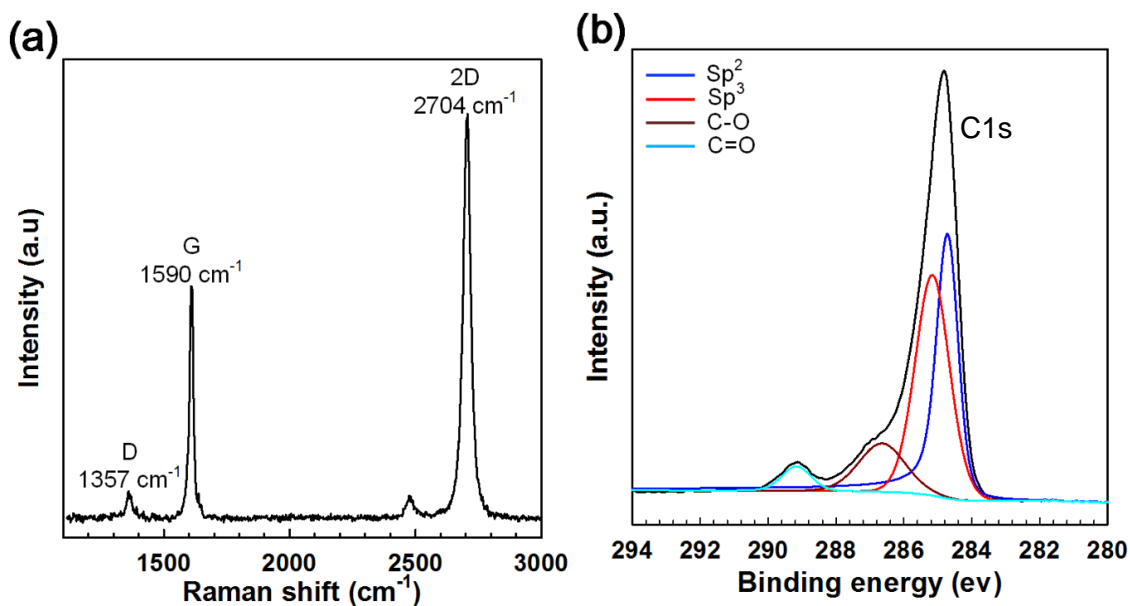


Figure 5-2: (a) Raman spectrum of transferred graphene onto SiO₂/Si substrate. (b) C1s XPS data of transferred graphene on SiO₂/Si substrate, the blue peak corresponds to graphene, and others indicate PMMA residue.

1486.6 eV with an operating power of 150 W) was also engaged to further examine the PMMA residue on the transferred graphene layers. As shown in Fig. 5.2b, there are five peaks for C 1s core-level spectra. The red peak (Sp²) corresponds to graphene, and the other peaks (Sp³, C-O and C=O) attribute to the PMMA residue. The C 1s background signals were subtracted by using the Shirley background model in the peak fitting. The Sp² component was modelled by using the asymmetric Doniach–Sunjic line shape [169], whereas other spectral components fitted by a Gaussian/Lorentzian product formula corresponded to the different [167, 170, 171]. The peaks of this residue can be clearly observed. This provides additional proof that there is PMMA residue left on graphene layers after the removal of PMMA layers by acetone treatment. Thus, on the basis of the physical characteristics, it can be concluded that the wet transfer process causes PMMA residue on transferred CVD-graphene since the acetone treatment could not completely remove the PMMA layer [45, 98-101].

5.2.2 Electrical characteristics of transferred graphene using improved wet transfer process

To study the electrical characteristics of transferred graphene, a graphene-based field effect transistor (gFET) was fabricated. Two novel techniques for the shaping process and forming Au contacts were introduced within the fabrication process of devices to obtain efficient graphene-based devices, as described in the following sections.

5.2.2.1 Novel shaping process of graphene using Argon plasma

Instead of oxygen plasma, argon plasma with a low power of 50 Watt was applied to pattern CVD-graphene. The quality and monolayer nature of graphene patterned with the standard and modified lithography process was investigated by an optical microscope and Raman spectroscopy as shown in Fig. 5.3. Fig. 5.3a shows an optical picture of graphene channels processed with the argon plasma and the standard lithography process. It can be observed that the photoresist (a cyan coloured layer) was left on the graphene channel after the standard chemical cleaning process although the unwanted graphene was completely etched away. This indicates that an outer layer of the photoresist melted, due to the high local temperature of argon ions during the shaping process, and linked the edges of the graphene channel. In other words, the outer layer of the photoresist became a hardened shell on the graphene channel, leading to a reduction in the performance of fabricated devices. This is called a cross-linked photoresist effect [154]. When Lift-off resist 3B (LOR) and photoresist were used within the lithography process, around 50% of photoresist was lifted off after the cleaning process as shown in Fig. 5.3b. LOR in this case was used as an intermediate layer between the photoresist and graphene in order to enable the photoresist to be removed from the graphene surface.

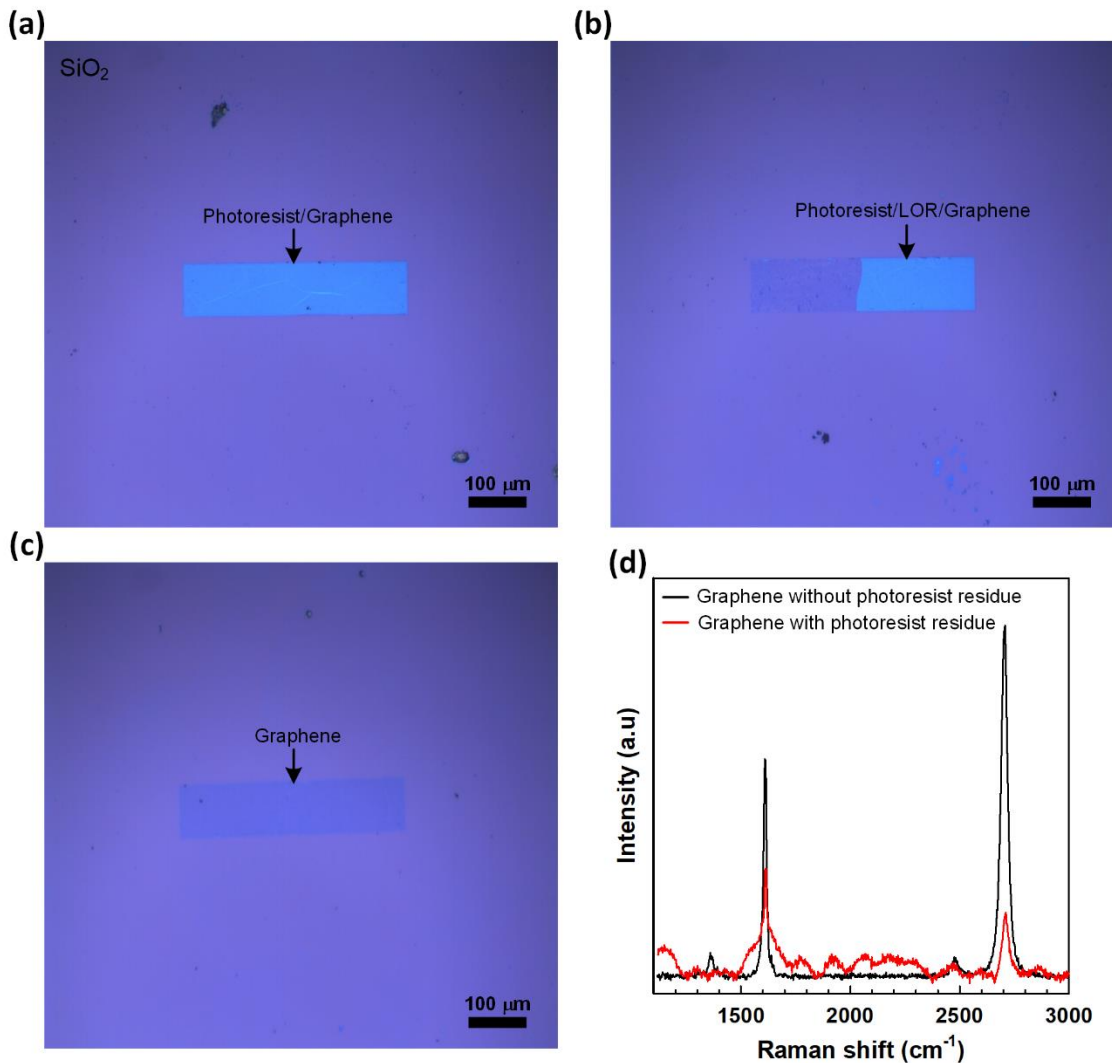


Figure 5-3: (a) and (b) Optical pictures of graphene channels processed with standard lithography without and with LOR, respectively. (c) Optical picture of graphene channels processed with modified lithography processes. (d) Raman spectra of graphene channels patterned with and without modified lithography process.

However, about 50% of the graphene channel was still covered with photoresist and LOR. To further reduce the effect of cross-linked photoresist, the post-baking of photoresist was achieved by a DUV treatment at 180 °C for 2 min. As shown in Fig. 5.3c, there is no residue or visible defects on the patterned graphene. The Raman spectra of graphene channels, patterned with and without the modified technique, are shown in Fig. 5.3d. It can be seen that the graphene channel patterned without the improved technique has a broad G band (red curve), representing the effect of photoresist, whilst the application of LOR and DUV has

maintained the properties of graphene in its original state as shown in this figure (black curve). Based on optical and Raman data, it can be said that the undesirable cross-link of the photoresist on graphene was successfully eliminated by using the improved technique. This attributed to the rapid hardening of the photoresist layer by the DUV treatment. Thus, the photoresist layer was successfully lifted off by the cleaning process.

5.2.2.2 Novel sputtering technique of Au/graphene contact

Au contact was efficiently formed using the sputtering technique. To easier remove the unwanted sputtered Au layer by using the conventional lift-off process, the improved lithography process in the previous section was applied to create the requested patterns. Then, a 5 nm Cr layer was formed using sputtering and evaporation methods. After that, a 50 nm Au layer was sputtered at a low deposition rate on each of the Cr/graphene devices. A four-probe/two-probe method, which is explained in section 3.1.2, was used to measure the graphene-metal contact resistance of fabricated devices. A schematic structure of a graphene field-effect transistor (gFET) is shown in Fig. 5.4a. The channel width (W) and length (L) of a device were 80 μm and 90 μm , respectively. Fig. 5.4b shows the current-voltage (I_D - V_D) output curves of the device with a sputtered 50 nm Au/5 nm Cr contact. The linear relation between I_D and V_D indicates that the Au/Cr/graphene contact is ohmic. By using a four-probe/two-probe method, as explained in section 3.1.2, the R_C was 3.9 K Ω , and this value is lower by 10% than that of the reported device, which has sputtered Au contact [85]. This improvement can be attributed to a decrease of the photoresist residue by the improved lithography process. To further minimize the R_C , a Cr layer of 5nm was grown by an evaporation method instead of the sputtering method. Then, an Au layer was sputtered to complete the contact.

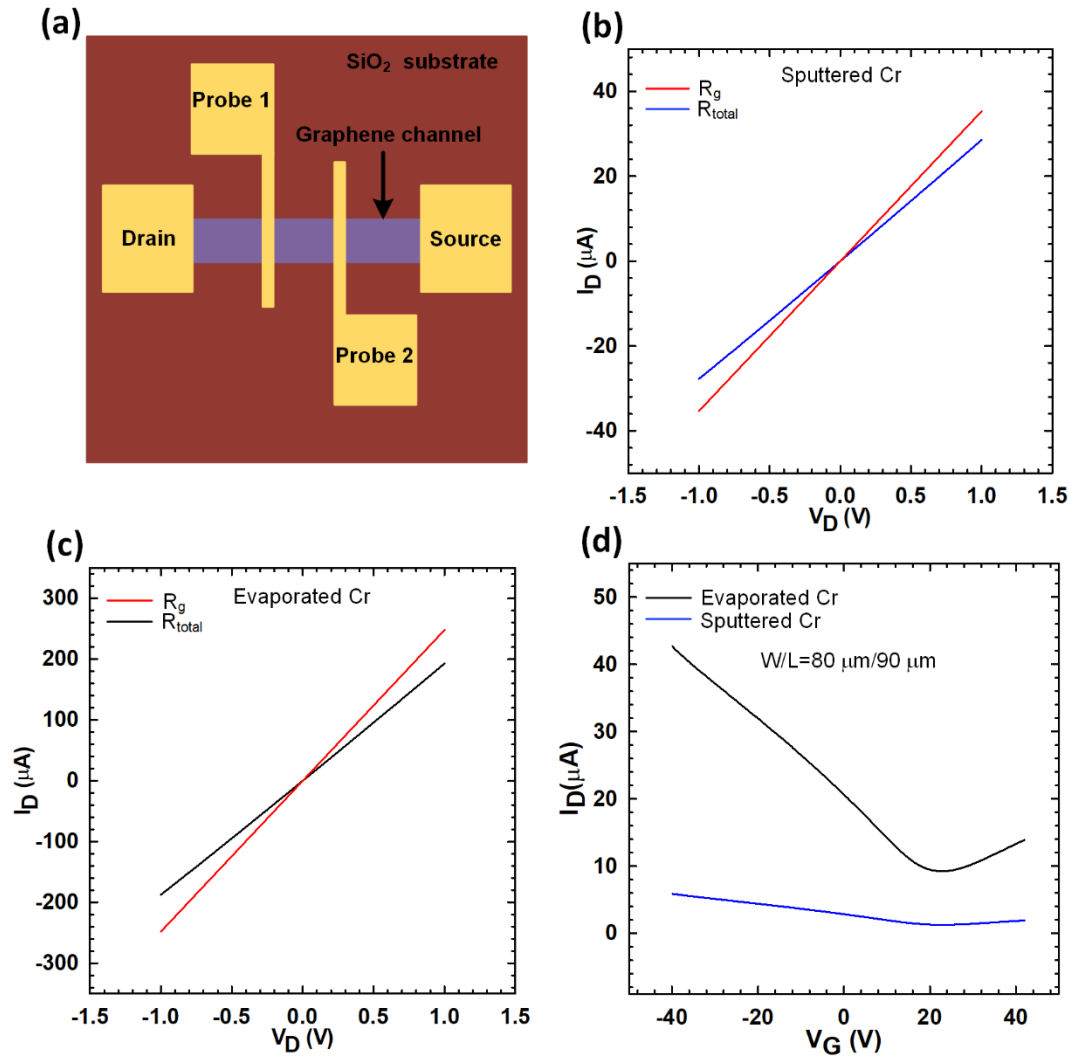


Figure 5-4: (a) Schematic structure of a gFET. (b) and (c) Current-voltage (I_D - V_D) output curves of the gFETs with sputtered and evaporated adhesive layers. (d) Current-voltage (I_D - V_G) transfer curves of the gFETs with evaporated and sputtered adhesive layers.

As shown in Fig. 5.4c, there is also a linear relation between I_D and V_D of this device, and the R_C of this device was 0.6 K Ω . This indicates that the evaporated Cr layer plays a vital role in the provision of a low contact resistance to graphene layers, resulting in an improvement of the performance of graphene-based devices. The four-probe method was also applied to measure the sheet resistance of the transferred graphene onto SiO₂/Si substrates. The sheet resistance in the case of the device had evaporated Cr was around $1150 \pm 50 \Omega \square^{-1}$, while the corresponding value in the case of the second device was $1790 \pm 50 \Omega \square^{-1}$. This also refers to the fact that the deposition method of an

adhesive layer affects the sheet resistance of graphene. To further investigate the conduction level of fabricated devices, the (I_D - V_G) transfer curves were measured in air at room temperature as shown in Figure 5.4d. The gate voltage (V_G) was continuously applied through the backside of devices from -40 to +40 V, and the source-drain bias (V_D) was constant at 10 mV. The field-effect mobility (μ) of holes and electrons can be extracted in this figure from the slope of source-drain current variation from gate voltage to the linear regime as described in section 3.1.2. Where, the contact resistance was not considered when the mobility was calculated. The reason for this is four-probe method is used to measure the (I_D - V_G) transfer curves for gFETs [122]. The mobility of holes and electrons for the gFET device with the evaporated Cr layer were 6304 and 2741 $\text{cm}^2/\text{V}\cdot\text{S}$, whereas the corresponding values for another gFET device were 970 and 485 $\text{cm}^2/\text{V}\cdot\text{S}$, respectively. This indicates that the device with the evaporated Cr layer shows a higher conduction level than that of the other device. This improvement suggests that the evaporated Cr layer maintains graphene layers during sputtering Au atoms. In contrast, the sputtered Cr layer causes defects at Cr/graphene interface since Cr atoms, which have high energetic bombardment during the sputtering process, deposit onto substrates in relatively straight trajectories [172].

5.2.3 Current density-voltage (J - V) characteristics of graphene/n-Si Schottky junction solar cells based on back-contact structure and improved wet transfer process

A new graphene/Si Schottky junction solar cell with a back-contact structure was prepared as shown in Fig. 5.5. A graphene layer was transferred onto the n-Si substrate, using the improved wet transfer process, as shown in Fig. 5.5b. To obtain high graphene/Si solar cell efficiency, a $3.3 \times 3.3 \text{ mm}^2$ graphene area was

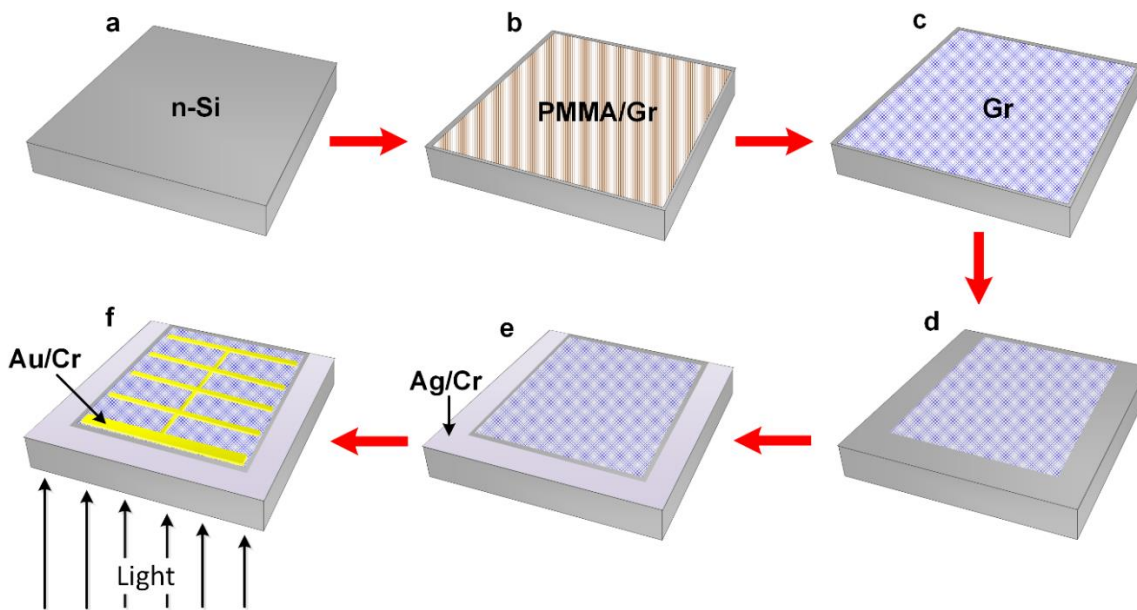


Figure 5-5: Fabrication process of graphene/Si Schottky junction solar cells. (a) Si substrate after the cleaning process. (b) and (c) Transferring PMMA/graphene (Gr) onto the Si substrate using the improved wet transfer process. (d) Applying shaping process to obtain a 3.3×3.3 mm² graphene area. (e) Creating Ag/Cr cathode. (f) Forming Au/Cr grid.

patterned using the modified technique of argon plasma as shown in Fig. 5.5c. Afterward, Ag (150 nm)/Cr (5 nm) layers formed the cathode (see Fig. 5.5d) instead of the InGa eutectic alloy, which reduced the fabrication cost. To form the 70 nm Au/5 nm Cr grid as shown in Fig. 5.5e, Cr was evaporated and then Au was sputtered.

The device structure is shown in Fig. 5.5e, and it has a number of advantages. In particular, the active area of the device is increased compared with those of the reported devices [125, 127] although the same optimum area of graphene sheets was used. This means that the number of photons absorbed is higher, leading to an increase in the solar cell efficiency. The second advantage of this structure is that the texturing process can be applied effectively within the fabrication process of devices. In this case, the process is only applied to the front surface of Si substrates, and graphene layers are placed on the non-textured side of Si substrates. This avoids the recombination process between the graphene and

textured surface of Si substrates, which occurred in the reported work [131]. The Schottky junction in this structure is formed at the interface between the graphene and silicon as shown in Fig. 5.6. It can be seen that carriers are generated throughout the whole Si wafer thickness by the incident light. Then, generated carriers will be separated by the built-in field at the graphene/Si junction. After that, electrons and holes will move in opposite directions, resulting in the generation of the photocurrent [37, 38]. Fig. 5.7a shows current density-voltage (J - V) characteristics of graphene/ n -Si Schottky junction solar cells based on back-contact structure and improved wet transfer process.

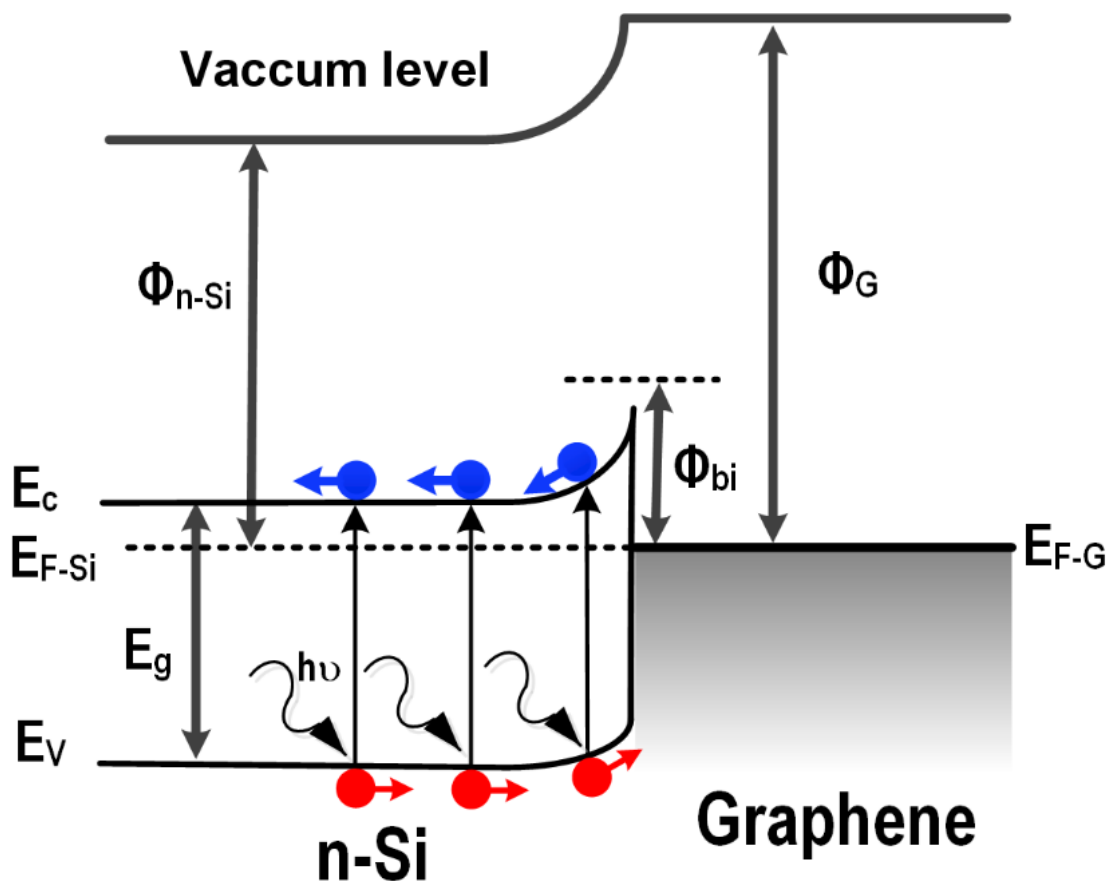


Figure 5-6: Schematic energy diagram of a device and photo-excited electron transfer, indication the photo-generation process which done at a Si substrate then electrons move in the opposite direction to that in the case of holes.

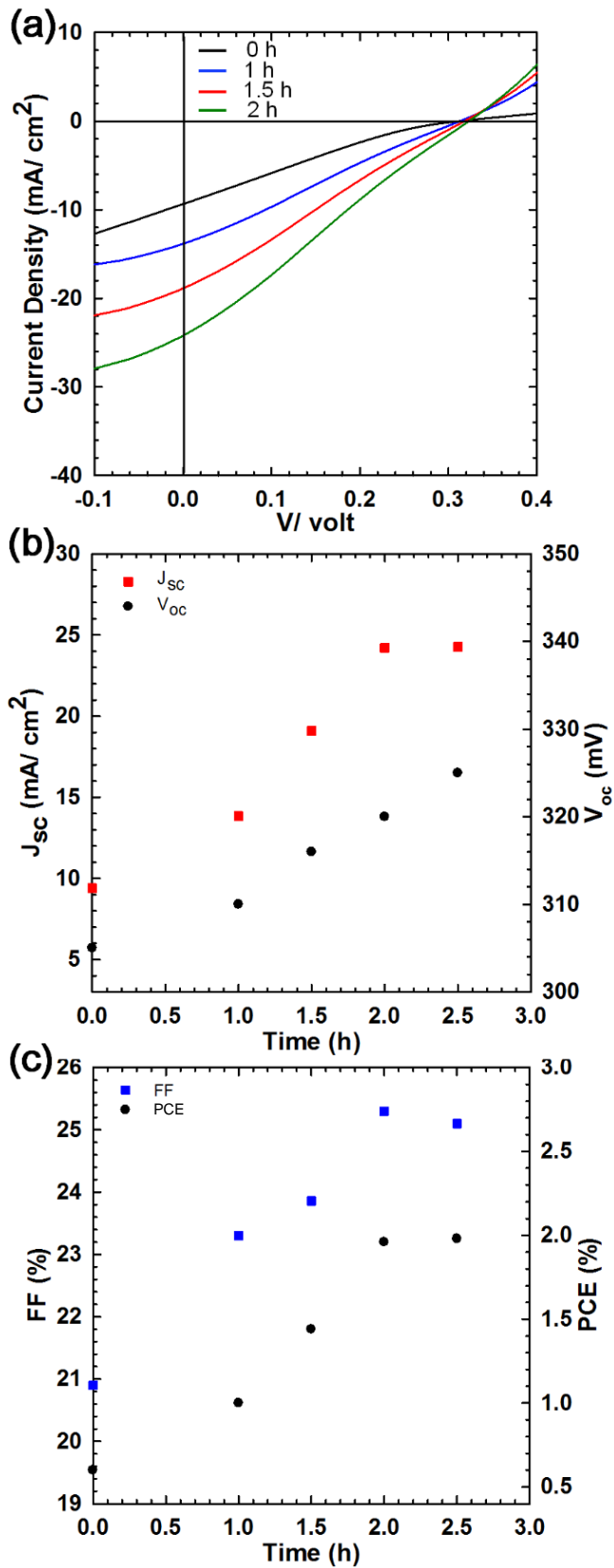


Figure 5-7: (a) *J-V* characteristics of graphene/Si Schottky solar cells treated with forming gas for different periods. (b) and (c) Improvements of V_{oc} , J_{sc} , *FF* and *PCE* of treated devices for different periods.

The short-circuit current density (J_{SC}), open circuit voltage (V_{OC}), fill factor (FF) and power conversion efficiency (PCE) of this device were 9.4 mA/cm², 0.305 V, 20.9% and 0.6%, respectively. The poor values of FF and PCE were owing to the s-shape in the black (J - V) curve of the device treated with acetone.

In order to improve the performance of the device, an annealed process in a (95% Ar/5%H₂) forming gas at 200 °C for different periods (between 0.5 and 2.5 h) was applied after transferring graphene layers on Si substrates. Fig. 5.7a shows the J - V characteristics of graphene/Si Schottky solar cells treated with forming gas for different periods. As shown in Figs. 5.7a, 5.7b, 5.7c and Table 5.1, the V_{OC} and J_{SC} considerably increased to 0.32 V and 24.21 mA/cm², respectively after annealing for 2 h. This increased the FF to 25.3% and the PCE to 1.96% as shown in Fig. 5.7c and Table 5.1. This indicates that the photovoltaic parameters of devices significantly improved after applying the thermal annealing process although the s-shape is still presented in (J - V) curves, in comparison

Table 5-1: The short-circuit current density (J_{SC}), open circuit voltage (V_{OC}), fill factor (FF) and power conversion efficiency (PCE) of graphene/Si devices treated with forming gas for different periods (average values reported)

Annealing treatment (h)	V_{OC} (mV)	J_{SC} (mA/ cm ²)	FF (%)	PCE (%)
0	305	9.4	20.9	0.6
1	310	13.85	23.3	1
1.5	316	19.1	23.86	1.44
2	320	24.21	25.3	1.96
2.5	323	24.25	25	1.97

with those of the unannealed devices. It can also be noticed that the J_{SC} and PCE of devices annealed in forming gas for longer than 2 h marginally improved compared with those of the device treated for 2 h. However, the FF decreased from 25.3 to 25%. This suggests that the annealing treatment for 2 h was sufficient to improve device performance. To explore the reason for the photovoltaic improvement after the annealing process, Raman spectroscopy, XPS and AFM were employed. In this case, graphene layers were transferred onto SiO_2/Si substrates and followed by annealing for 2 h. Raman analysis shows that the G band is at 1601 cm^{-1} and the 2D band is at 2709 cm^{-1} as observed in Fig. 5.8 (red curve). These values indicate that there is an important blue shift in the spectrum of graphene that was annealed for 2 h, in comparison with those of the un-annealed graphene layer (black curve).

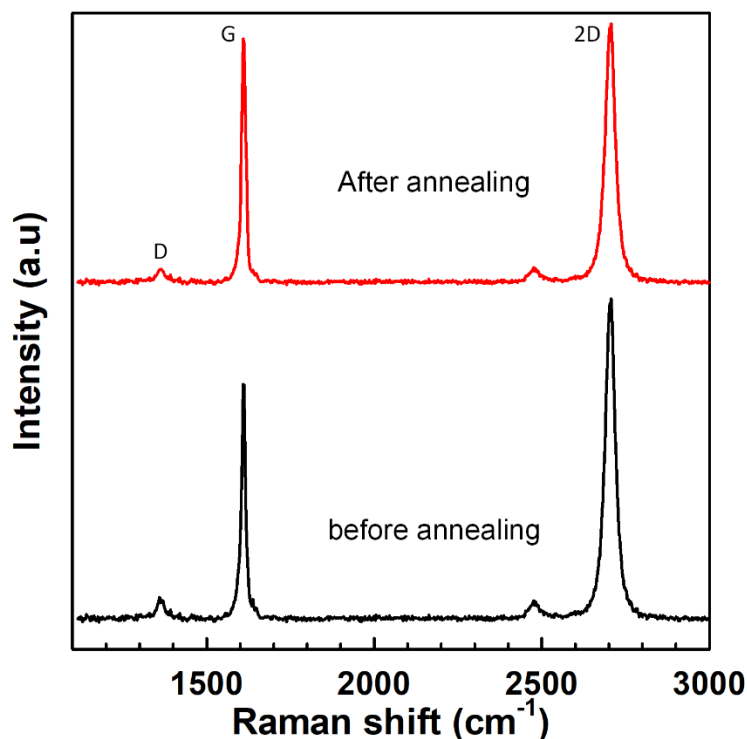


Figure 5-8: Raman spectrum of transferred graphene layers before and after annealing in forming gas for 2 h, showing 2D/G ratio around 1 after annealing.

This data states that the annealing process resulted in p-doping in graphene, and it is in an agreement with reported data [103, 107, 123, 124]. It can also be noted in Fig. 5.8 that the intensity ratio of the 2D to G (I_{2D}/I_G) bands for graphene is around 1.1. This means that the ratio (I_{2D}/I_G) was reduced after this treatment compared with that of the unannealed graphene layer, and the reduction is also due to the p-doping process obtained by the annealing treatment [123]. Fig. 5.9a shows the C 1s core-level spectra of the annealed sample for 2 h. As shown, the peaks of PMMA residue for the annealed graphene layer were marginally reduced compared with those of the sample untreated with the forming gas. Additionally, the peak of graphene was slightly higher than that of the unannealed sample. As presented in Fig. 5.9b, an AFM image of annealed graphene shows that the PMMA residue left on the graphene surface was considerably reduced after the annealing process, compared with that of the unannealed graphene surface. Thus, according to the systematic study achieved by XPS, Raman spectroscopy and AFM, it can be said that the enhancement of photovoltaic parameters after annealing was the result of a further reduction of the PMMA

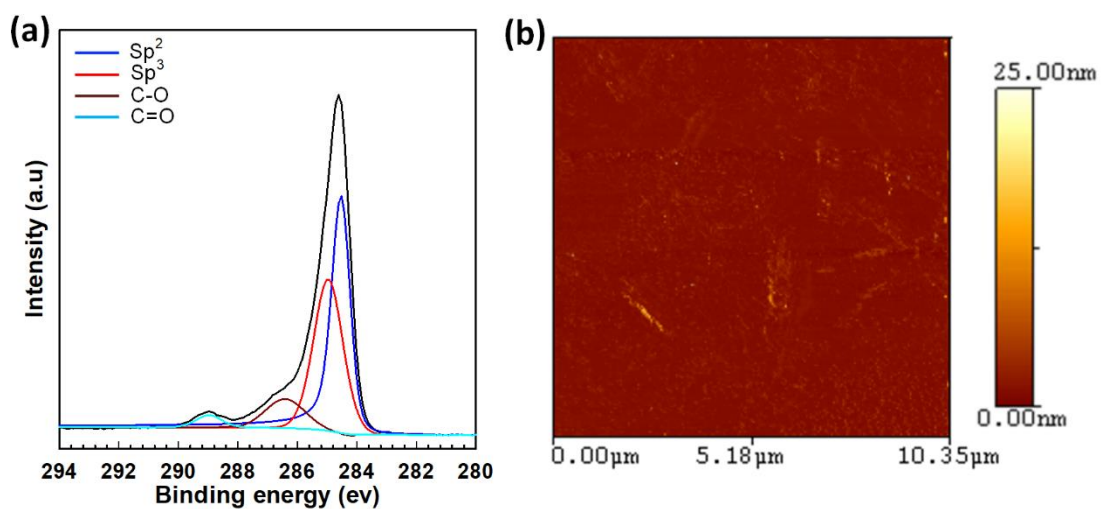


Figure 5-9: (a) and (b) XPS and AFM data of transferred graphene, which was annealed in forming gas for 2 h, onto SiO₂/Si substrates, respectively.

residue on graphene layers and an increase of the p-type doping level in graphene. The chemical doping process using the vapour of 65% HNO_3 for 30 sec was applied to eliminate the s-shape in the J - V curve of the device annealed for 2 h. Fig. 5.10 shows the typical J - V curve (red line) of graphene/n-Si Schottky junction solar cell immediately after the doping process. It can be observed that there is no s-shape in the J - V curve. The values of J_{SC} , V_{OC} , FF and PCE for this device were 24.45 mA/cm^2 , 0.37 V , 44.2% and 4% , respectively. This means that the PCE increased by 100% compared to that of the undoped device. This enhancement is attributed to the improvement of the electrical conductivity of graphene after the doping process [117, 173]. The stability of the treated device with 65% HNO_3 was also examined. In this case, the sample was left in ambient air for a week, then, the J - V characteristic of the doped sample was measured.

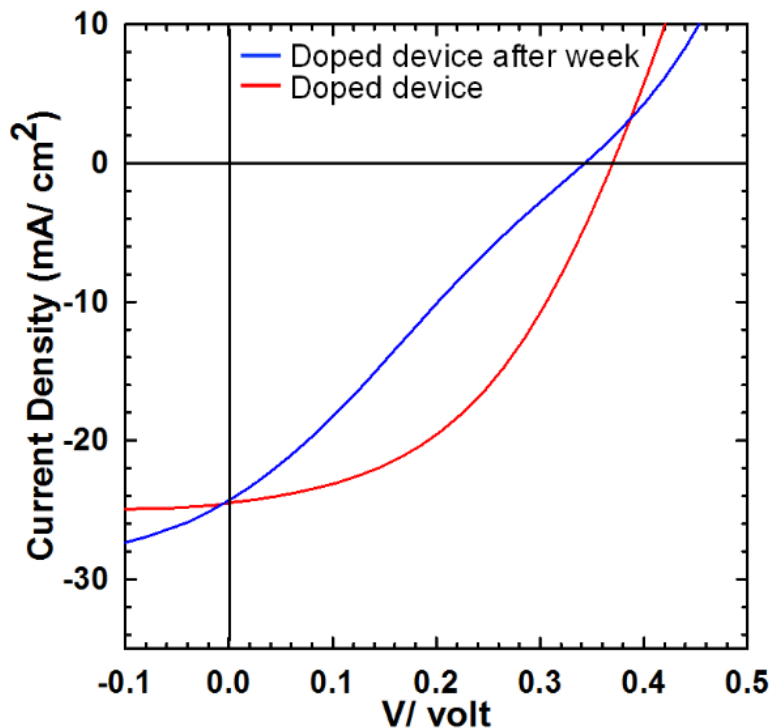


Figure 5-10: J - V characteristics of chemical doped graphene/Si Schottky junction solar cells before and after the doping process.

As shown in Fig. 5.10, the s-shape in the J - V curve (blue line) of doped graphene/n-Si Schottky junction solar cell re-appeared after a week. The values of J_{SC} , V_{OC} , FF and PCE for this device were 24.3 mA/cm², 0.34 V, 30.3% and 2.5%, respectively, which means that the device retained around 60% of its efficiency after the storing process compared with that of the device in the previous stage. It can be realised that the drop in the performance of the stored device was due to a decrease in the V_{OC} and FF values. The V_{OC} decreased as the chemical dopants gradually evaporate during the storage time as confirmed in reported works [141, 174], whereas the decrease in the FF was owing to the s-shape. It can be concluded from the above data that the doping process could suppress the s-shape in J - V curves of graphene/n-Si Schottky junction solar cells for a limited time only. This is in agreement with reported works [133, 135, 136, 140]. This indicates that the s-shape should be eliminated by using a different method instead of the HNO₃ treatment in order to obtain more efficient and stable devices. This also suggests that the PMMA residue should be reduced more as the reduction of this residue could be a key to eliminate the s-shape in J - V curves of graphene/n-Si Schottky junction solar cells, resulting in a further improvement in the solar cell performance.

5.3 Graphene/n-Si Schottky junction solar cells based on back-contact structure and formamide treatment

In this section, a novel technique using formamide treatment in combination with the annealing process in forming gas has been conducted to effectively decrease the PMMA residue and suppress the behaviour of distinctive s-shaped kinks. In this case, samples were firstly immersed in formamide after removing the PMMA layer using the usual acetone process and followed by annealing in an argon/hydrogen (95%/5%) environment for 2 h.

5.3.1 Physical characteristics of transferred graphene using formamide treatment

A surface morphology of graphene transferred using the new technique was verified by an optical microscope and AFM. Fig. 5.11a displays a typical optical image of a $60 \times 60 \mu\text{m}^2$ area of a graphene sheet transferred using the formamide treatment for 30 min before annealing for 2 h. It can be seen that the transferred graphene layer was almost uniform and continuous. A noncontact AFM image of a $10.35 \times 10.35 \mu\text{m}^2$ area of the transferred graphene is shown in Fig. 5.11b. It can be noticed that PMMA residue is significantly reduced on graphene layers compared with that of samples treated with forming gas only. This indicates that the new method results in an effective reduction in the PMMA residue on graphene sheets. The monolayer nature of transferred graphene was evaluated by Raman spectroscopy as shown in Fig. 5.12. It can be observed that the spectrum is for monolayer graphene, and that there is no D band in this spectrum. It can also be noticed that the G band is at 1593 cm^{-1} and the 2D band is at 2706 cm^{-1} , indicating that there is an essential red shift in the spectrum of graphene.

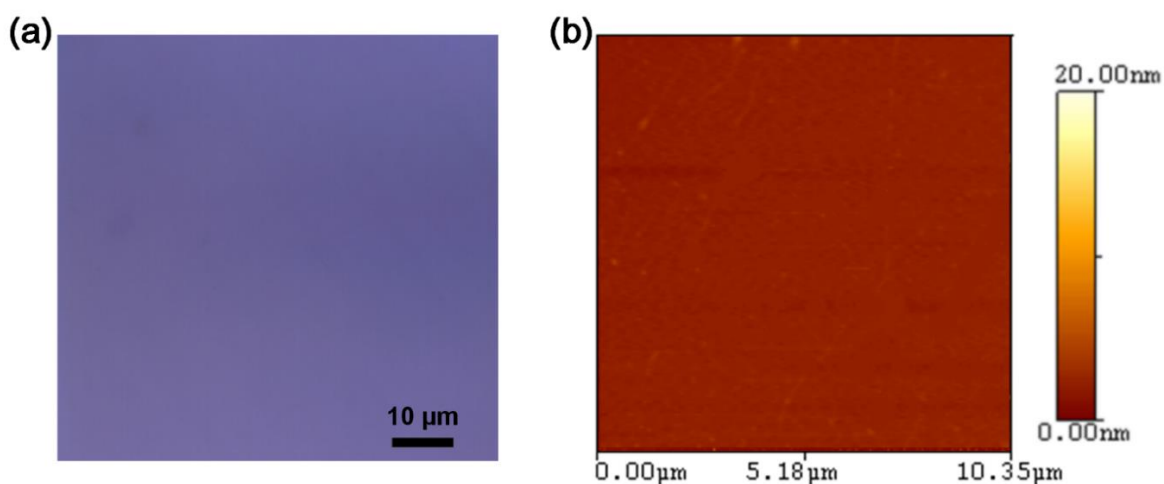


Figure 5-11: (a) and (b) Optical and AFM images of transferred graphene surfaces, which was treated with formamide method, onto SiO_2/Si substrates, respectively.

This shift means that the p-doping level in graphene has reduced [117, 122]. In other words, a graphene layer transferred using the new technique has less PMMA residue compared to that of a graphene layer treated with the forming gas only. The intensity ratio of the 2D to G bands for transferred graphene was around 1.4, showing that the graphene layer transferred using the improved technique has a higher quality of that of the graphene layer treated with forming gas. To further study PMMA residue on transferred graphene layers, XPS was used. Fig. 5.13 shows the evolution of C 1s core-level spectra of graphene after treating with formamide. As shown in this figure, the red peak (Sp^2) of graphene increased compared with those of graphene layers treated with the acetone and forming gas methods. It can also be seen that the Sp^3 , C-O and C=O peaks of PMMA

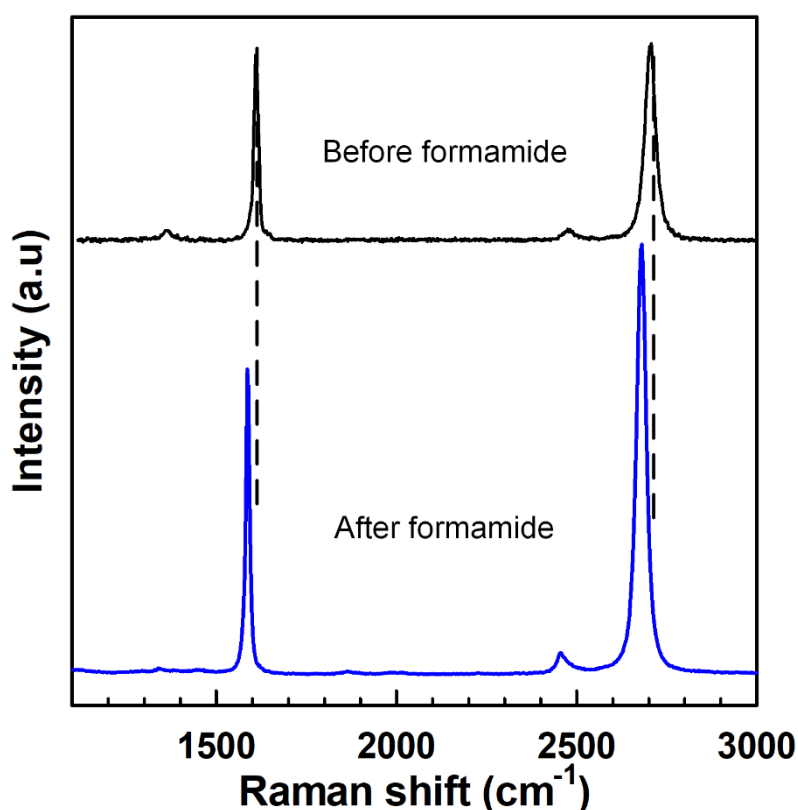


Figure 5-12: Raman spectra of transferred graphene onto SiO₂/Si substrates before and after formamide treatment, showing a red shift in spectrum after this treatment.

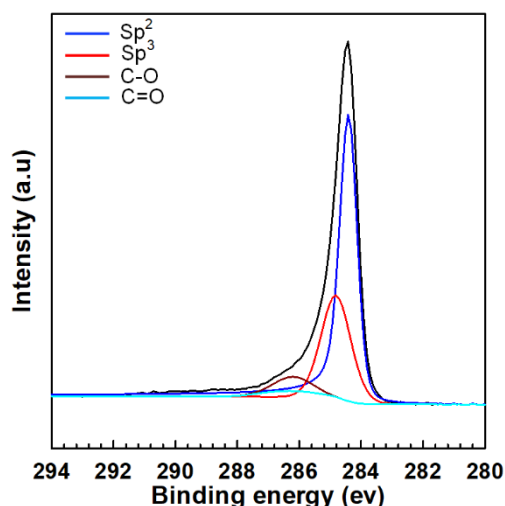


Figure 5-13: XPS data of transferred graphene treated with formamide method onto SiO₂/Si substrates.

residue were considerably reduced, where the NH₂ has the ability to break the C-O and C=O bonds from the PMMA as confirmed in reported works [175, 176]. It can be summarized based on the physical characteristics of transferred CVD-graphene using the formamide treatment in combination with the annealing process that PMMA residue on transferred graphene was effectively reduced to a greater degree than those of graphene layers processed with the previous treatments. This is attributable to the fact that PMMA residue firstly absorbs the -NH₂ functional group in formamide (CH₃NO). This resulted in an electron donation to graphene at the graphene/PMMA residue interface [177-179], leading to minimizing some of the PMMA residue through breaking the C-O and C=O bonds in PMMA. Then, the annealing process further removes PMMA residue. This compensates for p-type doping and effectively restores the intrinsic electrical properties of the transferred graphene layers.

5.3.2 Current density-voltage ($J-V$) characteristics of graphene/n-Si Schottky junction solar cells based on back-contact structure and formamide treatment

The fabrication process of graphene/n-Si Schottky junction solar cells based on the back-contact structure and formamide method is shown in Fig. 5.14. As shown in Fig. 5.14c, after transferring graphene layers onto Si substrates, samples were immersed in formamide for 30 min and then annealed in forming gas for 2 h in order to efficiently reduce the effect of the PMMA residue. Next, the same methodology of shaping process and contacts as for the previous fabrication process in section 4.2.3 was applied. Fig. 5.15 compares the ($J-V$) characteristics of graphene/n-Si Schottky junction solar cells treated with and without formamide for 30 min before the annealing process.

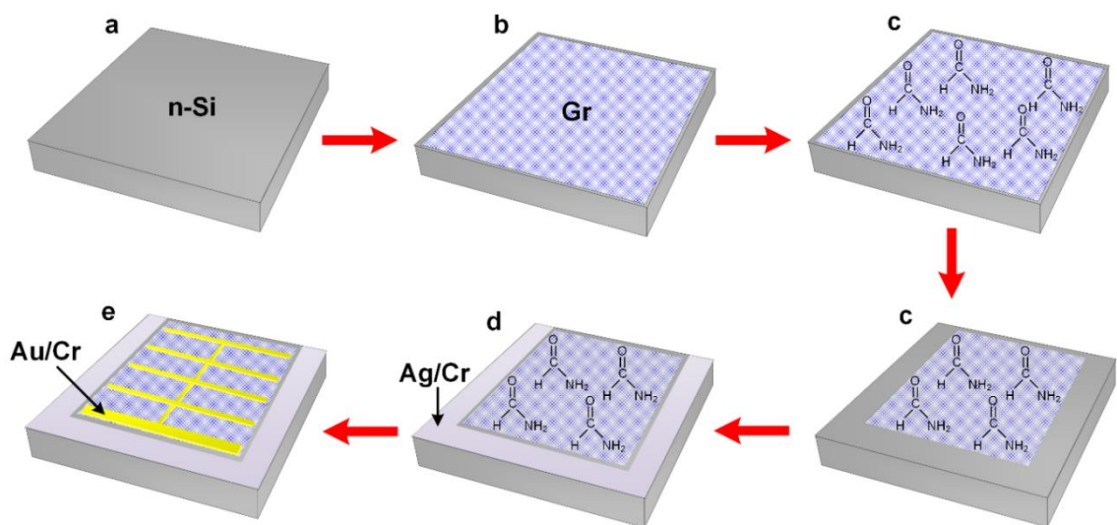


Figure 5-14: Fabrication process of graphene/Si Schottky junction solar cells based on formamide. (a) Si substrate after cleaning process. (b) Transferring PMMA/graphene (Gr) onto the Si substrate. (c) Immersing sample in formamide and followed by annealing in a hydrogen/argon environment for 2 h. (d) Applying shaping process to obtain a 3.3×3.3 mm² graphene area. (e) Creating the Ag/Cr cathode. (f) Forming the Au/Cr grid.

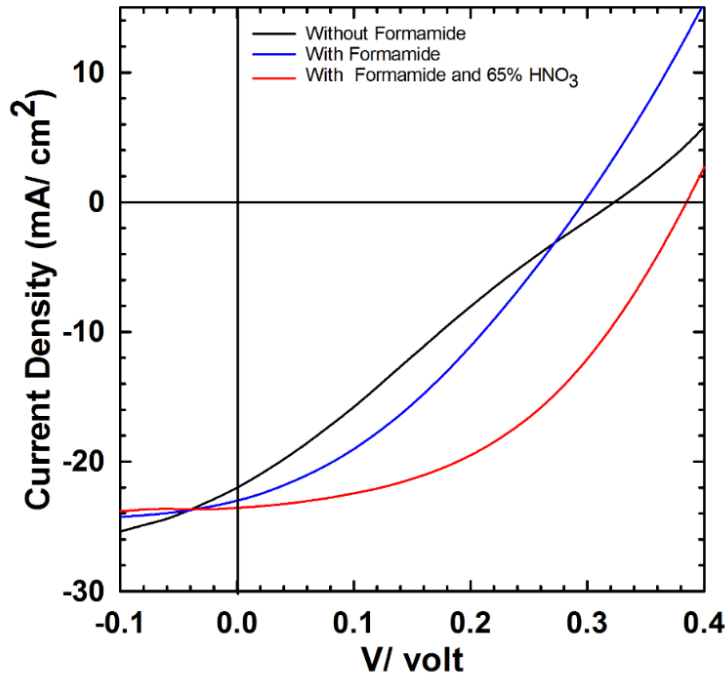


Figure 5-15: J - V characteristics of graphene/Si Schottky solar cells before and after treating with formamide.

It can clearly be observed that the behaviour of s-shape in the J - V curve (blue) of a treated device is efficiently eliminated. In contrast, there is an s-shape in the J - V curve (black) in the case of an untreated device. For the treated device, the J_{SC} , V_{OC} , FF and PCE were 25.3 mA/cm², 0.30 V, 35% and 2.6% respectively. This points out that minimizing the PMMA residue successfully increases the FF by 40%, resulting in an improvement in the PCE by 30% compared with those of the untreated device. This suggests that the PMMA residue acts as a trap for generated carriers during their transmits at the interfaces through the solar cell device, leading to an increase in the recombination process [117, 180]. This causes poor efficiency of graphene/Si junction solar cells. Hence, this confirms that PMMA residue left on graphene layers is the key to the elimination of the s-shape in J - V curves. Table 5.2 shows the comparison of photovoltaic parameters of graphene/Si solar cells reported with different structures. It can be seen that our device displays the highest photovoltaic performance; in particular, the FF

and *PCE* enhanced by about 50% and 60% more than those of the device prepared with the top-window structure. This enhancement is attributed to the usage of the back-contact structure and formamide treatment in the fabrication process. It can also be noticed that there is a decrease in the V_{OC} of our device compared with those of the reported devices since the PMMA residue was reduced. The effect of chemical doping on the performance of the treated device was examined. Fig. 5.15 shows the J - V curve (red) of the device after treating graphene with a vapour of 65% HNO_3 for 30 s, yielding a higher *PCE* of 4.6% with the V_{OC} of 0.38 V, J_{SC} of 26 mA/cm² and *FF* of 45%. This indicates that the enhancement of solar cell performance after the doping process was due to the improvements in the J_{SC} , V_{OC} and *FF*, whereas the enhancement of performance of samples treated with forming gas was owing to the improvements in V_{OC} and *FF*. This attributes to a development in the electrical conductivity of graphene after reducing the PMMA residue using the formamide method as confirmed by the electrical characteristics of gFETs. The (I_D - V_D) output curves of the immersed device are shown in Fig. 5.16. It can be observed that there is an obvious linear relation between I_D and V_D , showing that the contact is still ohmic. The contact resistance at the metal/graphene interface, which was also extracted from this figure using the four-probe/two-probe method, was 110 ohm.

Table 5-2: Comparison of photovoltaic parameters of graphene/Si solar cells reported with different structures

Structure	V_{OC} (mV)	J_{SC} (mA/ cm ²)	<i>FF</i> (%)	<i>PCE</i> (%)	Ref.
Top-window	310	21.4	24	1.57	[132]
Top-grid	350	7.81	21.7	0.59	[125]
Back-contact	300	25.3	35	2.6	This work

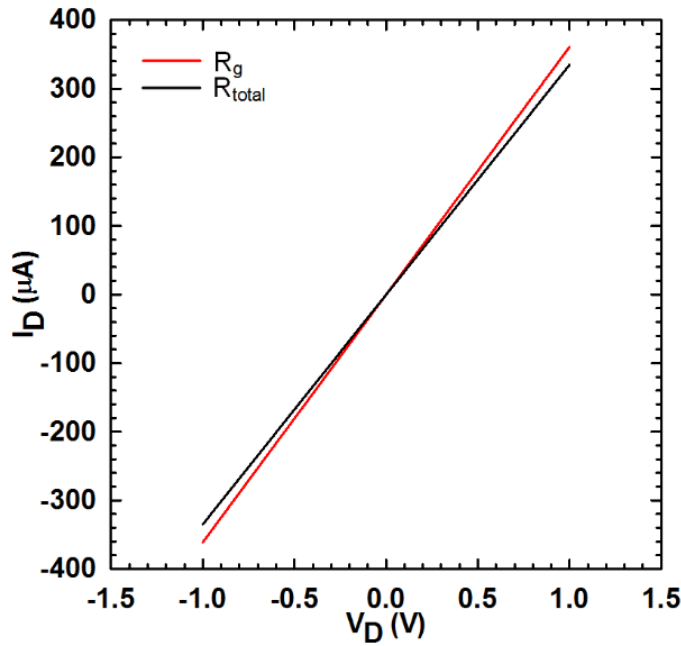


Figure 5-16: Current-voltage (I_D - V_D) output curves of the gFETs treated with formamide.

This value states that minimizing the PMMA residue on the graphene surface reduces the contact resistance by about 83% in comparison with the gFET treated with acetone, resulting in an improvement in the device performance. The sheet resistance of the transferred graphene was in the range of $380 \pm 50 \Omega \square^{-1}$. This means that the sheet resistance of graphene treated with formamide was minimized by around 65% compared to that of graphene treated with acetone only. The values of contact and sheet resistances confirm that reducing PMMA residue enhances the electrical conductivity of graphene and lower the graphene electrode- contact resistance. Fig. 5.17 shows the (I_D - V_G) transfer curves of the gFETs treated with and without formamide. As shown, the V_G was continuously applied through the rear side of devices from -40 to +40 V, and the source-drain bias (V_D) was constant at 10 mV. It can be noticed that the Dirac point of the (I_D - V_G) curve (black line) for the treated gFET was at 17 V, whilst the Dirac point of the (I_D - V_G) curve (red line) for the untreated gFET was at 33 V.

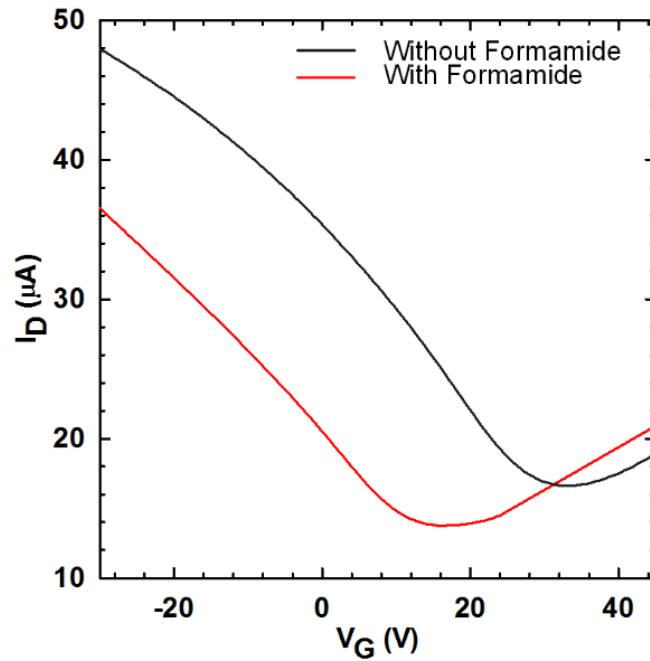


Figure 5-17: Current-voltage (I_D - V_G) transfer curves of the gFETs treated without and with formamide before the annealing process.

This data reveals that there was a shift in the Dirac point towards zero voltage, indicating that the p-doped level in graphene had been reduced. This also confirms that PMMA residue was reduced on graphene layers after treating graphene with formamide. Due to the significant improvement in solar cell performance after formamide treatment, the influence of this treatment on photovoltaic parameters was investigated with different time scales. The J - V characteristics of typical graphene/Si solar cells treated with formamide between 5 and 35 min before annealing are shown in Fig. 5.18a. It can be seen that the s-shape in J - V curves of devices was gradually eliminated with increasing treatment time. Figs. 5.18b, 5.18c and Table 5.3 show the evolution of the V_{OC} , J_{SC} , FF and PCE of these devices. It can be seen that the V_{OC} marginally reduced from 0.32 V to 0.29 V when samples were immersed in formamide between 0 and 35 min since the p-doping level in graphene was decreased.

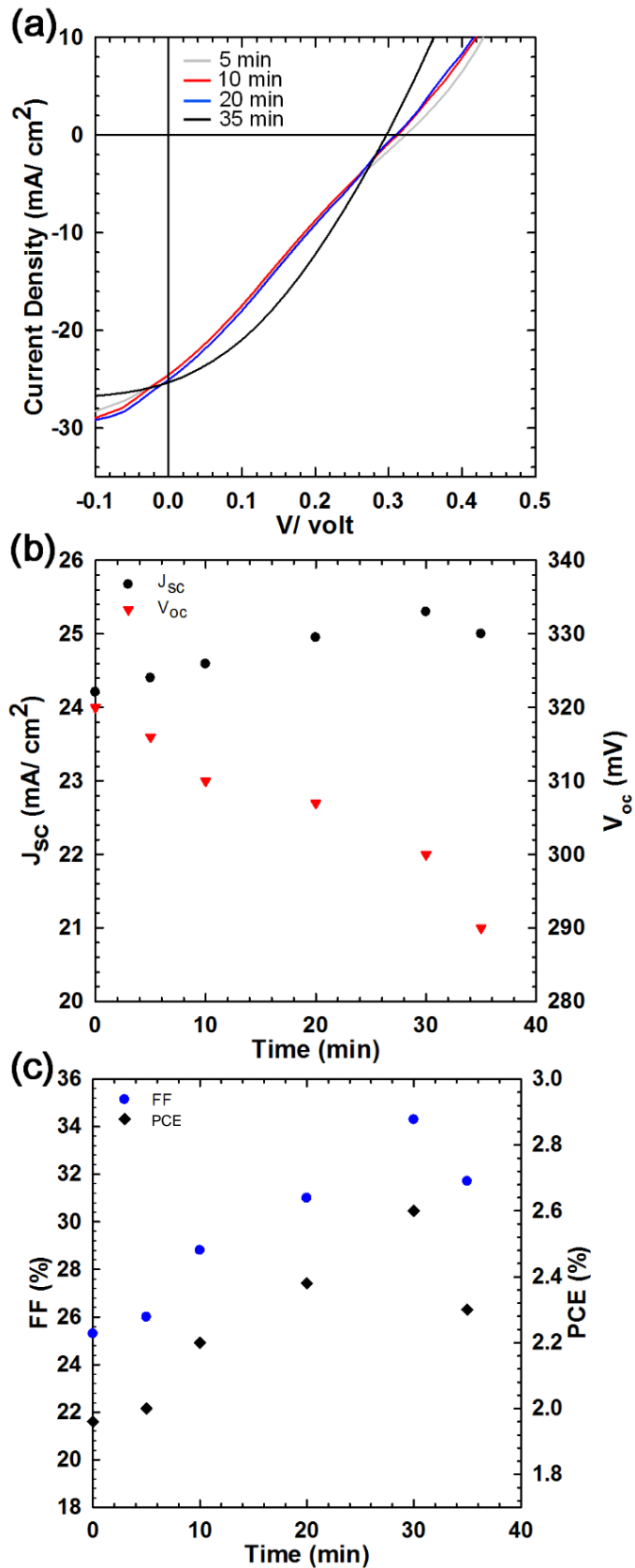


Figure 5-18: (a) J - V characteristics of graphene/Si Schottky solar cells treated with formamide for different periods before applying forming gas process for 2 h. (b) and (c) Enhancements of V_{oc} , J_{sc} , FF and PCE of treated devices for different periods.

Table 5-3: The short-circuit current density (J_{SC}), open circuit voltage (V_{OC}), fill factor (FF) and power conversion efficiency (PCE) of treated graphene/Si devices with formamide for different periods (average values reported)

Formamide treatment (min)	V_{OC} (mV)	J_{SC} (mA/ cm ²)	FF (%)	PCE (%)
0	320	24.21	25.3	1.96
5	316	24.4	26	2
10	310	24.59	28.8	2.2
20	307	24.95	31	2.38
30	300	25.3	34.3	2.6
35	290	25	31.7	2.3

In contrast, the J_{SC} of treated devices significantly improved from 24.21 mA/cm² to 25.3 mA/cm² for samples treated between 0 and 30 min. This enhancement resulted in an increase in the FF and PCE to 34.3% and 2.6%, respectively. The improvement in the current density indicates that the trapping process of charge carriers by the PMMA residue during their transmits at the interfaces was successfully eliminated when devices were immersed in formamide as shown in Fig. 5.19, leading to a decrease in a recombination loss of photo-generated carriers and an increase in the FF . However, formamide treatment for longer than 30 min resulted in a decrease in the J_{SC} of 25 mA/cm², FF of 31.7 % and PCE of 2.3%. In this case, it can be said that the formamide treatment for 35 min caused n-doping in graphene layers [122]. This indicates that the formamide treatment for 35 min is a suitable way to prepare n-graphene/p-Si solar cells (see section 3.4.1). Hence, it is recommended that graphene/n-Si devices should be treated with formamide for 30 min before annealing in order to remove the PMMA residue and improve the solar cell performance. To further improve device performance, the reflected light from the front surface of Si substrates was reduced by anti-

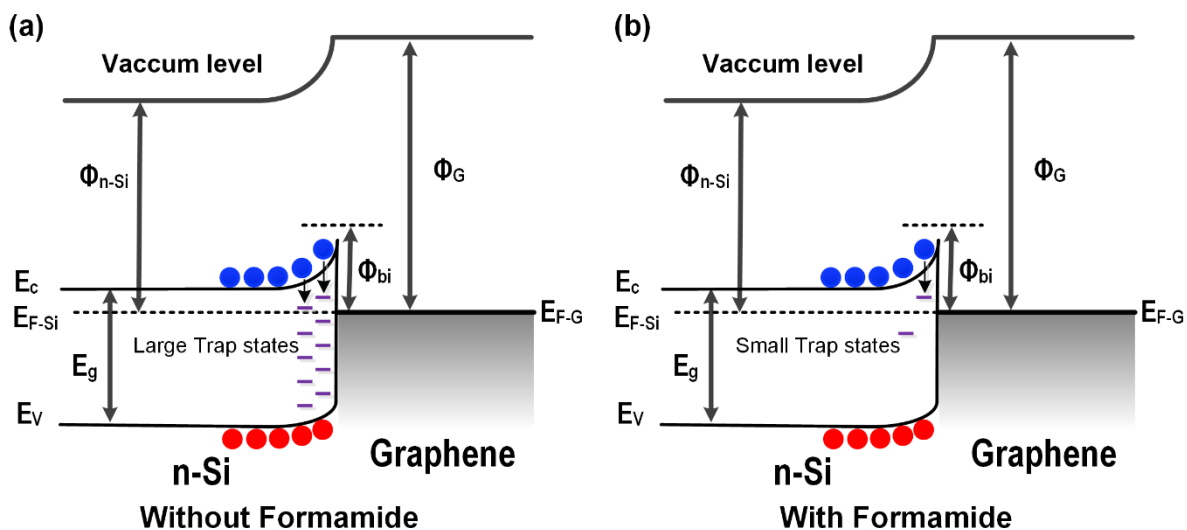


Figure 5-19: (a) and (b) Schematic energy band diagrams of graphene/silicon Schottky junctions treated without and with formamide before annealing process, respectively, indicating to the recombination process of generated carriers due to the trap states of PMMA residue.

reflection coatings. In this case, SiO₂ and SiO₂/TiO₂ layers were sputtered as SLAR and DLAR coatings on Si substrates. To ensure there were no defects, SiO₂ and TiO₂ layers were sputtered at room temperature [181]. Schematic designs of SLAR and DLAR coatings on Si substrates are shown in Figs. 5.20a and 5.20b. The effect of the ARC on the reflectance of Si substrates was investigated using a spectrophotometer with an integrating sphere, and a Si substrate was used as a reference. As shown in Fig. 5.21a, the diffused reflectance (R) of Si substrates with and without coatings is as a function of the wavelength within the range of 400-1000 nm. It can be observed that the average R of the reference Si was around 35% within this range, and the corresponding value was reduced to 17.5% by forming SiO₂ and 4.3% by forming SiO₂/TiO₂, respectively. The *J-V* characteristics of graphene/n-Si solar cells after applying formamide treatment for 30 min, annealing in forming gas for 2h and doping treatment of HNO₃ for 30 sec are shown in Fig. 5.21b. It can be seen that the *J-V* curve (black) of the device fabricated with a SiO₂ layer exhibited a significant improvement in photovoltaic performance in comparison with the fabricated

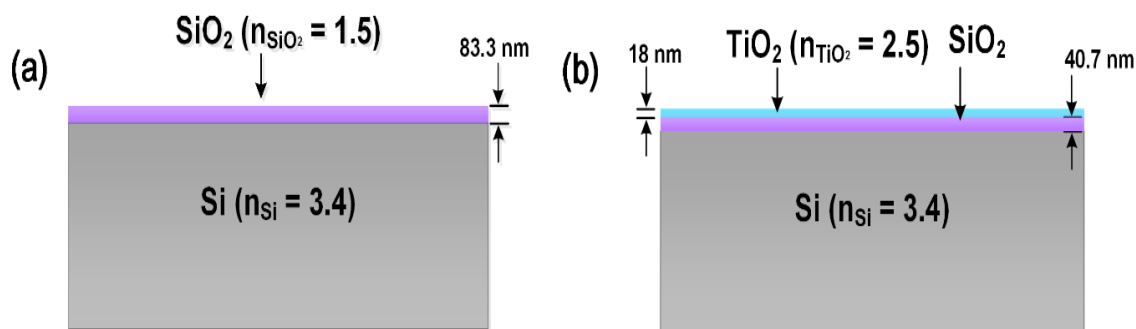


Figure 5-20: Schematic structures of Si substrates with (a) SLAR and (b) DLAR coatings.

Device without a SiO₂ layer (see the red curve in Fig. 5.15), showing a higher J_{SC} of 33.5 mA/cm², V_{OC} of 0.442 V, FF of 47.4% and PCE of 7% as displayed in Table 5.4. This improvement is attributed to the reduction of reflected light by the SiO₂ layer. It can also be observed in Fig. 5.21b (red curve) and Table 5.4 that the device fabricated with DLAR coating exhibits improved photovoltaic performance, in particular, the J_{SC} of around 44 mA/cm². This means that the J_{SC} increased by 10.5 mA/cm² more than the previous device, as the reflection was further minimized. This resulted in an increase in the FF from 47.4 to 50% and PCE from 7 to 9.5%, whereas the V_{OC} for the device fabricated with DLAR coating

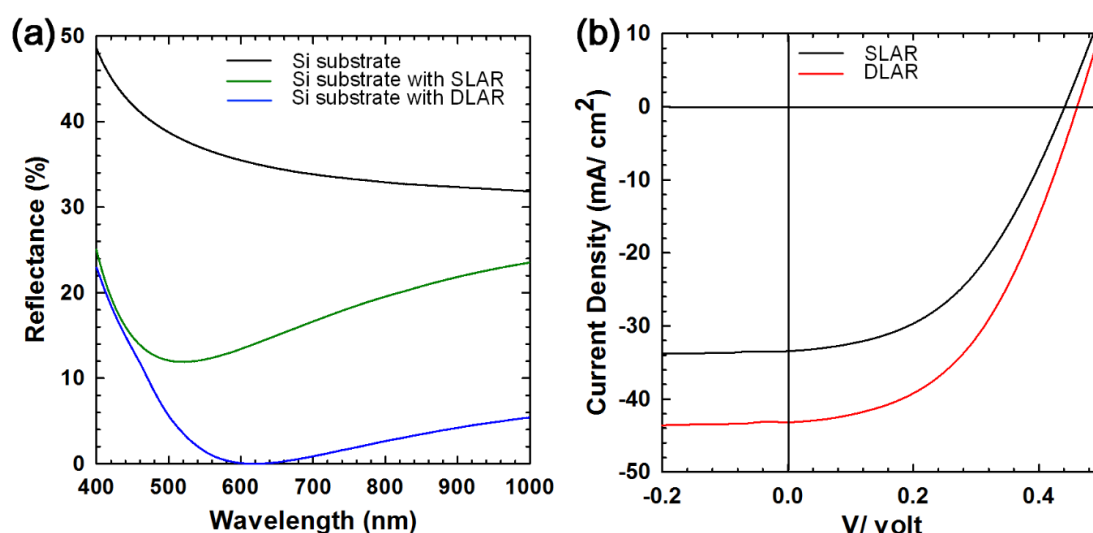


Figure 5-21: (a) Reflectance spectra of Si substrates with and without anti-reflective coatings. (b) J - V characteristics for the fabricated devices using Si substrates with antireflective coatings after formamide treatment for 30 min, annealing in forming gas for 2h and doping treatment of HNO₃ for 30 sec.

Table 5-4: Open-circuit voltage (V_{oc}), short-circuit current density (J_{sc}), fill factor (FF), and power conversion efficiency (PCE) of fabricated devices using Si substrates with and without anti-reflective coatings after formamide treatment for 30 min, annealing in forming gas for 2 h and doping process for 30 sec

Substrate	V_{oc} (mV)	J_{sc} (mA/ cm ²)	FF (%)	PCE (%)
Si	380	26	45	4.6
SLAR	422	33.5	47.4	7
DLAR	458	44	50	9.5

Marginally improved from 0.422 to 0.458 V as listed in Table 5.4. It is also clear from this table that the maximum efficiency of 9.5% was obtained by the final fabricated device. To the best of our understanding, the value of 9.5% is a new record for graphene/Si solar cell efficiency reported to date, and it is superior to devices fabricated without the top window structure [125].

5.4 Conclusion

The significance of a back-contact structure on the graphene/Si Schottky junction solar cell performance was presented. Increasing the active area of this device resulted in a further enhancement in solar cell efficiency in comparison with that of reported devices although the same area of graphene sheets was used to form a Schottky junction with Si substrates. To fabricate graphene/Si Schottky junction solar cells with the back-contact structure, two novel techniques for lithography and forming contacts were developed. Regarding the lithography process, DUV treatment was employed as post-baking to avoid the undesirable cross-link of the photoresist on graphene during the etching and sputtering processes. For forming contacts on graphene layers, an Au layer was sputtered at low power of 50 Watt after introducing an evaporated Cr layer, resulting in a significant

decrease in the contact resistance of the graphene/metal. It was also found that PMMA residue is the key to eliminate the distinctive s-shaped kink in measured J - V curves of graphene/Si Schottky junction solar cells. To solve this issue, formamide treatment was applied prior to the annealing process to minimize the effect of this residue and consequently to improve the solar cell performance. Thus, the PCE of 2.6% was obtained after reducing the PMMA residue. Additionally, the PCE of 9.5% was achieved after applying chemical doping and anti-reflection coating techniques. This novel device offers a feasible way to fabricate a high performance, stable and affordable graphene/Si Schottky junction solar cell.

6 Novel graphene/n-Si Schottky junction solar cells with a back-contact structure based on DUV treatment

6.1 Introduction

In the previous chapter, the PMMA residue was effectively eliminated using the formamide treatment before annealing samples. However, an annealing process has to be carried out in vacuum for few hours [17-20]. Moreover, the annealing process for long time affects the material component of plastic electronics which have graphene as a transparent conductive electrode [177, 182, 183]. Additionally, this process requires safety considerations to avoid an explosion caused by H₂ gas. In this chapter, it is reported a novel technique using deep UV treatment for 20 min in ambient air within the wet transfer process to remove the PMMA layer from the transferred graphene surface. This improves the properties of graphene, leading to the suppression of the recombination process due to this residue. Transferred graphene layers using this technique were systematically evaluated by an optical microscope, AFM, Raman spectroscopy, X-ray photoelectron spectroscopy and electrical measurements. Additionally, the hysteresis in I_D - V_G characteristics of back-gate gFETs, explained in section 3.3, is studied before and after introducing the DUV treatment. To reduce the recombination process of carriers at a graphene/Si interface because of dangling bonds (see section 3.4.1), a layer of SiO₂ is grown as a passivated layer onto Si substrates through exposing samples to ambient air for 2 hours after the cleaning process. Furthermore, the behaviour of J - V curves of graphene/Si junction solar cells is investigated under DUV treatment between 20 and 65 min. Unlike reported works in section 3.4.1, texturing process is successfully applied within the fabrication process of solar cells to reduce the reflected light from the front of

Si substrates and further improve the solar cell performance. The stability of doped devices with HNO₃ for 1 min is also examined.

6.2 Novel wet transfer process based on DUV treatment

Fig. 6.1 shows a schematic illustration of the novel process using DUV irradiation for transferring graphene layers onto desired substrates. It is clear from this figure that the introduction of DUV irradiation within the wet transfer process is the principle difference between the modified DUV transfer and transfer. As shown in Fig. 6.1e, after transferring PMMA/graphene layers onto desired substrates using the same procedure as in the previous chapter, both layers were exposed to the DUV irradiation of 254 nm at 180 °C for 20 min in air as shown in Fig. 6.1f and followed by acetone treatment. During the irradiation process, a DUV lamp was fixed at a distance of 10 cm from the sample.

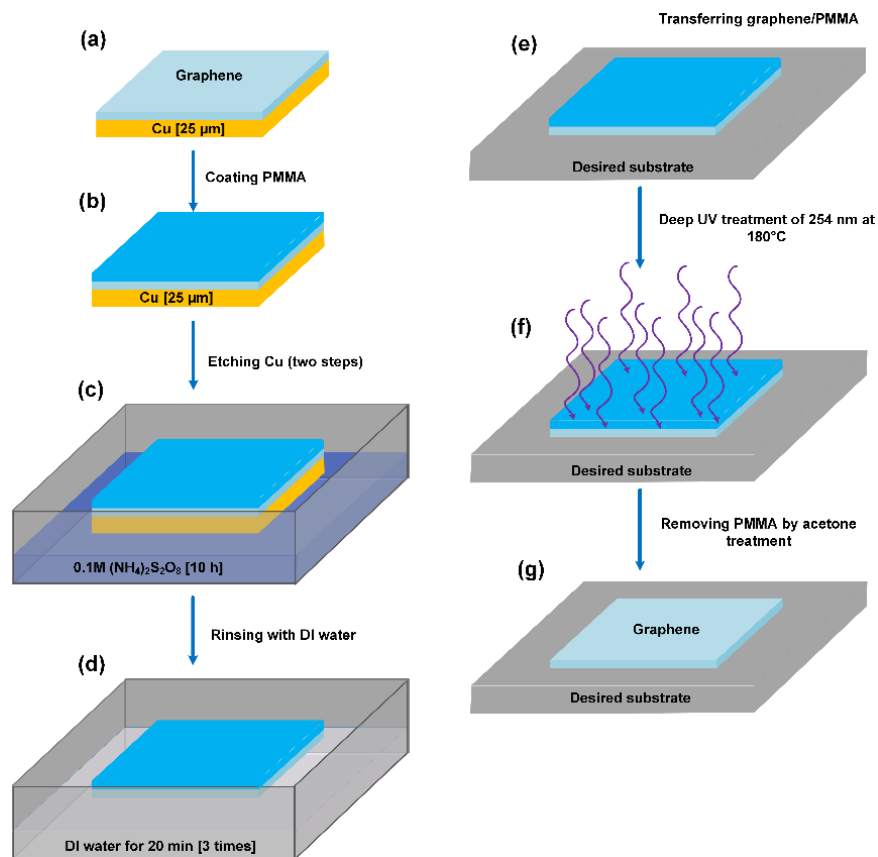


Figure 6-1: Schematic representation of the novel wet-transfer process, indicating the DUV irradiation treatment.

Usage of DUV irradiation in this case was to cleave the chemical bonds of PMMA. A temperature of 180 °C was applied in this treatment to reduce the time of cleaving process as DUV exposure of PMMA at room temperature requires several hours [184, 185].

6.2.1 Physical characteristics of transferred graphene using DUV treatment

The quality and monolayer nature of graphene layers transferred using the DUV treatment under optimized conditions were verified by an optical microscope and AFM. Fig. 6.2a shows a typical optical image of a 60×60 μm² area of transferred graphene with DUV treatment. It can be seen that the transferred graphene layer was almost uniform and continuous compared with that of graphene layers transferred without DUV (i.e. graphene transferred with acetone treatment as processed in section 5.2.1). Fig. 6.2b displays a noncontact AFM image of a 10.35×10.35 μm² area of the transferred graphene. It can be noticed that transferred graphene was almost clean and there are no spots of residual PMMA left on the graphene surface. This indicates that the surface of the graphene layer

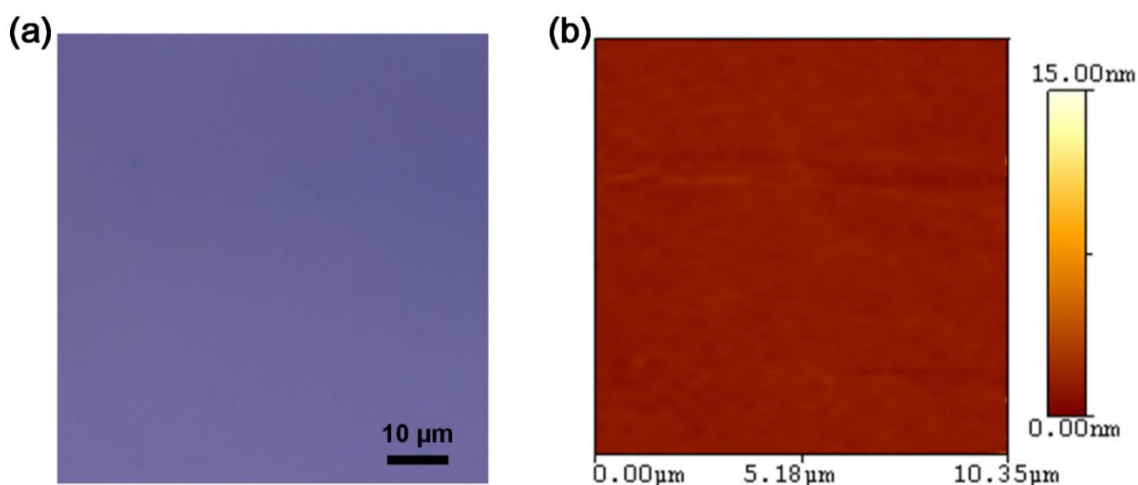


Figure 6-2: (a) and (b) Optical and AFM images of transferred graphene surfaces, which was treated with DUV irradiation, onto SiO₂/Si substrates, respectively.

is clean and smooth. Raman spectroscopy was also used to evaluate the crystallinity of transferred graphene as shown in Fig. 6.3a. The spectrum of transferred graphene is for monolayer, and the D band is not observed in this figure. It can also be seen that the G and 2D bands are at 1580 and 2699 cm^{-1} , respectively. This signifies that there was an important red shift in the spectrum of graphene treated with the DUV irradiation compared to that of graphene layers treated without DUV, indicating that transferred graphene has less PMMA residue. The intensity ratio of the 2D to G bands for transferred graphene by developed technique was around 2, whereas it was about 1.6 for graphene transferred without DUV method. The intensity ratio of 2 means that the graphene transferred using the improved technique is a higher quality monolayer than those of graphene transferred by previous methods. The amount of PMMA residue on the transferred graphene surface was extra examined using XPS. Fig. 6.3b shows the C 1s core-level spectra of the transferred graphene. As shown, the spectral components attributed to PMMA residue are remarkably reduced compared to

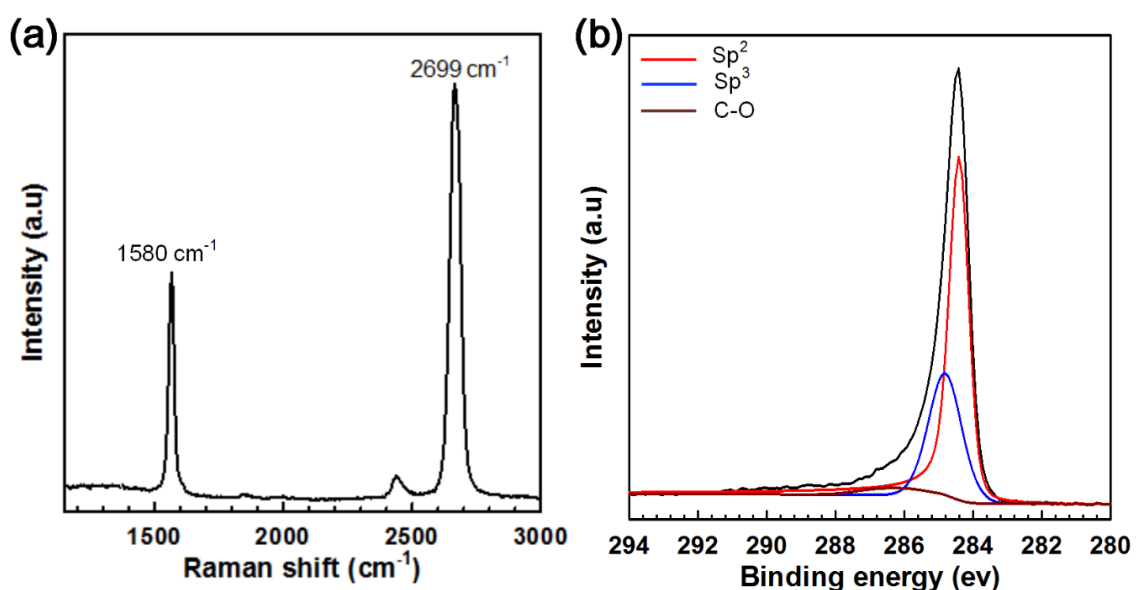


Figure 6-3: (a) and (b) Raman spectrum and XPS data of graphene transferred with DUV method onto SiO_2/Si substrates, respectively.

those of graphene treated without DUV. This verifies that PMMA residue on the graphene surface was effectively minimized by the DUV technique. Thus, the physical characteristics of transferred CVD-graphene show that applying the DUV for 20 min within the wet transfer process successfully vanishes the residual PMMA from graphene layers. This also indicates that the modified DUV transfer process is a faster, safer and easier method to reduce the PMMA residue on transferred graphene layers than the formamide method. Reduction of PMMA residue using the DUV technique attributes to the cleaving of the chemical bonds in PMMA by DUV exposure, where the cleaving process is in both the main chain and side groups of PMMA, thereby increasing the solubility of PMMA in acetone for subsequent processing steps.

6.2.2 Electrical characteristic of transferred graphene using DUV treatment

Four-probe measurement was applied to determine the sheet resistance of the transferred graphene onto SiO₂/Si substrates. The sheet resistance was in the range of 450±50 Ω□⁻¹ as shown in Table 6.1. It is clear that minimizing the PMMA residue on the graphene surface reduced the sheet resistance by about 60% more than that of untreated graphene with DUV. The contact resistance between graphene and electrode was extracted from Fig. 6.4, and it was around 118 Ω.

Table 6-1: Sheet and contact resistances of graphene layers transferred with and without DUV treatment

Transfer method	Sheet resistance (Ω□ ⁻¹)	Contact resistance (Ω)
Acetone	1150±50	600
DUV	450±50	118

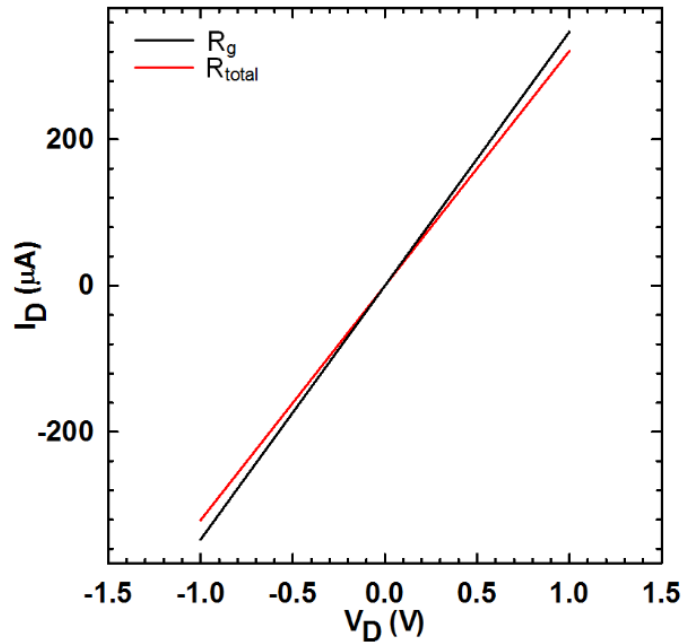


Figure 6-4: Current-voltage (I_D - V_D) output curves of the gFETs treated with DUV.

After minimizing the PMMA residue, it can be observed that the value of this resistance decreased by around 80% (see Table 6.1). Thus, electrical data confirms that reducing the PMMA residue improved the electrical conductivity of graphene and contact between the graphene and electrodes.

6.3 Hysteresis of graphene-based field effect transistors (gFETs)

In order to further investigate graphene layers before and after applying DUV irradiation, the hysteresis of gFETs was studied in the ambient environment. The gate voltage was continuously applied through the rear side of devices from -40 to 0 V, then to +40 V and back to -40 V. The source-drain bias (V_D) was constant at 10 mV for all measurements. Fig. 6.5 shows typical (I_D - V_G) transfer curves under forward and backward sweeps of devices treated with and without DUV. The magnitude of hysteresis in these devices can be explained in terms of the difference in the threshold voltages $\Delta V_{th} = V_{thb} - V_{thf}$ as shown in Table 6.2, where

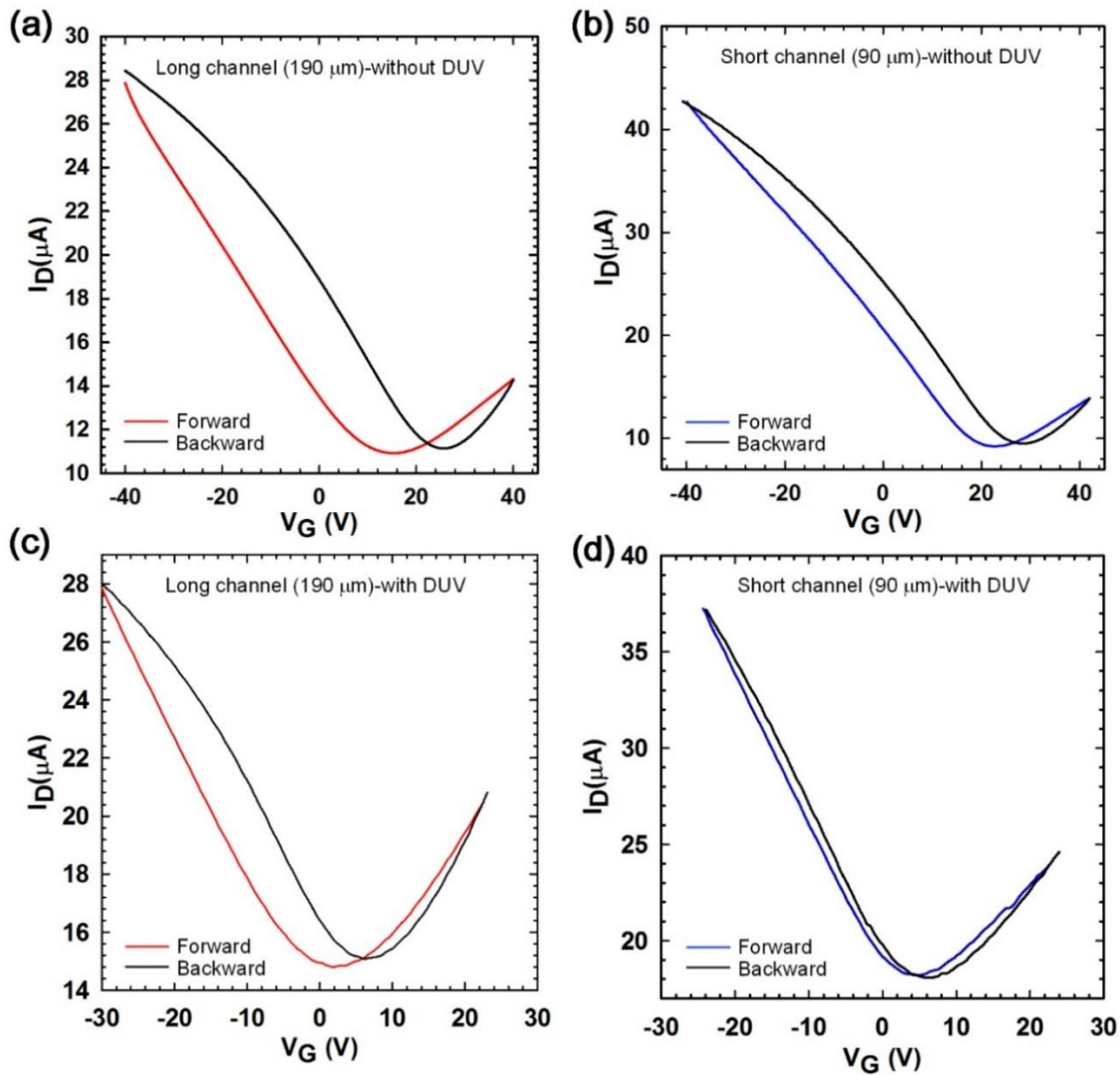


Figure 6-5: Current-voltage (I_D - V_G) transfer curves measured in air at room temperature and $V_D = 10$ mV under forward and backward sweeps. (a) and (b) Untreated long and short channel devices. (c) and (d) DUV treated long and short channel devices.

Table 6-2: Difference in the threshold voltages (ΔV_{th}) for long and short channel devices treated with and without DUV irradiation under both sweeps in air at room temperature and $V_D = 10$ mV

Channel(μm)	Acetone treatment			DUV treatment		
	ΔV_{th} (V)	V_{thb} (V)	V_{thf} (V)	ΔV_{th} (V)	V_{thb} (V)	V_{thf} (V)
90	8	29	21	1.2	3	1.8
190	15	24	9	6	4	-2

V_{thf} and V_{thb} are threshold voltages under forward and backward sweeps, respectively. The threshold voltages under both sweeps are obtained by extrapolating the linear region (ELR) method [186]. The ΔV_{th} was 15 V (24-9) and 8 V (29-21) for untreated long and short channel devices respectively, whereas the ΔV_{th} was 6 V (4+2) and 1.2 V (3-1.8) for treated long and short channel devices respectively. It is clear that the values of ΔV_{th} are reduced by 60 and 75% for treated long and short channel devices respectively, compared to those of untreated devices. This indicates that the number of trapped charges at the graphene/SiO₂ interface for treated devices was lower than that for untreated devices, resulting in a decrease in the hysteresis in the I_D - V_G characteristics of treated devices as shown in Figs. 6.5c and 6.5d, in contrast to the untreated devices (see Figs. 6.5a and 6.4b). It can be observed that the V_{np} of devices was reduced after applying the DUV, showing that the doping level in graphene was reduced. This further confirms that the DUV technique significantly reduced the PMMA residue on graphene layers. It can also be seen that Dirac points (neutral point voltages V_{nps}) of devices were positively shifted under the backward sweep, and this shift was due to the electrical screening effect, which originates from trapped charges at the graphene/SiO₂ interface [187]. Additionally, it can be noticed in this figure that the V_{np} for short channel devices was more positively shifted than that for long channel devices. This is attributable to short-channel effects in gFETs [188]. The effect of repeating the electrical test on the treated long and short channel devices was also investigated under different recovery times (1, 10, 20, 50, 100, 200 and 500 s). This effect is explainable in terms of shifted neutral point voltages under both sweeps as shown in Figs. 6.6a, 6.6b and Table 6.3. It can be seen that the V_{nps} for both irradiated devices shift with the recovery time under both sweeps. This points out that the trapped charges at

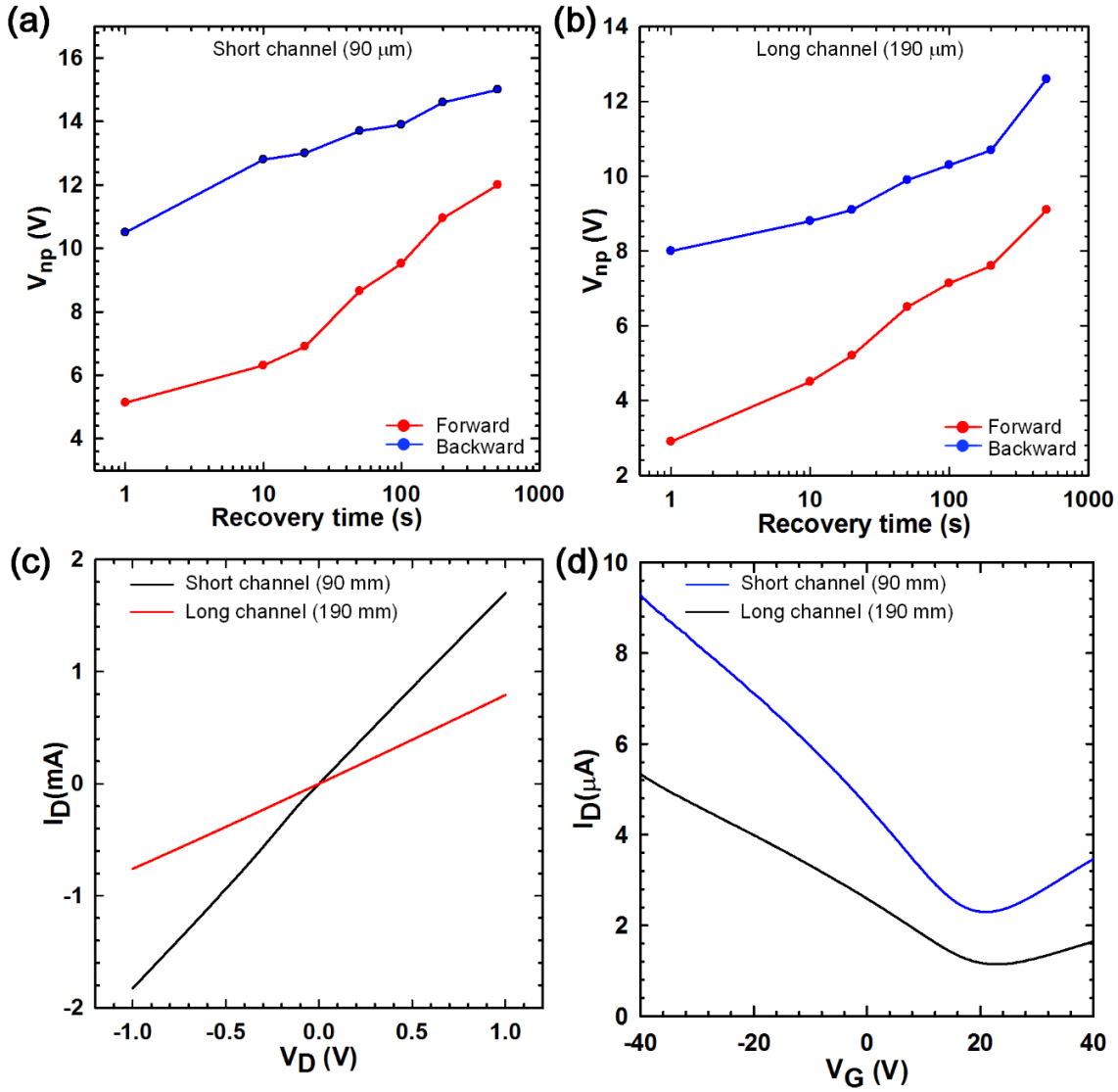


Figure 6-6: (a) and (b) Shifting of neutral point voltage of treated gFETs under repeating the electrical test at different recovery times in air at room temperature and $V_D = 10$ mV. (c) Current-voltage (I_D - V_D) output curves of treated gFETs in air at room temperature and $V_G = 5$ V. (d) Current-voltage (I_D - V_G) transfer curves of treated gFETs measured in air at room temperature and $V_D = 10$ mV after aging process.

the graphene/SiO₂ interface have not completely been released after each test, and these charges will continuously accumulate and increase the electrical field screening effect for the next test. This behaviour will eventually lead to a further increase in the shifting of V_{np} [189]. The values of the neutral point voltage differences ($\Delta V_{np} = V_{npb} - V_{npi}$) were reduced from 5 to 2.7 V for the short channel device and from 5.2 to 3.8 V for the long channel device after the recovery time of 500 s. This means that the number of trapped charges will be reduced;

Table 6-3: Shifting of neutral point voltage of treated devices under both sweeps and repeating the electrical test at different recovery times (1, 10, 20, 50, 100, 200 and 500 s) in air at room temperature and $V_D = 10$ mV

Recovery time (s)	Short channel		Long channel	
	V_{npf} (V)	V_{npb} (V)	V_{npf} (V)	V_{npb} (V)
1	5.1	10.5	2.9	8
10	6.3	12.8	4.5	8.8
20	6.9	13	5.2	9.1
50	8.6	13.7	6.5	9.9
100	9.5	13.9	7.1	10.3
200	10.9	14.6	7.6	10.7
500	12	15	9.1	12.6

increasing the recovery time due to the limitation of interface trap sites at the interface. In addition, these devices showed less shifting of neutral point voltages than those of reported devices [189]. This confirmed that the treated gFETs are more stable following repeated electrical measurements. The output characteristics of treated gFETs were also studied using the four-probe method in air at room temperature and V_G of 5 V as shown in Fig. 6.6c. It can be seen that there is a linear relationship in I_D - V_D curves for both devices, which suggests that there is an ohmic contact between the graphene and electrode. The calculated resistances in this figure were 0.56 and 1.18 K Ω for the short and long graphene channels, respectively. The effect of aging on the performance of treated gFETs was also studied in terms of shifting neutral point voltages under the forward sweep. In this case, devices were left in an ambient environment for

a month without applying voltage. Fig. 6.6d displays the transfer characteristics of treated devices in air at room temperature and $V_D = 10$ mV. As shown in this figure, there is a positively shift of the V_{np} after aging process, compared with those devices before the aging process (see Fig. 6.5c and 6.5d). It can be noticed that the V_{np} was shifted from 2 to 23 V for the long channel device and from 5.5 to 21 V for the second device after aging. It is clear that aging causes a shift in V_{np} and a decrease in the current (I_D). In addition, the V_{np} of the long gFET was slightly higher than that of the short gFET, which suggests that the long channel device is more effected by an ambient environment due to the larger area of this device.

6.4 Current density-voltage (J - V) characteristics of graphene/n-Si Schottky junction solar cells based on back-contact structure and DUV treatment

Fig. 6.7 shows a fabrication process of graphene/Si Schottky junction solar cell based on back-contact structure and DUV treatment. As shown in Fig. 6.7a, after the cleaning process of Si substrates, substrates were exposed to ambient air for 2 hours to achieve the passivation process of Si substrates [45, 127, 130]. Then, PMMA/graphene layers were transferred onto Si substrates, and the DUV treatment for 20 min was applied in order to effectively remove the PMMA layer as displayed in Fig. 6.7c. Then, the shaping process was introduced to obtain the optimum area of graphene sheets, followed by forming contacts. Fig. 6.8a shows the (J - V) characteristics of graphene/n-Si Schottky junction solar cells treated with and without DUV. It can be noticed that there is a s-shape in the J - V curve (black line) of a device based on the back-contact structure and acetone treatment. The J_{SC} , V_{OC} , FF and PCE of this device were 19.5 mA/cm², 0.415 V, 23% and 1.87%, respectively. It can be observed that the V_{OC} and J_{SC} improved

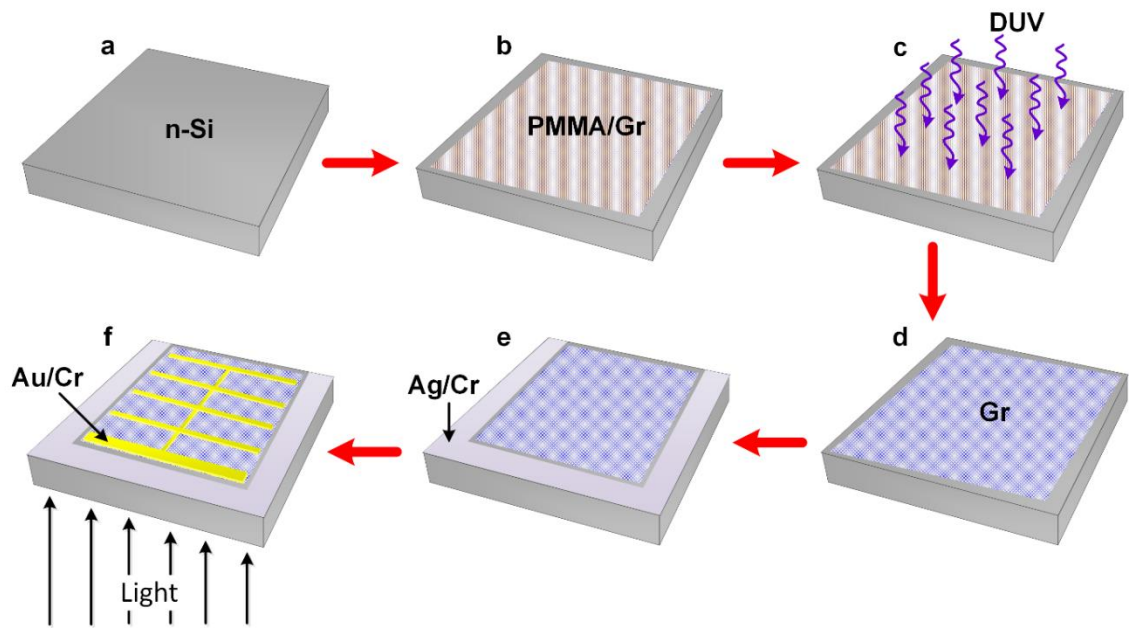


Figure 6-7: Fabrication process of graphene/Si Schottky junction solar cells. (a) Si substrate after cleaning process and leaving in air for passivation process for 2h. (b) Transferring PMMA/graphene (Gr) onto the center of Si substrate. (c) Exposing PMMA/Gr to the DUV of 254 nm at 180 °C. (d) Removing PMMA layer by acetone treatment. (e) Applying shaping process and creating Ag/Cr cathode. (f) Forming Au/Cr grid.

by around 40% and 100% respectively after exposing Si substrates to the ambient air, compared with those of the unexposed device displayed in section 5.2.3. This shows that the passivation process of dangling bonds at Si substrates significantly reduces the recombination process of generated carriers at the graphene/Si interface, resulting in an increase in the solar cell efficiency to nearly three times of that in the case of a un-passivated device. However, the s-shape is still in the J - V curve of the improved device. In contrast, as shown in Fig. 6.8a, there is a typical J - V curve (blue line) of a device based on the back-contact structure and DUV treatment for 20 min. The photovoltaic parameters for this device were 32.9 mA/cm², 0.41 V, 35% and 4.7%, respectively. This data shows that the V_{OC} of the sample is slightly decreased after DUV treatment, and this means that graphene becomes less p-doping. It can be observed that reduction of this residue also enhanced the J_{SC} , indicating that the trapping process for

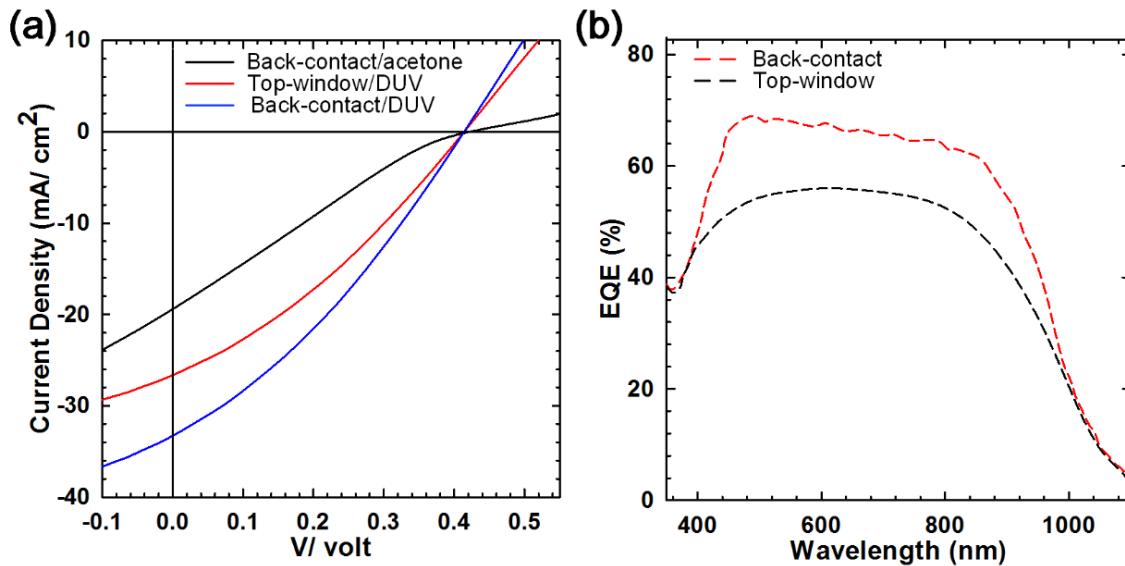


Figure 6-8: (a) J - V characteristics for the graphene/Si Schottky solar cells fabricated with top-window and back-contact structures. (b) External quantum efficiency (EQE) spectra of devices fabricated with both structures.

generated carriers was reduced. It is also clear that minimizing the PMMA residue eliminated the s-shape, resulting in an increase of the FF by 55% compared with that of the sample treated with acetone only. Hence, this additionally confirms that removing the PMMA residue is the key to eliminate the s-shape in J - V curves of graphene/n-Si Schottky junction solar cells. This also states that the elimination process of PMMA residue on graphene surface using the DUV irradiation is fastest, safest and simplest compared with those of reported methods in the previous chapter. To compare the performance of the device based on a back-contact structure, a device with an active area of 0.11 cm² was prepared using the top-window structure as shown in Fig. 6.9b. It can be observed that the active area of our device is increased by using the same area of the graphene sheet, compared with that of the device based on the top-window structure. This refers to that the number of photons absorbed is higher and leads to an increase in the solar cell efficiency as confirmed by the external quantum efficiency (EQE) data described later. Fig. 6.8a also compares the J - V curves of graphene/n-Si

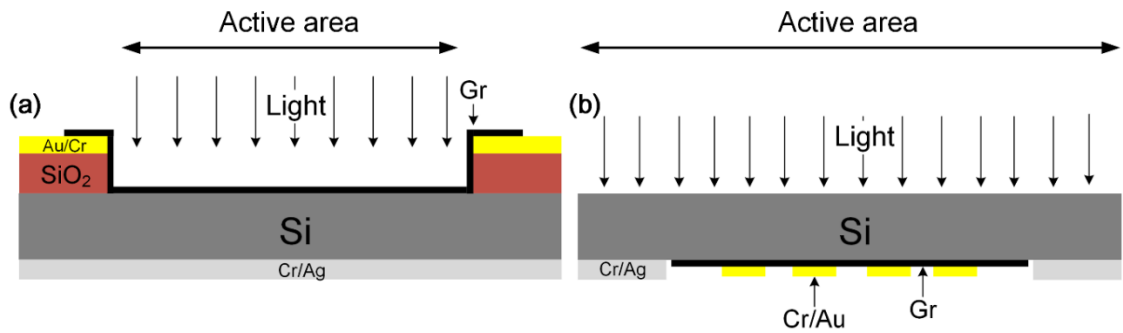


Figure 6-9: Schematic of graphene/Si Schottky junction solar cells fabricated with (a) top-window structure and (b) back-contact structure, showing an enhancement of the active area of the device based on the back-contact structure, showing that the same area of graphene sheet as a junction was used for both fabricated devices.

Schottky junction solar cells fabricated with both structures. The J_{SC} , V_{OC} , FF and PCE of the device fabricated with the top-window structure were 26.7 mA/cm^2 , 0.41 V , 31% and 3.4% , respectively. It is obvious that an increase in the active area of our device results in an improvement of the PCE by 40% , compared with that of the previous device. Hence, applying the back-contact structure within the fabrication process of graphene/Si solar cells is a smart idea to increase the active area of solar cell with using the area of graphene sheets. Fig. 6.8b shows EQE spectra of both devices. As shown, the EQE of the device fabricated with back-contact structure was about 65% in the wavelength range of $400\text{-}950 \text{ nm}$, whereas it was 53% for the device fabricated with top-window structure within the same range. It is clear that the EQE spectrum of our device shows a significant increase in the number of electron-hole pairs generated and collected after increasing the active area of device, in contrast to the device fabricated with the top-window structure. In addition, our device shows the highest EQE spectrum in comparison with those for reported pristine graphene/Si Schottky junction solar cells prepared with top-grid and top-window structures [100, 125]. Based on the EQE -setup method (see section 4.1.8), the calculated values of J_{SC} were 31.6 and 25.8 mA/cm^2 for devices fabricated with back-contact and top-window

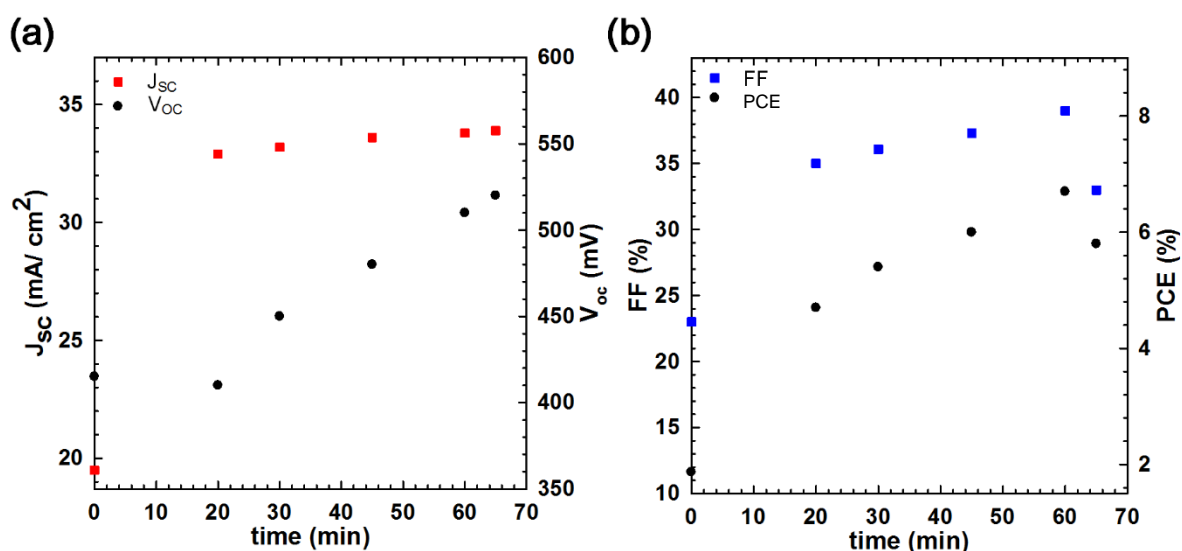


Figure 6-10: (a) and (b) Improvements of V_{oc} , J_{sc} , FF , and PCE of irradiated devices by DUV for different periods.

structures, respectively, which were in good agreement with those experimentally obtained from J - V curves in Fig. 6.8a. The effect of DUV treatment for longer periods (between 30 and 65 min) on the performance of this device was also systematically investigated. Average results of measured photovoltaic parameters for each exposed device are shown in Fig. 6.10 and Table 6.4. As observed in Fig. 6.10a, the V_{oc} and J_{sc} significantly increased to 0.51 V and 33.8

Table 6-4: Open-circuit voltage (V_{oc}), short-circuit current density (J_{sc}), fill factor (FF) and power conversion efficiency (PCE) of treated graphene/Si devices with DUV for different periods (average Values reported).

DUV exposure Time (min)	V_{oc} (mV)	J_{sc} (mA/ cm ²)	FF (%)	PCE (%)
0	415	19.5	23	1.87
20	410	32.9	35	4.7
30	450	33.2	36.1	5.4
45	480	33.6	37.3	6
60	510	33.8	39	6.7
65	520	33.9	33	5.8

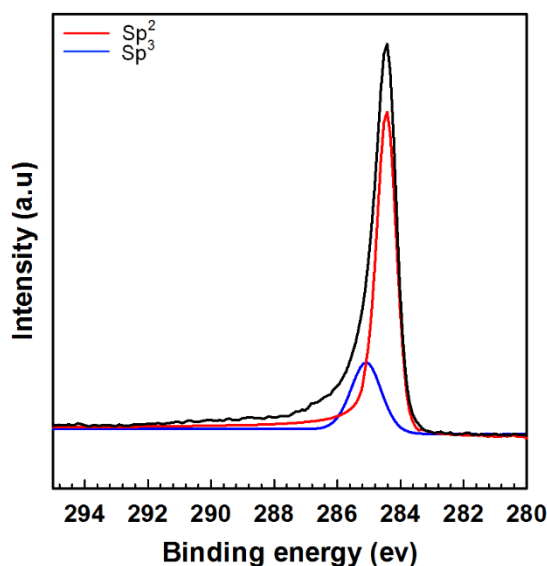


Figure 6-11: XPS data of graphene transferred with DUV method onto SiO_2/Si substrates, respectively.

mA/cm^2 , respectively after DUV exposure of PMMA/graphene for 60 min. These enhancements improved the FF to 39% and PCE to 6.7% as shown in Fig. 6.10b and Table 6.4. XPS and Raman spectroscopy were conducted to examine the reasons for this improvement in the solar cell efficiency. Fig. 6.11 shows the C 1s core-level spectra of graphene exposed to DUV irradiation for 60 min. It can be seen that the red peak (Sp^2) corresponds to graphene was further enhanced, showing a higher graphene quality, compared with that of graphene layers treated with DUV for 20 min. Additionally, the other peaks of C-O and C=O for the PMMA residue have efficiently been eliminated, unlike those of graphene layers exposed to the DUV for 20 min. This shows that the first reason for the development in photovoltaic parameters is that the PMMA residue on transferred graphene layers was further minimized by applying the DUV for a period of longer than 20 min. Raman data also shows that there is a significant blue shift in the spectrum of graphene sheet exposed to the DUV for 60 min, compared with that of a sample treated for 20 min as illustrated in Fig. 6.12. This points out that applying the DUV treatment for longer than 20 min enhances the p-doping level in graphene.

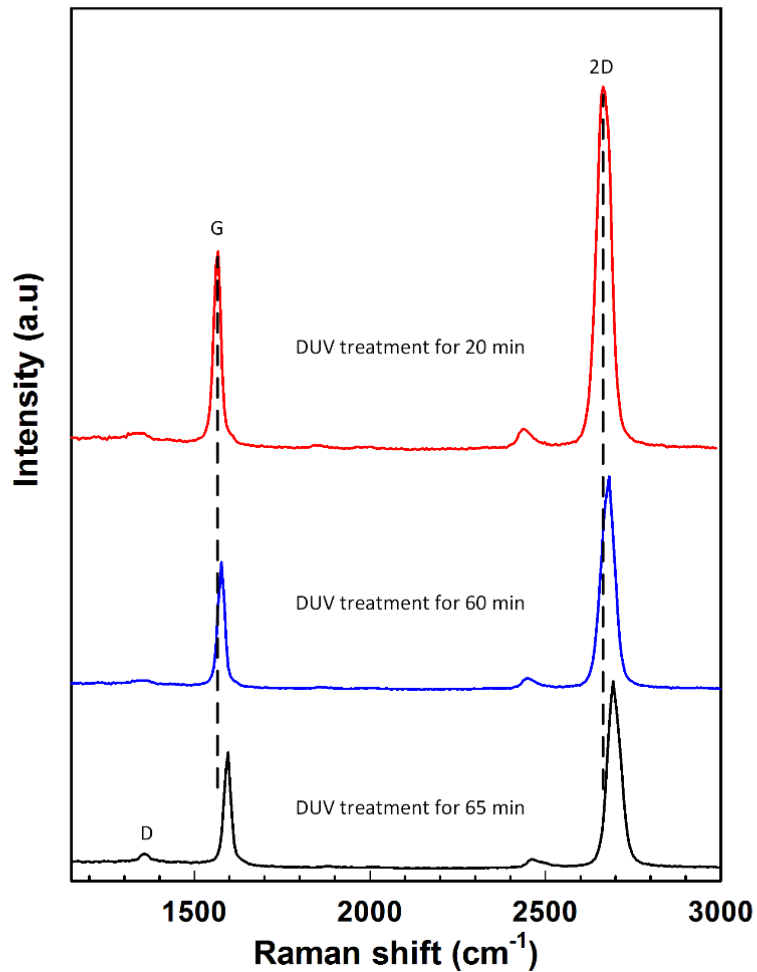


Figure 6-12: Raman spectra of transferred graphene onto SiO₂/Si substrates with DUV treatment between 20 and 65 min.

This also shows that the second reason for the improvement in solar cell performance is a result of the p-type doping effect obtained by the DUV in graphene when samples were exposed to the DUV for longer than 20 min. The I_{2D}/I_G peak intensity ratio of exposed graphene for 60 min was about 1.8, and it can be observed that there is no D band in the spectrum of exposed graphene. Thus, this refers to that the graphene layer treated with DUV for 60 min was still a high-quality monolayer. Hence, the Raman and XPS data show that the mechanism of the DUV treatment between 30 and 60 min is to further reduce the PMMA residue and enhance p-doping in graphene. This mechanism is the same of that of the forming gas, but the forming gas alone would not effectively remove

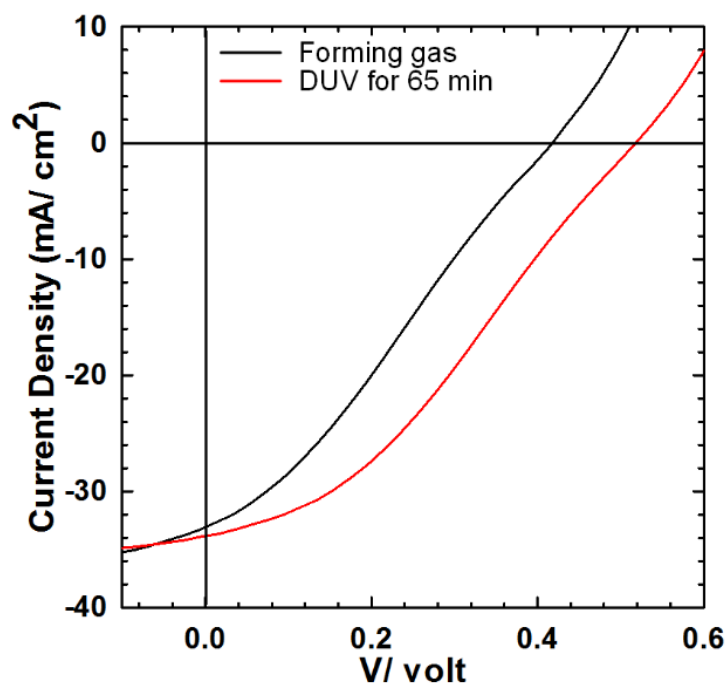


Figure 6-13: J-V characteristics of graphene/n-Si Schottky junction solar cells treated with forming gas at 300 °C for 120 min and DUV at 180 °C for 65 min.

the PMMA residue, unlike the DUV treatment. Furthermore, the p-doping obtained by DUV light is more effective than that obtained by forming gas method as the I_{2D}/I_G ratio of graphene will be around 1 after the annealing process. In addition, an annealing method has to be carried out in a vacuum for several hours, whereas the DUV treatment was applied in air for only 1h. This also confirms that applying the DUV between 30 and 60 min is more effective, faster, safer and easier to remove the PMMA residue than that by forming gas treatment alone. In addition, it enhances p-doping in graphene. To further improve the performance of devices, the DUV process was applied for the longer time than 60 min. The V_{OC} and J_{SC} slightly increased to 0.52 V and 33.9 mA/cm², respectively after treating PMMA/graphene devices for prolonged DUV exposure as shown in Fig. 6.10a and Table 6.4. However, the FF and PCE observably decreased to 33%

and 5.8%, respectively due to the s-shape in the J - V curve (red line) as shown in Fig. 6.13.

The XPS was also employed to explore the PMMA residue left on the treated graphene surface for 65 min. Fig. 6.14a shows the C 1s core-level spectra of the treated sample. As can be seen, the red peak (Sp^2) that corresponds to graphene displayed a greater reduction than that in the previous treatments, and peaks attributed to the PMMA residue clearly increased. This indicates that irradiation of PMMA/graphene sheets for a time longer than 60 min resulted in overbaking of the PMMA layer, and this was the cause of the PMMA residue on the graphene surface after acetone treatment, resulting in the s-shape in J - V curves of graphene/Si solar cells. Raman data also shows that there is the D band in the spectrum of graphene exposed for 65 min (see Fig. 6.12). This states that the transferred graphene with DUV for 65 min was not a high-quality monolayer. Hence, it is recommended that the DUV treatment should be applied between 20 and 60 min within the wet transfer process of CVD-graphene in order to remove the PMMA residue and to improve the performance of graphene devices.

The influence of annealing in forming gas (argon/hydrogen (9:1)) on the elimination of the s-shape was also studied. In this case, the percentage of hydrogen was increased to 10% in order to improve the removal the PMMA residue more efficiently than that achieved in the previous chapter. After transferring PMMA/graphene onto a Si substrate, the PMMA layer was removed by acetone. The sample was then annealed in forming gas at 300 °C for 2 h. Fig. 6.13 shows the J - V curve (black line) of an annealed device. The J_{SC} , V_{OC} , FF and PCE of this device were 33.1 mA/cm², 0.42 V, 29% and 4%, respectively. It can be observed that the J_{SC} , V_{OC} and PCE of this device were improved as a

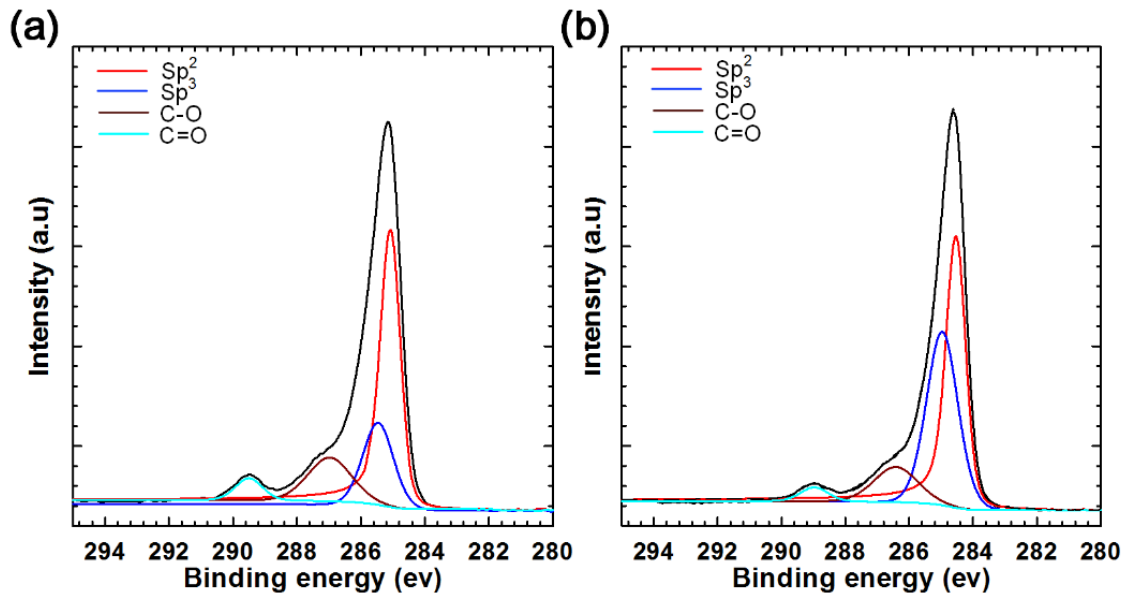


Figure 6-14: (a) and (b) XPS results of treated graphene on SiO₂/Si substrates with DUV at 180 °C for 65 min and forming gas at 300 °C for 120 min, respectively, the red peak corresponds to graphene, and the others indicate PMMA residue.

result of reducing the PMMA residue and increasing the doping in graphene, compared with that of the sample treated with acetone only. However, there is still the s-shape in the J - V curve of the annealed device, indicating that forming gas could not efficiently eliminate the s-shape in the J - V curve of graphene/Si Schottky junction solar cells although the percentage of forming gas mixture changed. XPS data also verifies that there was PMMA residue on the graphene annealed for 120 min as shown in Fig. 6.14b. This states that the forming gas (Ar/H₂ (9:1)) treatment was also unsuccessful in removing the PMMA residue, and this also confirmed in the reported work [107, 123]. This is a further confirmation that the removal of the PMMA residue is the answer to the issue of the elimination of the s-shape.

6.5 Current density-voltage (*J-V*) characteristics of graphene/n-textured Si Schottky junction solar cells based on back-contact structure and DUV treatment

Due to the novelty of graphene/n-Si Schottky junction solar cells based on back-contact structure, a texturing process was effectively involved within the fabrication process to reduce the reflected light from the front surface of Si substrates, leading to a further enhancement in the solar cell performance. In this case, the texturing process was only applied to the front surface of Si substrates, and graphene layers were placed on the non-textured side of Si substrates. This avoids the recombination process of carriers between the graphene and textured surface of Si substrates, which occurred in the reported work [131]. A wet texturing process using an alkaline solution was used to create pyramid-like structures on Si surfaces. As summarized in Table 6.5, four different KOH/IPA/DI H₂O solutions of 200 ml were prepared. The concentration of IPA varied from 4 to 10 Vol%, and the KOH concentration fixed at 1 W%. The temperature of 75 °C and texturing time of 45 min were fixed during the process. A spectrophotometer with an integrating sphere was used to characterize the reflectance of textured silicon substrates, and a non-textured substrate was used as a reference.

Table 6-5: Parameters of texturing processes for c-Si substrates processed using different KOH/IPA/DI H₂O solutions at 75 °C for 45 min.

Process	IPA (Vol%)	Average reflectance (%)
A	4	28
B	6	18
C	8	13
D	10	21

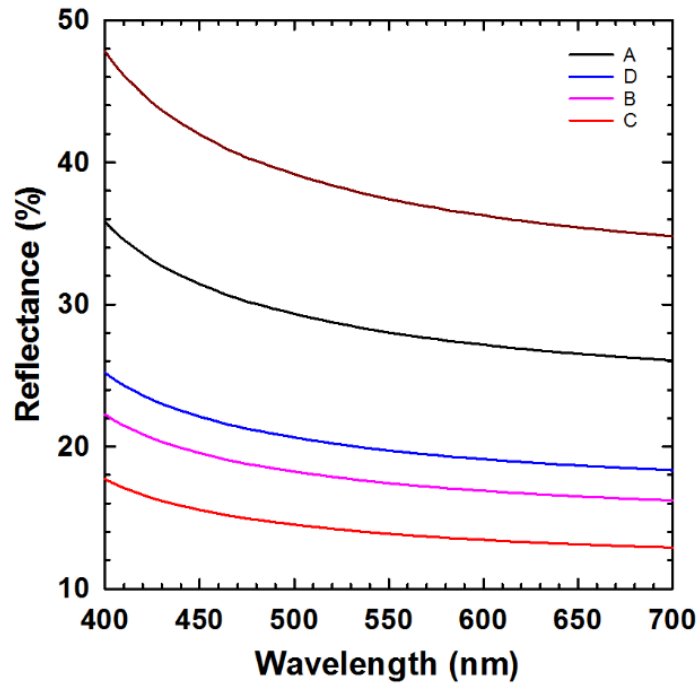


Figure 6-15: Reflectance spectra of textured Si substrates using different KOH/IPA/DI H₂O solutions at 75 °C for 45 min. A, B, C and D refer to processes displayed in Table 6-5.

As shown in Fig. 6.15, the diffused reflectance (R) of the textured substrates is a function of wavelength over the range of 400-700 nm. It can be seen that the average R of the non- textured Si (black curve) was 39%. After introducing the texturing process, the lowest average reflectance was about 13% for the textured substrate using a process labeled C as displayed in Table 6.5 and Fig. 6.15. The average height of the pyramid-like structures for textured substrates using the optimal process (process C) was measured using the AFM, and it was around 1 μm . The surface morphology of textured substrates was evaluated by the SEM. Fig. 6.16 shows SEM images of textured Si substrates using different KOH/IPA/DI H₂O solutions. For processes A, B and D, there were obvious variations in the textured surface of Si substrates as shown in Figs. 6.16a, 6.16b and 6.16d, resulting in significant differences in the reflectance of these substrates. However, the pyramid-like structures on these substrates are different in shape

and size. In contrast, the pyramid-like structures formed by the process C were almost uniform in shape and size over the whole substrate surface as shown in Fig. 6.16c. Hence, substrates textured by using the optimal process were used for solar cell fabrication. Fig. 6.17a displays the schematic of graphene/textured Si solar cells based on back-contact structure and DUV treatment. Fig. 6.17b shows the J - V characteristics of graphene/n-textured Si before and after applying chemical doping. As shown in this figure (black line) and Table 6.6, the values of J_{SC} , V_{OC} , FF and PCE for the graphene/n-textured Si device were 40 mA/cm², 0.51 V, 49% and 10%, respectively. This means that the PCE increased by 60% more than that of the device with a non-textured substrate. This improvement is attributable to a decrease in the reflectance of Si substrates using the texturing

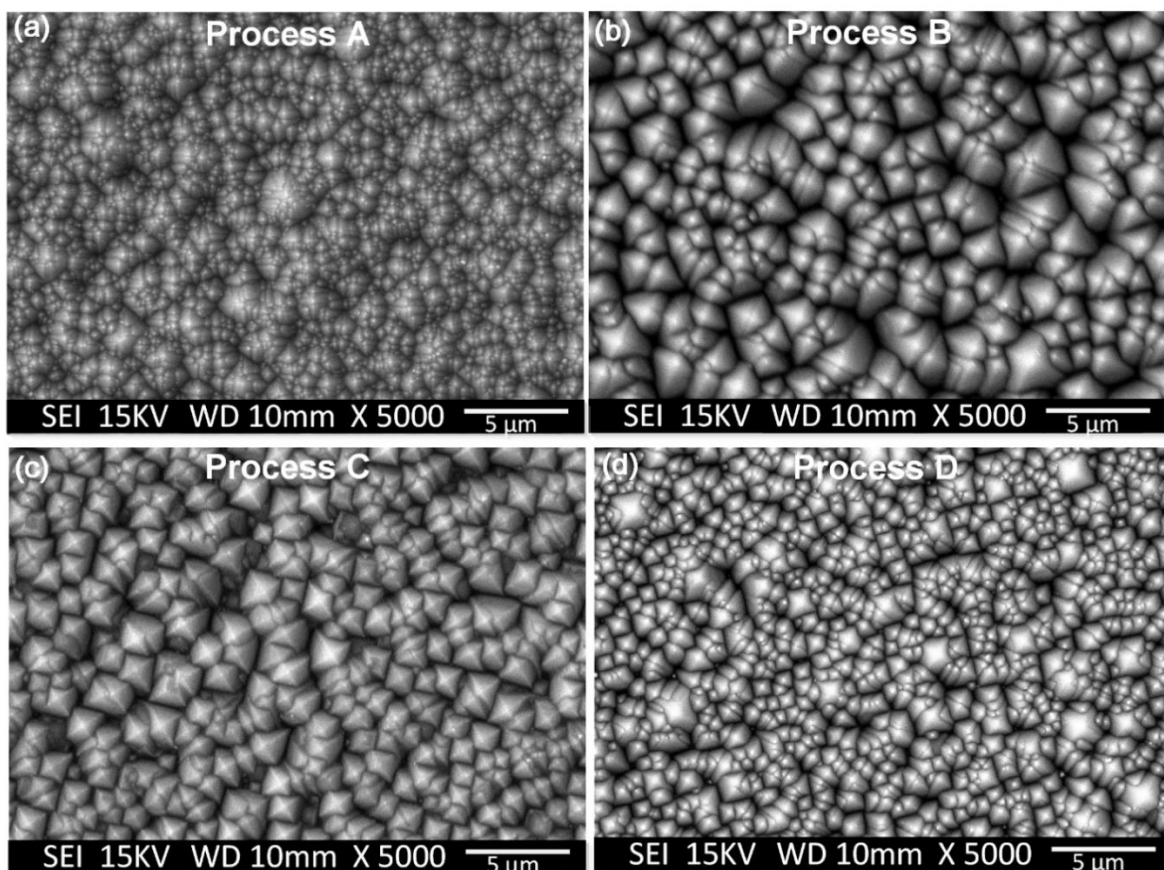


Figure 6-16: SEM images of textured Si substrates processed using different KOH/IPA/DI H₂O solutions at 75 °C for 45 min. A, B, C and D refer to processes displayed in Table 6-5.

process, leading to a significant increase in the J_{SC} . To the best of our understanding, the PCE of 10% establishes a new record to date for graphene/Si solar cells prepared without chemical doping and anti-reflection coating reported as illustrated in Table 6.7 [125, 127, 132, 190]. After treating the graphene sheet with 65% HNO_3 vapour for 60 s, the corresponding values of the photovoltaic parameters were 40.8 mA/cm^2 , 0.61 V , 57% and 14.1% as stated in Table 6.6. It is clear that the measured J - V curve (red line) of the doped device displayed a

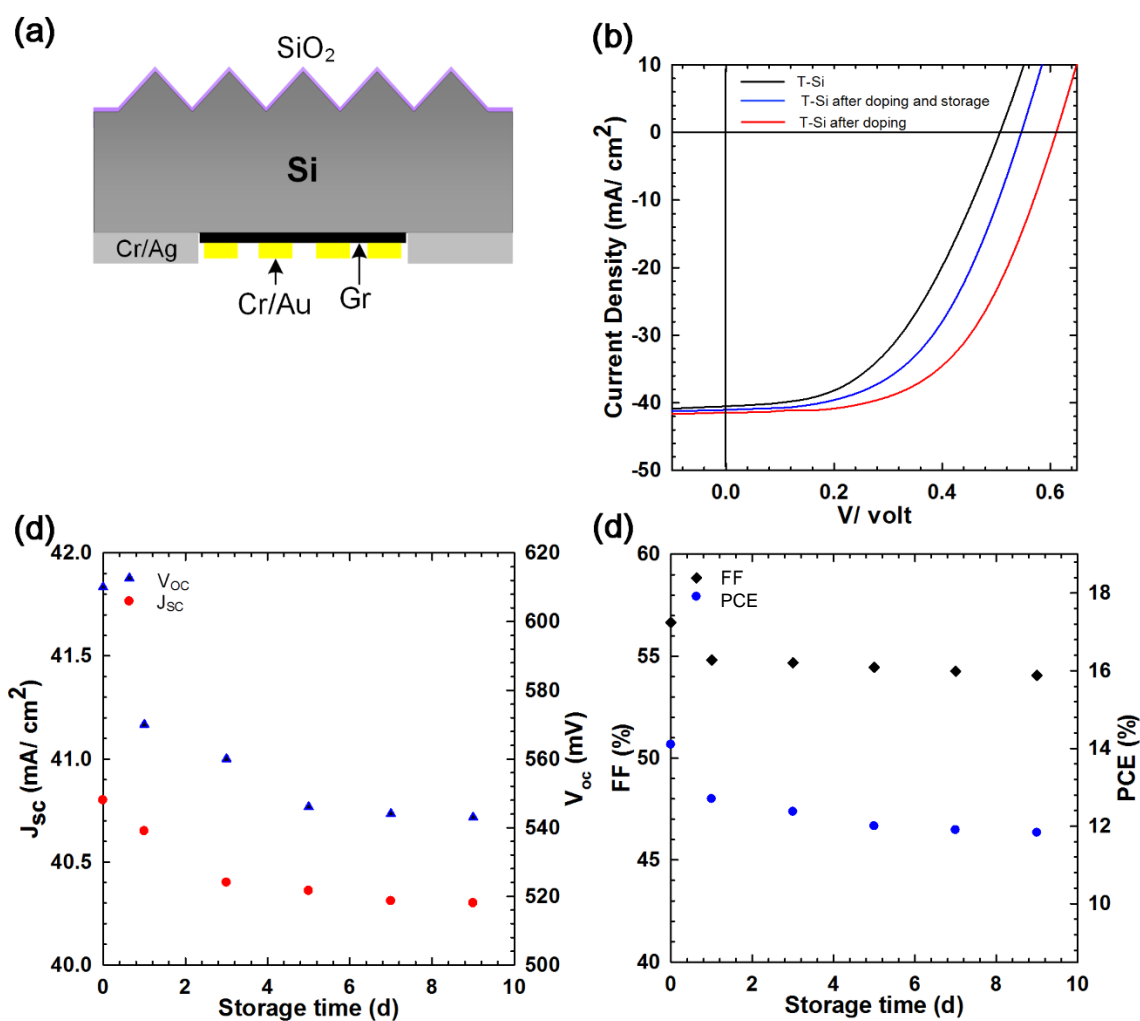


Figure 6-17: (a) Schematic of graphene/textured Si Schottky junction solar cell, indicating SiO_2 as the passivation layer. (b) J - V characteristics for graphene/textured Si devices before and after doping process of graphene/textured-Si Schottky. (c) and (d) Photovoltaic parameters of chemical doped graphene/Si Schottky junction solar cells during 9 days storage in air.

Table 6-6: Comparison of open-circuit voltage (V_{OC}), short-circuit current density (J_{SC}), fill factor (FF) and power conversion efficiency (PCE) of graphene/n-textured Si solar cells before and after doping process.

Device	V_{OC} (mV)	J_{SC} (mA/ cm ²)	FF (%)	PCE (%)
Graphene/textured Si	510	40	49	10
Doped-graphene/textured Si	610	40.8	56.65	14.1
Doped-graphene/textured Si after 9 days	543	40.3	54.06	11.83

noteworthy enhancement in photovoltaic performance compared to that of the previous device. The improvement in solar cell performance after the doping process was a result of the enhancements in the J_{SC} , V_{OC} and FF , unlike reported devices treated with HNO_3 [127, 133]. This attributes to the improved electrical conductivity of graphene after the reduction of the PMMA residue and the chemical doping process [117, 173]. To study the stability of the chemical doped devices, samples were kept in ambient conditions for 9 days. The measurement of J - V curves was repeated during that time. The average results of measured photovoltaic parameters after 9 days are presented in Figs. 6.17c, 6.17d and Table 6.8. It can be noticed that the drop in the performance of treated devices is mainly due to the decrease in the V_{OC} . The reason for this is that the chemical dopants gradually evaporated during this time [141, 174]. It is also clear from Fig. 6.17b that the J - V curve (blue line) of the doped device was still without the s-shape after 9 days, and the PCE of this device was 11.83%. This means that the device retains 84% of the efficiency after storage. This indicates that our devices showed more stability than those treated with HNO_3 in the reported work [141]. Thus, removal of the PMMA residue on graphene surfaces is vital for the stability

of chemically doped graphene/Si Schottky junction solar cells. Additionally, the doping level of the graphene layer decreases with time due to evaporation and the overall efficiency of the cell is reduced.

Table 6-7: The highest power conversion efficiency (*PCE*) reported to date for SGL/n-Si Schottky junction solar cells prepared without chemical doping and anti-reflection coating.

<i>PCE</i> (%)	Year	Reference
6.18	2014	[132]
7.04	2017	[190]
10	2017	This work

Table 6-8: Open-circuit voltage (V_{OC}), short-circuit current density (J_{SC}), fill factor (*FF*) and power conversion efficiency (*PCE*) of doped graphene/Si devices during 9 days storage in air (average Values reported).

Storage time (d)	V_{OC} (mV)	J_{SC} (mA/ cm ²)	<i>FF</i> (%)	<i>PCE</i> (%)
0	610	40.8	56.65	14.1
1	570	40.65	54.81	12.7
3	560	40.4	54.68	12.4
5	546	40.36	54.45	12
7	544	40.31	54.27	11.9
9	543	40.3	54.06	11.83

6.6 Conclusions

Reduction of polymer residue is a key challenge in the fabrication of graphene-based devices. In this chapter, the novel technique using deep UV (DUV) exposure of PMMA coated graphene samples was introduced to reduce the effect of PMMA residue. It was confirmed that applying the DUV irradiation resulted in a clean, uniform and continuous graphene sheets with a typical low sheet resistance. In addition, the contact between graphene and electrodes was improved following DUV exposure. Similarly, it was shown that the hysteresis behaviour in back-gate graphene field-effect transistors was minimized by reducing the PMMA residue. Furthermore, the treated devices showed more stability than untreated devices under repeated electrical tests during the recovery times. Moreover, devices aged for a month exhibited an increase in the shift of the neutral point voltage of treated devices. This development attributed to the cleaving of the chemical bonds in PMMA by DUV exposure, thereby increasing the solubility of PMMA in acetone. The role of a back-contact structure on the graphene/Si Schottky junction solar cell efficiency was also demonstrated. With this structure, the short-circuit current density improved by around 25% more than that of the device fabricated with the top-window structure. It was also confirmed that PMMA residue is the key to eliminate the s-shaped kink in J - V curves of graphene/Si Schottky junction solar cells. This shape was successfully eliminated by using the DUV treatment in air for 20 min. Additionally, applying the DUV treatment for 60 min further reduced the PMMA residue and enhanced the p-doping in graphene, leading to a further improvement in the solar cell's efficiency. The issue of recombination loss for charge carriers at the graphene/textured Si interface was also prevented by using this structure. After applying the texturing process and chemical doping, the power conversion

efficiency of 14.1% was obtained for graphene/Si Schottky junction solar cell. This device also showed great stability after 9 days storage, and it retained about 84% of its efficiency. This work presents a feasible way to prepare low-cost, stable and high-performance graphene/Si Schottky junction solar cells.

7 Conclusions and Further Work

7.1 Summary of Key results

This research introduced a new structure of graphene/Si Schottky junction solar cells. To prepare solar cells with low cost and high efficiency, many novel techniques for lithography, a shaping process and forming contacts were applied. With back-structure, the challenges of reported structures were overcome, where the same of the reported optimum area of graphene sheet was used to form Schottky junction with a Si substrate. The active area of this device is 0.19 cm^2 , and it is the largest area of graphene/Si Schottky junction solar cells with ideal J - V curves reported so far. Thus, J_{SC} has improved by around 25% compared with that of devices fabricated with the top-window structure. The physical properties of resultant transferred graphene were confirmed using Raman spectroscopy and optical contrast imaging. AFM was also employed to evaluate the morphology of graphene and the thickness of coated metals. To further investigate the PMMA residue left on graphene, XPS was used. Under the optimum conditions of the shaping process and forming contacts, the gFETs were prepared, and this enabled the electrical properties of transferred graphene to be studied. The physical and electrical data shown that there is PMMA residue left on graphene layers after acetone treatment as this treatment can not effectively remove the PMMA layer from graphene. This residue increased the sheet and contact resistances, resulting in a degradation in the performance of graphene-based devices. It also caused the s-shape in the of J - V curves of graphene/Si junction solar cells. An annealing process in forming gas was employed to reduce the PMMA residue and s-shape. However, the physical and electrical results showed that this treatment could only reduce this residue marginally. Thus, reducing the

PMMA residue is the key to eliminate the s-shape behaviour. To reduce this residue on graphene layers, two novel techniques were introduced. The first technique is by using the formamide before the annealing process. The physical and electrical data showed that the immersion graphene layers in formamide for 30 min resulted in a successful reduction of the PMMA residue. This also improved the sheet resistance and contact between the metal and graphene and eliminated the s-shape, leading to an enhancement in solar cell efficiency. This improvement is attributed to that the NH_2 functional group in formamide which was absorbed by the PMMA residue. This resulted in an electron donation to graphene at the graphene/PMMA residue interface, leading to a reduction in the amount of the PMMA residue. Then, the annealing process further removed PMMA residue. This effectively restored the intrinsic electrical properties of transferred graphene layers. After the doping process, samples showed higher J_{sc} , V_{oc} and FF . Including anti-reflection coating in the fabrication process decreased light reflected from Si substrates, resulting in a significant enhancement in solar cell performance.

The second novel technique is by using the DUV treatment. It was shown that exposing the PMMA/graphene layers to the DUV for 20 min efficiently removed the PMMA layer from graphene after acetone treatment. This means that the modified DUV transfer process was a faster, safer and easier method to reduce the PMMA residue on transferred graphene layers, compared to the previous method. The magnitude of hysteresis in the current-voltage (I_D - V_G) transfer curves of gFETs was reduced after DUV irradiation. The Dirac point of exposed graphene was also shifted toward a zero voltage, showing that the p-doped level obtained from PMMA residue in graphene was reduced. Reduction of PMMA residue using the DUV technique attributed to the cleaving of the chemical bonds

in PMMA by DUV exposure, and hence increasing the solubility of PMMA in acetone for subsequent processing steps. The effect of DUV treatment between 20 and 60 min on the performance of solar cells was studied. It was observed that the s-shape behaviour of irradiated devices for 20 min was successfully eliminated. Additionally, the PMMA residue was further reduced and the p doping in graphene was increased after applying the DUV treatment between 30 and 60 min, resulting in an additional enhancement in solar cell efficiency. This mechanism was the same of that of the forming gas, but the forming gas would not effectively remove the PMMA residue alone. This also confirmed that an irradiation process between 30 and 60 min was more effective, faster, safer and easier to remove the PMMA residue and enhance p-doping in graphene, in comparison with that of forming gas treatment alone. Due to the novelty of the back-contact structure, a texturing process was shown to be an effective part of the fabrication process to reduce light reflected from the front surface of Si substrates, leading to a further enhancement in the solar cell performance. In this case, the texturing process was only applied to the front surface of Si substrates, and graphene layers are placed on the non-textured side of Si substrates. This avoids the recombination process of carriers between the graphene and textured surface of Si substrates. Thus, the recorded power conversion efficiency of 10% was achieved for graphene/textured Si devices. After treating graphene/textured Si graphene/Si junction solar cells with HNO₃, the efficiency improved to 14.1%. Doped devices also showed great stability and retained 84% of the efficiency after 9 days storage in air. It can be concluded the contributions to the knowledge which have been achieved in this project as follows:

- Novel back-contact device structure with no optical loss due to contact was fabricated.

- Texturing process is successfully applied within the fabrication process of graphene/Si Schottky junction solar cells.
- Two techniques developed; for lithography and forming Au contacts on evaporated Cr.
- Identification of PMMA residue removal to be the Key to the elimination of the s-shape in J-V curves.
- Two novel techniques for wet transfer process introduced for PMMA residue removal.
- Novel DUV treatment for up to 60 min to eliminate the PMMA residue and increase the doping level in graphene at the same time.

7.2 Future work

In this thesis, a monolayer graphene was used in the fabrication process of graphene/n-Si Schottky junction solar cells. To further improve the efficiency of prepared devices, multi- layers of graphene are required. In this case, multi-graphene layers form a Schottky junction with a Si substrate, resulting in a further increase in the J_{sc} since the usage of multi- graphene layers improves a charge transport. Hence, the shaping process should be optimized to pattern the multi-graphene layers with an optimum area of 0.11 cm². Texturing process and anti-reflection coatings can also be introduced to the multi-graphene/n-Si Schottky junction solar cells. Thus, the work in chapters 5 and 6 can be investigated by using the multi-graphene layers. Hence, the photovoltaic parameters of prepared devices can be compared with those of the HIT solar cells discussed in section 2.4.1.1.4.

Additionally, graphene/p-Si Schottky junction solar cells can also be prepared. However, there are two challenges in that. The first challenge is the difficulty in

obtaining n-type graphene, and the second challenge is the PMMA residue which provides a negative p doping in graphene as shown in chapter 5 and 6 and. These are the main reasons for a low efficiency of graphene/p-Si Schottky junction solar cells. For the first challenge, it is already overcome by the novel techniques using formamide and DUV treatments. Thus, preparing n-type graphene is a great challenge for researchers. This has been already started in this research by using a formamide treatment for 35 min (see section 5.3.2). However, the effect of formamide treatment for a longer time on transferred graphene should be investigated to optimise n-graphene layers. The anti-reflection coatings and texturing process can also be added to further increase the solar cell efficiency of n-graphene/textured p-Si Schottky junction solar cells by reducing the reflected light from Si substrates.

In this research, crystalline Si substrates were used in the fabrication process of graphene/n-Si Schottky junction solar cells. Thus, doped amorphous Si layers instead of crystalline Si substrates can be used to prepare graphene/n-Si and graphene/p-Si Schottky junction solar cells, resulting in a decrease in the fabrication cost. This idea will also support to prepare flexible graphene/Si Schottky junction solar cells.

The Formamide and DUV techniques can also be employed to prepare Heterojunction intrinsic thin-layer (HIT) solar cells (see section 2.4.1.4). In this case, a p-type type amorphous Si layer is replaced by p-graphene which was achieved by DUV treatment for 60 min, and an n-type amorphous Si layer is exchanged by n-graphene which will be optimized using the formamide. Additionally, multi-graphene layers will be introduced in the fabrication process of HIT solar cells, resulting in a further increase in the solar cell efficiency. To further enhance the solar cell performance, HNO_3 is used for doping process.

References:

1. Ye, Y., et al., *Schottky junction photovoltaic devices based on CdS single nanobelts*. *Nanotechnology*, 2009. **20**(37): p. 375202.
2. Zhou, Z., et al., *Schottky solar cells with amorphous carbon nitride thin films prepared by ion beam sputtering technique*. *Solar energy materials and solar cells*, 2002. **70**(4): p. 487-493.
3. Luther, J.M., et al., *Schottky solar cells based on colloidal nanocrystal films*. *Nano letters*, 2008. **8**(10): p. 3488-3492.
4. Sun, Y., Q. Wu, and G. Shi, *Graphene based new energy materials*. *Energy & Environmental Science*, 2011. **4**(4): p. 1113-1132.
5. Ye, Y. and L. Dai, *Graphene-based Schottky junction solar cells*. *Journal of Materials Chemistry*, 2012. **22**(46): p. 24224-24229.
6. Novoselov, K.S., et al., *Electric field effect in atomically thin carbon films*. *science*, 2004. **306**(5696): p. 666-669.
7. Novoselov, K.S., et al., *A roadmap for graphene*. *nature*, 2012. **490**(7419): p. 192-200.
8. Goetzberger, A. and V.U. Hoffmann, *Photovoltaic solar energy generation*. Vol. 112. 2005: Springer Science & Business Media.
9. Sze, S.M. and K.K. Ng, *Physics of semiconductor devices*. 2006: John wiley & sons.
10. Nelson, J., *The physics of solar cells*. 2003: World Scientific Publishing Co Inc.
11. Shockley, W. and W. Read Jr, *Statistics of the recombinations of holes and electrons*. *Physical review*, 1952. **87**(5): p. 835.
12. Green, M.A., *Solar cells: operating principles, technology, and system applications*. 1982.
13. Soga, T., *Nanostructured materials for solar energy conversion*. 2006: Elsevier.
14. Luque, A. and S. Hegedus, *Handbook of photovoltaic science and engineering*. 2011: John Wiley & Sons.
15. Jäger, K., et al., *Solar energy fundamentals, technology and systems*. Delft University of technology, 2014. **77**: p. 78.
16. Meemongkolkiat, V., *Development of high efficiency monocrystalline silicon solar cells through improved optical and electrical confinement*. 2008: Georgia Institute of Technology.
17. McDonald, D. and A. Cuevas, *Reduced fill factors in multicrystalline silicon solar cells due to injection-level dependent bulk recombination lifetimes*. 2000.
18. McIntosh, K.R., *Lumps, humps and bumps: Three detrimental effects in the current-voltage curve of silicon solar cells*. 2001: University of New South Wales.
19. Schlangenotto, H., H. Maeder, and W. Gerlach, *Temperature dependence of the radiative recombination coefficient in silicon*. *physica status solidi (a)*, 1974. **21**(1): p. 357-367.
20. Dzierwior, J. and W. Schmid, *Auger coefficients for highly doped and highly excited silicon*. *Applied Physics Letters*, 1977. **31**(5): p. 346-348.
21. Sinton, R.A. and R.M. Swanson, *Recombination in highly injected silicon*. *Electron Devices, IEEE Transactions on*, 1987. **34**(6): p. 1380-1389.
22. Altermatt, P.P., et al., *Assessment and parameterisation of Coulomb-enhanced Auger recombination coefficients in lowly injected crystalline silicon*. *Journal of Applied Physics*, 1997. **82**(10): p. 4938-4944.
23. Hall, R.N., *Electron-hole recombination in germanium*. *Physical Review*, 1952. **87**(2): p. 387.
24. Taguchi, M., et al., *HITTM cells—high-efficiency crystalline Si cells with novel structure*. *Progress in Photovoltaics*, 2000. **8**(5): p. 503-514.

25. Ali, K., S.A. Khan, and M.M. Jafri, *Enhancement of silicon solar cell efficiency by using back surface field in comparison of different antireflective coatings*. Solar Energy, 2014. **101**: p. 1-7.
26. Macleod, H. and T.-F.O. Filters, *Macmillan Publishing Company*. New York, 1986.
27. Birmann, K., M. Zimmer, and J. Rentsch, *Fast alkaline etching of monocrystalline wafers in KOH/CHX*. 23rd European PVSEC, 2008.
28. Chu, A., et al., *A simple and cost-effective approach for fabricating pyramids on crystalline silicon wafers*. Solar Energy Materials and Solar Cells, 2009. **93**(8): p. 1276-1280.
29. King, D.L. and M.E. Buck. *Experimental optimization of an anisotropic etching process for random texturization of silicon solar cells*. in *Photovoltaic Specialists Conference, 1991., Conference Record of the Twenty Second IEEE*. 1991. IEEE.
30. Green, M.A., *The path to 25% silicon solar cell efficiency: History of silicon cell evolution*. Progress in Photovoltaics: Research and Applications, 2009. **17**(3): p. 183-189.
31. Palik, E.D., *Gallium Arsenide (GaAs)*. Handbook of optical constants of solids, 1985. **1**: p. 429-443.
32. Masuko, K., et al., *Achievement of more than 25% conversion efficiency with crystalline silicon heterojunction solar cell*. IEEE Journal of Photovoltaics, 2014. **4**(6): p. 1433-1435.
33. Schroder, D.K., N.R. Thomas, and J.C. Swartz, *Free carrier absorption in silicon*. Solid-State Circuits, IEEE Journal of, 1978. **13**(1): p. 180-187.
34. Yablonovitch, E., *Statistical ray optics*. JOSA, 1982. **72**(7): p. 899-907.
35. Yablonovitch, E. and G.D. Cody, *Intensity enhancement in textured optical sheets for solar cells*. Electron Devices, IEEE Transactions on, 1982. **29**(2): p. 300-305.
36. Goetzberger, A. *Optical confinement in thin Si-solar cells by diffuse back reflectors*. in *15th Photovoltaic Specialists Conference*. 1981.
37. Riazimehr, S., et al., *High Photocurrent in Gated Graphene-Silicon Hybrid Photodiodes*. ACS Photonics, 2017.
38. Li, X., et al., *Graphene-on-silicon Schottky junction solar cells*. Advanced Materials, 2010. **22**(25): p. 2743-2748.
39. M. Green, K.E., D.L. King, Slgari, W. Warta, *Progress in Photovoltaics, Research and Applications*. Research and Applications, 2005. **1349e1354**
40. Kray, D., et al. *Comprehensive experimental study on the performance of very thin laser-fired high-efficiency solar cells*. in *Proceedings of the 19th European Photovoltaic Solar Energy Conference*. 2004. WIP Renewable Energies Paris, France.
41. Ralph, E.L., Proceedings of 11th IEEE Photovoltaics Specialist Conference, 1975: p. 315.
42. Wronski, C.R. and D.E. Carlson, *Amorphous silicon solar cells*. Vol. 199. 2001: Imperial College Press, London, UK.
43. Miles, R., K. Hynes, and I. Forbes, *Photovoltaic solar cells: An overview of state-of-the-art cell development and environmental issues*. Progress in Crystal Growth and Characterization of Materials, 2005. **51**(1-3): p. 1-42.
44. Staebler, D. and C. Wronski, *Reversible conductivity changes in discharge-produced amorphous Si*. Applied Physics Letters, 1977. **31**(4): p. 292-294.
45. Wu, B.-S., et al. *Hybrid multi-layer graphene/Si Schottky junction solar cells*. in *Photovoltaic Specialists Conference (PVSC), 2013 IEEE 39th*. 2013. IEEE.
46. Alferov, Z.I., *State-of-the art and prospects of A III B V science and technology*. Czechoslovak Journal of Physics B, 1980. **30**(3): p. 245-261.
47. Rappaport, P., *The photovoltaic effect and its utilization*. Solar Energy, 1959. **3**(4): p. 8-18.

48. Wagner, S., et al., *p-InP/n-CdS solar cells and photovoltaic detectors*. Applied Physics Letters, 1975. **26**(5): p. 229-230.
49. Green, M.A., et al., *Solar cell efficiency tables (version 26)*. Progress in Photovoltaics: Research and Applications, 2005. **13**(5): p. 387-392.
50. Shi, Z. and A.H. Jayatissa, *Perovskites-Based Solar Cells: A Review of Recent Progress, Materials and Processing Methods*. Materials, 2018. **11**(5).
51. Jeon, N.J., et al., *Compositional engineering of perovskite materials for high-performance solar cells*. Nature, 2015. **517**(7535): p. 476.
52. Kojima, A., et al., *Organometal halide perovskites as visible-light sensitizers for photovoltaic cells*. Journal of the American Chemical Society, 2009. **131**(17): p. 6050-6051.
53. Saliba, M., et al., *Cesium-containing triple cation perovskite solar cells: improved stability, reproducibility and high efficiency*. Energy & environmental science, 2016. **9**(6): p. 1989-1997.
54. Novoselov, K., et al., *Two-dimensional atomic crystals*. Proceedings of the National Academy of Sciences of the United States of America, 2005. **102**(30): p. 10451-10453.
55. Peres, N., *The transport properties of graphene*. Journal of Physics: Condensed Matter, 2009. **21**(32): p. 323201.
56. Jeong, H.J., et al., *Improved transfer of chemical-vapor-deposited graphene through modification of intermolecular interactions and solubility of poly (methylmethacrylate) layers*. Carbon, 2014. **66**: p. 612-618.
57. Kim, K.S., et al., *Large-scale pattern growth of graphene films for stretchable transparent electrodes*. nature, 2009. **457**(7230): p. 706.
58. Beams, R., L.G. Cançado, and L. Novotny, *Raman characterization of defects and dopants in graphene*. Journal of Physics: Condensed Matter, 2015. **27**(8): p. 083002.
59. Thomsen, C. and S. Reich, *Double resonant Raman scattering in graphite*. Physical review letters, 2000. **85**(24): p. 5214.
60. Saito, R., et al., *Probing phonon dispersion relations of graphite by double resonance Raman scattering*. Physical review letters, 2001. **88**(2): p. 027401.
61. Pimenta, M., et al., *Studying disorder in graphite-based systems by Raman spectroscopy*. Physical chemistry chemical physics, 2007. **9**(11): p. 1276-1290.
62. Lucchese, M.M., et al., *Quantifying ion-induced defects and Raman relaxation length in graphene*. Carbon, 2010. **48**(5): p. 1592-1597.
63. Cançado, L.G., et al., *Quantifying defects in graphene via Raman spectroscopy at different excitation energies*. Nano letters, 2011. **11**(8): p. 3190-3196.
64. Eckmann, A., et al., *Probing the nature of defects in graphene by Raman spectroscopy*. Nano letters, 2012. **12**(8): p. 3925-3930.
65. Lespade, P., et al., *Caractérisation de matériaux carbonés par microspectrométrie Raman*. Carbon, 1984. **22**(4-5): p. 375-385.
66. Cancado, L., et al., *Influence of the atomic structure on the Raman spectra of graphite edges*. Physical review letters, 2004. **93**(24): p. 247401.
67. Casiraghi, C., et al., *Raman spectroscopy of graphene edges*. Nano letters, 2009. **9**(4): p. 1433-1441.
68. Beams, R., L.G. Cançado, and L. Novotny, *Low temperature Raman study of the electron coherence length near graphene edges*. Nano letters, 2011. **11**(3): p. 1177-1181.
69. Tuinstra, F. and J.L. Koenig, *Raman spectrum of graphite*. The Journal of Chemical Physics, 1970. **53**(3): p. 1126-1130.
70. Saito, R., et al., *Raman spectroscopy of graphene and carbon nanotubes*. Advances in Physics, 2011. **60**(3): p. 413-550.
71. Tivanov, M., et al., *Significant G peak temperature shift in Raman spectra of graphene on copper*. Journal of Materials Science: Materials in Electronics, 2016. **27**(9): p. 8879-8883.
72. Souza, M., et al., *Single-and double-resonance Raman G-band processes in carbon nanotubes*. Physical Review B, 2004. **69**(24): p. 241403.

73. Felten, A., et al., *Radio-frequency plasma functionalization of carbon nanotubes surface O 2, NH 3, and CF 4 treatments*. Journal of applied physics, 2005. **98**(7): p. 074308.
74. Jorio, A., et al., *G-band resonant Raman study of 62 isolated single-wall carbon nanotubes*. Physical Review B, 2002. **65**(15): p. 155412.
75. Ferrari, A.C., et al., *Raman spectrum of graphene and graphene layers*. Physical review letters, 2006. **97**(18): p. 187401.
76. Cançado, L., et al., *Geometrical approach for the study of G' band in the Raman spectrum of monolayer graphene, bilayer graphene, and bulk graphite*. Physical Review B, 2008. **77**(24): p. 245408.
77. Lindvall, N., *Towards graphene-based devices: Fabrication and characterization*. 2012.
78. Wang, X., et al., *N-doping of graphene through electrothermal reactions with ammonia*. Science, 2009. **324**(5928): p. 768-771.
79. Tombros, N., et al., *Electronic spin transport and spin precession in single graphene layers at room temperature*. Nature, 2007. **448**(7153): p. 571-574.
80. Katsnelson, M., K. Novoselov, and A. Geim, *Chiral tunnelling and the Klein paradox in graphene*. Nature physics, 2006. **2**(9): p. 620-625.
81. 電界効果トランジスタの制作と評価, *Fabrication and Characterization of Carbon Nanotube and Graphene Field-Effect Transistors*.
82. Nagashio, K., et al. *Metal/graphene contact as a performance killer of ultra-high mobility graphene analysis of intrinsic mobility and contact resistance*. in *Electron Devices Meeting (IEDM), 2009 IEEE International*. 2009. IEEE.
83. Blake, P., et al., *Influence of metal contacts and charge inhomogeneity on transport properties of graphene near the neutrality point*. Solid State Communications, 2009. **149**(27-28): p. 1068-1071.
84. Liu, W., et al., *Impact of process induced defects on the contact characteristics of Ti/graphene devices*. Electrochemical and Solid-State Letters, 2011. **14**(12): p. K67-K69.
85. Liu, W., et al., *A study on graphene—metal contact*. Crystals, 2013. **3**(1): p. 257-274.
86. Lee, Y., et al., *Wafer-scale synthesis and transfer of graphene films*. Nano letters, 2010. **10**(2): p. 490-493.
87. Li, X., et al., *Large-area synthesis of high-quality and uniform graphene films on copper foils*. Science, 2009. **324**(5932): p. 1312-1314.
88. Li, X., et al., *Evolution of graphene growth on Ni and Cu by carbon isotope labeling*. Nano letters, 2009. **9**(12): p. 4268-4272.
89. Land, T., et al., *STM investigation of single layer graphite structures produced on Pt (111) by hydrocarbon decomposition*. Surface Science, 1992. **264**(3): p. 261-270.
90. Nagashima, A., et al., *Electronic states of monolayer graphite formed on TiC (111) surface*. Surface Science, 1993. **291**(1): p. 93-98.
91. Li, Z., et al., *Chemical Vapor Deposition Growth of Graphene using Other Hydrocarbon Sources*. arXiv preprint arXiv:1101.5664, 2011.
92. Li, X., et al., *Graphene films with large domain size by a two-step chemical vapor deposition process*. Nano letters, 2010. **10**(11): p. 4328-4334.
93. Reina, A., et al., *Growth of large-area single-and bi-layer graphene by controlled carbon precipitation on polycrystalline Ni surfaces*. Nano Research, 2009. **2**(6): p. 509-516.
94. Grüneis, A., K. Kummer, and D.V. Vyalikh, *Dynamics of graphene growth on a metal surface: a time-dependent photoemission study*. New Journal of Physics, 2009. **11**(7): p. 073050.
95. Wang, H., et al., *Controllable synthesis of submillimeter single-crystal monolayer graphene domains on copper foils by suppressing nucleation*. Journal of the American Chemical Society, 2012. **134**(8): p. 3627-3630.

96. Zhang, Y., et al., *Comparison of graphene growth on single-crystalline and polycrystalline Ni by chemical vapor deposition*. The Journal of Physical Chemistry Letters, 2010. **1**(20): p. 3101-3107.
97. Yu, Q., et al., *Graphene segregated on Ni surfaces and transferred to insulators*. Applied Physics Letters, 2008. **93**(11): p. 113103.
98. Xie, C., et al., *Monolayer graphene film/silicon nanowire array Schottky junction solar cells*. Applied Physics Letters, 2011. **99**(13): p. 133113.
99. Jiao, T., et al., *Flexible solar cells based on graphene-ultrathin silicon Schottky junction*. Rsc Advances, 2015. **5**(89): p. 73202-73206.
100. Miao, X., et al., *High efficiency graphene solar cells by chemical doping*. Nano letters, 2012. **12**(6): p. 2745-2750.
101. Yu, X., et al., *The enhanced efficiency of graphene–silicon solar cells by electric field doping*. Nanoscale, 2015. **7**(16): p. 7072-7077.
102. Wu, Z.T., et al., *The influence of chemical solvents on the properties of CVD graphene*. Journal of Raman Spectroscopy, 2015. **46**(1): p. 21-24.
103. Choi, Y., et al., *The effect of the graphene integration process on the performance of graphene-based Schottky junction solar cells*. Journal of Materials Chemistry A, 2017. **5**(35): p. 18716-18724.
104. Ishigami, M., et al., *Atomic structure of graphene on SiO₂*. Nano letters, 2007. **7**(6): p. 1643-1648.
105. Chen, J.-H., et al., *Charged-impurity scattering in graphene*. Nature Physics, 2008. **4**(5): p. 377-381.
106. Schedin, F., et al., *Detection of individual gas molecules adsorbed on graphene*. Nature materials, 2007. **6**(9): p. 652.
107. Lin, Y.-C., et al., *Graphene annealing: how clean can it be?* Nano letters, 2011. **12**(1): p. 414-419.
108. Liao, Z.-M., et al., *Hysteresis reversion in graphene field-effect transistors*. The Journal of chemical physics, 2010. **133**(4): p. 044703.
109. Shi, Y., et al., *Effective doping of single-layer graphene from underlying SiO₂ substrates*. Physical Review B, 2009. **79**(11): p. 115402.
110. Jung, I., et al., *Effect of water vapor on electrical properties of individual reduced graphene oxide sheets*. The Journal of Physical Chemistry C, 2008. **112**(51): p. 20264-20268.
111. Hu, C., et al., *Observation of mutual diffusion of macromolecules in PS/PMMA binary films by confocal Raman microscopy*. Soft Matter, 2012. **8**(17): p. 4780-4787.
112. Tunnell, A., V. Ballarotto, and J. Cumings, *A measurement technique for circumventing hysteresis and conductance drift in carbon nanotube field-effect transistors*. Nanotechnology, 2014. **25**(4): p. 045705.
113. Kim, W., et al., *Hysteresis caused by water molecules in carbon nanotube field-effect transistors*. Nano Letters, 2003. **3**(2): p. 193-198.
114. Lafkioti, M., et al., *Graphene on a hydrophobic substrate: doping reduction and hysteresis suppression under ambient conditions*. Nano letters, 2010. **10**(4): p. 1149-1153.
115. Kunpeng, J., et al., *Stability analysis of a back-gate graphene transistor in air environment*. Journal of Semiconductors, 2013. **34**(8): p. 084004.
116. Yang, Y. and R. Murali, *Binding mechanisms of molecular oxygen and moisture to graphene*. Applied Physics Letters, 2011. **98**(9): p. 093116.
117. Suhail, A., et al., *Reduction of polymer residue on wet–transferred cvd graphene surface by deep UV exposure*. Applied Physics Letters, 2017. **110**(18): p. 183103.
118. Cheng, Z., et al., *Toward intrinsic graphene surfaces: a systematic study on thermal annealing and wet-chemical treatment of SiO₂-supported graphene devices*. Nano letters, 2011. **11**(2): p. 767-771.
119. Goossens, A., et al., *Mechanical cleaning of graphene*. Applied Physics Letters, 2012. **100**(7): p. 073110.

120. Kuzmenko, A., et al., *Universal optical conductance of graphite*. Physical review letters, 2008. **100**(11): p. 117401.
121. Her, M., R. Beams, and L. Novotny, *Graphene transfer with reduced residue*. Physics Letters A, 2013. **377**(21): p. 1455-1458.
122. Suk, J.W., et al., *Enhancement of the electrical properties of graphene grown by chemical vapor deposition via controlling the effects of polymer residue*. Nano letters, 2013. **13**(4): p. 1462-1467.
123. Choi, W., et al., *Effect of Annealing in Ar/H₂ Environment on Chemical Vapor Deposition-Grown Graphene Transferred With Poly (Methyl Methacrylate)*. IEEE Transactions on Nanotechnology, 2015. **14**(1): p. 70-74.
124. Ni, Z.H., et al., *Tunable stress and controlled thickness modification in graphene by annealing*. ACS nano, 2008. **2**(5): p. 1033-1039.
125. Wang, Y., et al., *Top-grid monolayer graphene/Si Schottky solar cell*. Journal of Solid State Chemistry, 2015. **224**: p. 102-106.
126. Xu, Y., et al., *Contacts between two-and three-dimensional materials: Ohmic, schottky, and p-n heterojunctions*. ACS nano, 2016. **10**(5): p. 4895-4919.
127. Song, Y., et al., *Role of interfacial oxide in high-efficiency graphene-silicon Schottky barrier solar cells*. Nano letters, 2015. **15**(3): p. 2104-2110.
128. Yu, X., et al., *The enhanced efficiency of graphene-silicon solar cells by electric field doping*. Nanoscale, 2015. **7**(16): p. 7072-7.
129. Yang, L., et al., *An 8.68% Efficiency Chemically-Doped-Free Graphene-Silicon Solar Cell Using Silver Nanowires Network Buried Contacts*. ACS applied materials & interfaces, 2015. **7**(7): p. 4135-4141.
130. Aberle, A.G., *Surface passivation of crystalline silicon solar cells: a review*. Progress in Photovoltaics: Research and Applications, 2000. **8**(5): p. 473-487.
131. Lin, Y., et al., *Graphene/semiconductor heterojunction solar cells with modulated antireflection and graphene work function*. Energy & Environmental Science, 2013. **6**(1): p. 108-115.
132. Yang, L., et al., *Interface engineering for efficient and stable chemical-doping-free graphene-on-silicon solar cells by introducing a graphene oxide interlayer*. Journal of Materials Chemistry A, 2014. **2**(40): p. 16877-16883.
133. Shi, E., et al., *Colloidal antireflection coating improves graphene-silicon solar cells*. Nano letters, 2013. **13**(4): p. 1776-1781.
134. An, X., F. Liu, and S. Kar, *Optimizing performance parameters of graphene-silicon and thin transparent graphite-silicon heterojunction solar cells*. Carbon, 2013. **57**: p. 329-337.
135. Shi, Y., et al., *Work function engineering of graphene electrode via chemical doping*. ACS nano, 2010. **4**(5): p. 2689-2694.
136. Wadhwa, P., et al., *Electronic junction control in a nanotube-semiconductor Schottky junction solar cell*. Nano letters, 2010. **10**(12): p. 5001-5005.
137. Wadhwa, P., et al., *Electrolyte-induced inversion layer Schottky junction solar cells*. Nano letters, 2011. **11**(6): p. 2419-2423.
138. An, X., et al., *Tunable graphene-silicon heterojunctions for ultrasensitive photodetection*. Nano letters, 2013. **13**(3): p. 909-916.
139. Regan, W., et al., *Screening-engineered field-effect solar cells*. Nano letters, 2012. **12**(8): p. 4300-4304.
140. Li, X., et al., *Anomalous behaviors of graphene transparent conductors in graphene-silicon heterojunction solar cells*. Advanced Energy Materials, 2013. **3**(8): p. 1029-1034.
141. Cui, T., et al., *Enhanced efficiency of graphene/silicon heterojunction solar cells by molecular doping*. Journal of Materials Chemistry A, 2013. **1**(18): p. 5736-5740.
142. Kim, K.K., et al., *Enhancing the conductivity of transparent graphene films via doping*. Nanotechnology, 2010. **21**(28): p. 285205.
143. Choi, D., et al., *Nanopatterned graphene field effect transistor fabricated using block co-polymer lithography*. Materials Research Letters, 2014. **2**(3): p. 131-139.

144. Berger, C., et al., *Electronic confinement and coherence in patterned epitaxial graphene*. Science, 2006. **312**(5777): p. 1191-1196.
145. Han, M.Y., et al., *Energy band-gap engineering of graphene nanoribbons*. Physical review letters, 2007. **98**(20): p. 206805.
146. Kim, K.-J., et al., *Surface property change of graphene using nitrogen ion*. Journal of Physics: Condensed Matter, 2010. **22**(4): p. 045005.
147. Kim, K., et al., *Electric property evolution of structurally defected multilayer graphene*. Nano letters, 2008. **8**(10): p. 3092-3096.
148. Shin, Y.J., et al., *Surface-energy engineering of graphene*. Langmuir, 2010. **26**(6): p. 3798-3802.
149. Gokus, T., et al., *Making graphene luminescent by oxygen plasma treatment*. ACS nano, 2009. **3**(12): p. 3963-3968.
150. Özyilmaz, B., et al., *Electronic transport in locally gated graphene nanoconstrictions*. Applied Physics Letters, 2007. **91**(19): p. 192107.
151. Beery, D., et al. *Post etch residue removal: novel dry clean technology using densified fluid cleaning (DFC)*. in *Interconnect Technology, 1999. IEEE International Conference*. 1999. IEEE.
152. De Gendt, S., et al. *A novel resist and post-etch residue removal process using ozonated chemistries*. in *VLSI Technology, 1998. Digest of Technical Papers. 1998 Symposium on*. 1998. IEEE.
153. Li, B., et al., *Deep UV hardening of photoresist for shaping of graphene and lift-off fabrication of back-gated field effect biosensors by ion-milling and sputter deposition*. Carbon, 2017. **118**: p. 43-49.
154. Frank, I.W., *Shaping Graphene: An Alternative Approach*. 2008.
155. Guo, B., et al., *Controllable N-doping of graphene*. Nano letters, 2010. **10**(12): p. 4975-4980.
156. Nagashio, K. and A. Toriumi, *Density-of-states limited contact resistance in graphene field-effect transistors*. Japanese Journal of Applied Physics, 2011. **50**(7R): p. 070108.
157. Dlubak, B., et al., *Are Al₂O₃ and MgO tunnel barriers suitable for spin injection in graphene?* Applied Physics Letters, 2010. **97**(9): p. 092502.
158. Maneshian, M.H., et al., *The influence of high dielectric constant aluminum oxide sputter deposition on the structure and properties of multilayer epitaxial graphene*. Nanotechnology, 2011. **22**(20): p. 205703.
159. Friedemann, M., et al., *Versatile sputtering technology for Al₂O₃ gate insulators on graphene*. Science and technology of advanced materials, 2012. **13**(2): p. 025007.
160. Quintana, M., E. Vazquez, and M. Prato, *Organic functionalization of graphene in dispersions*. Accounts of chemical research, 2012. **46**(1): p. 138-148.
161. Li, B., *Graphene transistors for label-free biosensing*. 2016.
162. Martin, P.M., *Handbook of deposition technologies for films and coatings: science, applications and technology*. 2009: William Andrew.
163. Gao, L., et al., *Total color difference for rapid and accurate identification of graphene*. ACS nano, 2008. **2**(8): p. 1625-1633.
164. Bhushan, B. and O. Marti, *Scanning probe microscopy—principle of operation, instrumentation, and probes*. 2010: Springer.
165. Schrader, B., *Infrared and Raman spectroscopy: methods and applications*. 2008: John Wiley & Sons.
166. Holder, J.K.L., *Quantum structures in photovoltaic devices*. 2013, University of Oxford.
167. Pirkle, A., et al., *The effect of chemical residues on the physical and electrical properties of chemical vapor deposited graphene transferred to SiO₂*. Applied Physics Letters, 2011. **99**(12): p. 122108.
168. Shin, H.-J., et al., *Control of electronic structure of graphene by various dopants and their effects on a nanogenerator*. Journal of the American Chemical Society, 2010. **132**(44): p. 15603-15609.

169. Doniach, S. and M. Sunjic, *Many-electron singularity in X-ray photoemission and X-ray line spectra from metals*. Journal of Physics C: Solid State Physics, 1970. **3**(2): p. 285.
170. Suk, J.W., et al., *Mechanical measurements of ultra-thin amorphous carbon membranes using scanning atomic force microscopy*. Carbon, 2012. **50**(6): p. 2220-2225.
171. Some, S., et al., *Binol salt as a completely removable graphene surfactant*. Chemical Communications, 2012. **48**(62): p. 7732-7734.
172. Ngan, K.K.-T., *Avoiding contamination from induction coil in ionized sputtering*. 1998, Google Patents.
173. Tongay, S., et al., *Stable hole doping of graphene for low electrical resistance and high optical transparency*. Nanotechnology, 2011. **22**(42): p. 425701.
174. Singh, E. and H.S. Nalwa, *Stability of graphene-based heterojunction solar cells*. RSC Advances, 2015. **5**(90): p. 73575-73600.
175. Chaffee, A.L., et al., *CO2 capture by adsorption: materials and process development*. International journal of greenhouse gas control, 2007. **1**(1): p. 11-18.
176. Kook, J.-W., et al., *Synthesis and Characterization of Poly (Methyl Methacrylate)/Polyethylenimine Grafting Core-Shell Nanoparticles for CO2 Adsorption Using Soap-Free Emulsion Copolymerization*. Advances in Materials Physics and Chemistry, 2016. **6**(07): p. 220.
177. Lee, J., et al., *Embedded-gate graphene transistors for high-mobility detachable flexible nanoelectronics*. Applied physics letters, 2012. **100**(15): p. 152104.
178. Shim, M., et al., *Polymer functionalization for air-stable n-type carbon nanotube field-effect transistors*. Journal of the American Chemical Society, 2001. **123**(46): p. 11512-11513.
179. Kong, J. and H. Dai, *Full and modulated chemical gating of individual carbon nanotubes by organic amine compounds*. The Journal of Physical Chemistry B, 2001. **105**(15): p. 2890-2893.
180. An, C.J., et al., *Ultraclean transfer of CVD-grown graphene and its application to flexible organic photovoltaic cells*. Journal of Materials Chemistry A, 2014. **2**(48): p. 20474-20480.
181. Ariza, M., F. Martin, and D. Leinen, *XPS in-depth composition study on commercial monocrystalline silicon solar cells*. Surface and interface analysis, 2003. **35**(3): p. 251-255.
182. Lee, W.H., et al., *Simultaneous transfer and doping of CVD-grown graphene by fluoropolymer for transparent conductive films on plastic*. ACS Nano, 2012. **6**(2): p. 1284-1290.
183. Lu, C.-C., et al., *High mobility flexible graphene field-effect transistors with self-healing gate dielectrics*. ACS nano, 2012. **6**(5): p. 4469-4474.
184. Johnstone, R.W., I.G. Foulds, and M. Parameswaran, *Deep-UV exposure of poly (methyl methacrylate) at 254 nm using low-pressure mercury vapor lamps*. Journal of Vacuum Science & Technology B, 2008. **26**(2): p. 682-685.
185. Haiducu, M., et al., *Deep-UV patterning of commercial grade PMMA for low-cost, large-scale microfluidics*. Journal of Micromechanics and Microengineering, 2008. **18**(11): p. 115029.
186. Liou, J.J., A. Ortiz-Conde, and F. Garcia-Sanchez, *Analysis and design of MOSFETs: modeling, simulation, and parameter extraction*. 2012: Springer Science & Business Media.
187. Wang, H., et al., *Hysteresis of electronic transport in graphene transistors*. ACS nano, 2010. **4**(12): p. 7221-7228.
188. Han, S.-J., et al., *Channel-length-dependent transport behaviors of graphene field-effect transistors*. IEEE Electron Device Letters, 2011. **32**(6): p. 812-814.
189. Jie, Y., et al., *Hysteresis analysis of graphene transistor under repeated test and gate voltage stress*. Journal of Semiconductors, 2014. **35**(9): p. 094003.

190. Kim, S.H., et al., *Performance optimization in gate-tunable Schottky junction solar cells with a light transparent and electric-field permeable graphene mesh on n-Si*. Journal of Materials Chemistry C, 2017. **5**(12): p. 3183-3187.

Appendix

1. Publication and Presentations

1.1 Journal Publication lists

1. **A. Suhail**^{*}, G. Pan, K. Islam, D. Jenkins, A. Milne, Effective chemical treatment for high efficiency graphene/Si Schottky junction solar cells with a graphene back-contact structure, *Advanced Materials Letters* 8(10), 977-982 (2017).
2. **A. Suhail**^{*}, K. Islam, B. Li, D. Jenkins, G. Pan, Reduction of polymer residue on wet-transferred CVD graphene surface by deep UV exposure, *Applied Physics Letters* 110(18) (2017) 183103.
3. B. Li, G. Pan, **A. Suhail**, K. Islam, N. Avent, P. Davey, Deep UV hardening of photoresist for shaping of graphene and lift-off fabrication of back-gated field effect biosensors by ion-milling and sputter deposition, *Carbon* 118 (2017) 43-49.
4. **A. Suhail**^{*}, G. Pan, D. Jenkins, K. Islam, Improved efficiency of graphene/Si Schottky junction solar cell based on back contact structure and DUV treatment, *Carbon* 129 (2017) 520-526.
5. K. Islam, **A. Suhail**, G. Pan, A Label-Free and Ultrasensitive Immunosensor for Detection of Human Chorionic Gonadotrophin Based on Graphene FETs, *Biosensors* 7(3) (2017) 27.
6. K. Islam, S. Damiati, J. Sethi, **A. Suhail**, G. Pan, Development of a Label-Free Immunosensor for Clusterin Detection as an Alzheimer's Biomarker, *Sensors* 18(1) (2018) 308.

1.2 CONFERENCES

1. **Ahmed Suhail**, Genhua Pan, David Jenkins, A new graphene/Si Schottky junction solar cell structure with back-contacting graphene, 2nd International Conference on Graphene technology (ANM), University, of Aveiro, Portugal (2016).
2. **Ahmed Suhail**, Kamrul Islam, Genhua Pan, David Jenkins, Nick Fry, Shaping of graphene using Argon Plasm, 1st International Conference on Nanoscience and Nanotechnology (ICNAN '16), VIT University, India, (2016).
3. **Ahmed Suhail**, Genhua Pan, David Jenkins, Effect of back contact structure on graphene/Si Schottky junction solar cell performance, American Graphene Forum, Royal Caribbean Cruise, Miami, USA, (2016).
4. Carrie Haslam, Kamrul Islam, **Ahmed Suhail**, Toby Whitley, Paul Davey, Shakil A. Awan. "A label-free and ultrasensitive immunosensor for detection of human chorionic gonadotrophin based on graphene FET." Biodetection & Biosensors, Cambridge, UK (2016).
5. **Ahmed Suhail**, Genhua Pan, David Jenkins, Kamrul Islam, Highest conversion efficiency of graphene/Si Schottky junction solar cell with a graphene back-contact cell structure, 14th International conference on Nano sciences and Nanotechnology (NN17), Thessaloniki, Greece, (2017).
6. Kamrul Islam, Genhua Pan, Bing Li, **Ahmed Suhail**. "Graphene Biosensors for Ultrasensitive and Reproducible Detection of Disease Biomarkers, 14th International Conference on Nanosciences & Nanotechnologies (NN17), Thessaloniki, Greece (2017).

7. Kamrul Islam, Bing Li, **Ahmed Suhail**, Shakil Awan, Genhua Pan, Graphene Biosensors for Reproducible and Ultrasensitive Detection of Disease Biomarkers." BiosenseDementia, Plymouth, UK (2017).

8. **Ahmed Suhail**, Genhua Pan, David Jenkins, Kamrul Islam, Effect of PMMA residue on the *J-V* behaviour of graphene/Si Schottky junction solar cell, International Conference on Materials (ICMS), Toronto, Canada (2018).

1.3 Awards

1. Best oral presentation at 1st International Conference on Nanoscience and Nanotechnology (ICNAN '16), VIT University, India, (2016).

2. Best poster presentation at 14th International conference on Nano sciences and Nanotechnology (NN17), Thessaloniki, Greece, (2017).

1.4 Teaching qualification

Successfully passed the Introduction to Teaching and Learning (ITL) course with Distinction at the University of Plymouth (2018).

2. Lithography Designs

A number of different patterns have been designed and used for the shaping and fabrication of devices.

2.1. Designs for gFET devices

Fig. A-1 shows the patterns used for the fabrication of the 7-electrode gFET device with the adjacent channel length of 90 μm . The design for the shaping of a graphene channel with a length of 720 μm and a width of 80 μm is presented in Fig. A-1a shows. Fig. A-4b displays the design for the deposition of a Cr/Au contact on a graphene channel.

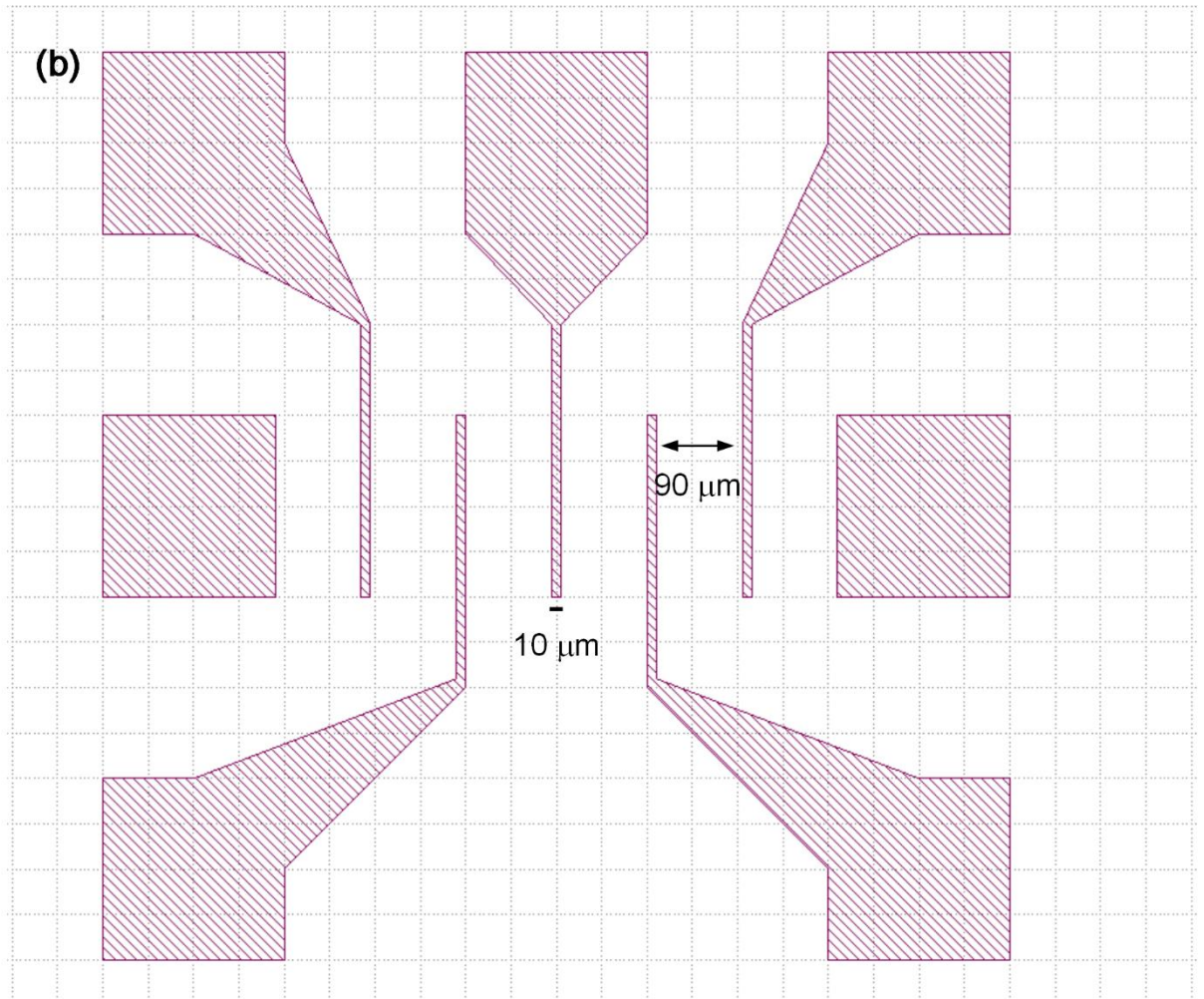
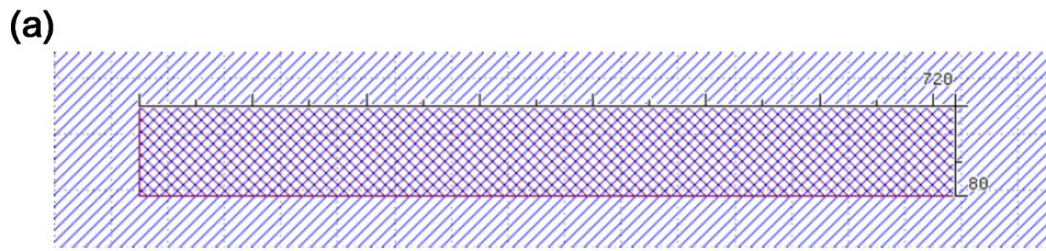


Fig. A-1. Designs for the fabrication of the 7-electrode device. (a) and (b) are the designs for graphene shaping and electrode deposition, respectively.

2.2. Designs for graphene/Si Schottky junction solar cells

The patterns for the fabrication of graphene/Si Schottky junction solar cells with an area of 0.19 cm^2 are shown in Fig. A-2. Fig. A-2a illustrates the design for the shaping of a graphene layer with an area of $3.3 \times 3.3 \text{ mm}^2$. Figs. A-4b and A-4c

show the design for the deposition of Ag/Cr cathode and Au/Cr contact, respectively.

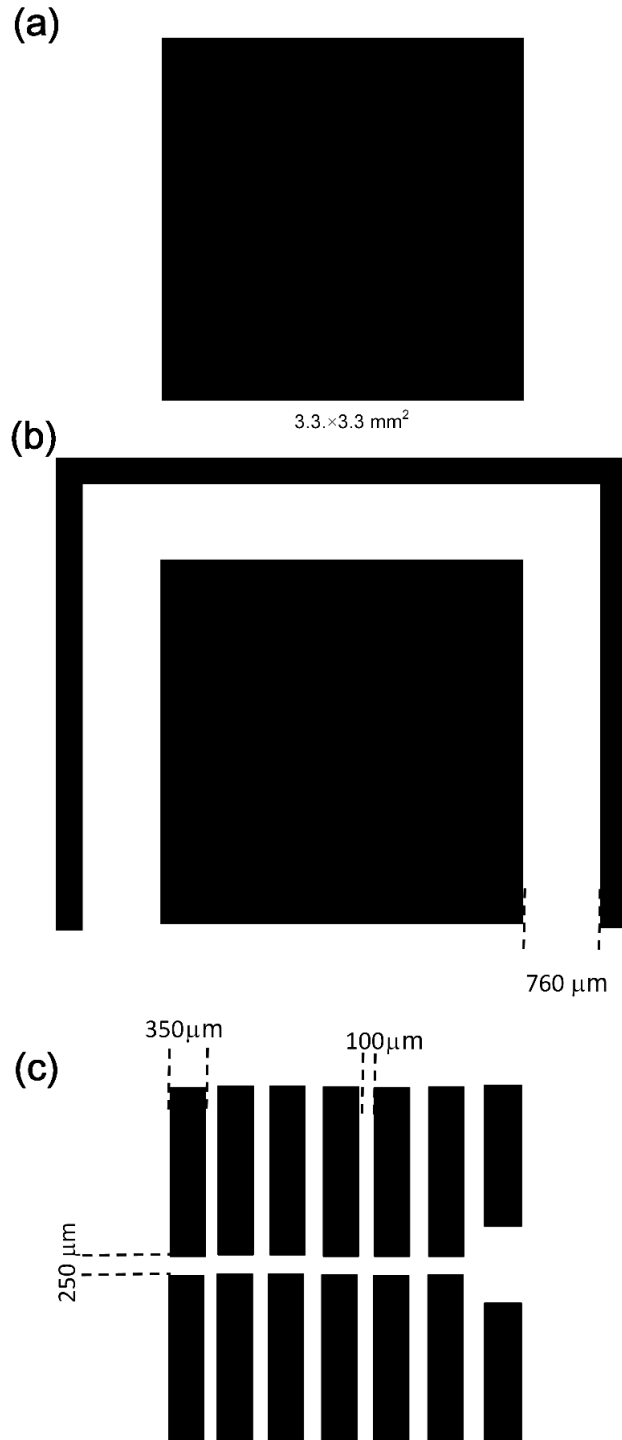


Fig. A-2. Designs for the fabrication of graphene/Si Schottky junction solar cell. (a), (b) and (c) are the designs for graphene shaping and forming contacts of Ag/Cr and Au/Cr, respectively.

3. Materials

4-inch Au target, 99.99% purity (*Kurt J. Lesker, US*)

4-inch Si (200 μm) wafer (*Siltronix, US*)

4-inch Si (500 μm) wafer with 300nm SiO_2 (*Siltronix, US*)

4-inch TiO_2 target (*Kurt J. Lesker, US*)

6-inch Ag target, 99.99% purity (*Kurt J. Lesker, US*)

6-inch Cr target, 99.99% purity (*Kurt J. Lesker, US*)

8-inch SiO_2 target (*Kurt J. Lesker, US*)

Acetone, general purpose grade (*BDH chemicals LTD, UK*)

Ammonium hydroxide, NH_4OH (*Sigma-Aldrich, UK*)

Ammonium persulfate, $(\text{NH}_4)_2\text{S}_2\text{O}_8$ (*Sigma-Aldrich, UK*)

Argon/Hydrogen, Ar/H_2 (*BOC, UK*)

DUV light (*UVP, UK*)

Fan Oven (*WTB binder, Germany*)

Formamide, CH_3NO (*Sigma-Aldrich, UK*)

Graphene (*Graphene Supermarket, USA*)

Hotplate SH8 (*STUART SCIENTIFIC*)

Hydrochloric acid, 37% HCl (*Fisher scientific, UK*)

Hydrogen fluoride, HF (*Sigma-Aldrich, UK*)

Hydrogen peroxide, 27% H_2O_2 (*Sigma-Aldrich, UK*)

IPA, general purpose grade (*BDH chemicals LTD, UK*)

Lift-off Resist 3B (*Rohm and has electrical materials Europe, UK*)

Liquid nitrogen (*BOC, UK*)

Microposit developer 351 (*Rohm and has electrical materials Europe, UK*)

Microposit remover 1165 (*Rohm and has electrical materials Europe, UK*)

Nitric acid, 70% HNO_3 (*Sigma-Aldrich, UK*)

Oxygen free nitrogen, N_2 (*BOC, UK*)

Poly (methyl methacrylate), PMMA (*Sigma-Aldrich, UK*)

Potassium hydroxide, KOH (*Sigma-Aldrich, UK*)

Pure argon, Ar (*BOC, UK*)

S1805 Positive photoresist (*Rohm and has electrical materials Europe, UK*)

Sulfuric acid, H_2SO_4 (*Sigma-Aldrich, UK*)

Ultrasonic Cleaner (*CBEST, US*)

Vacuum spinner 14E (*DAGE PRECIMA INTERNATIONAL*)